PLASMA INTERACTION SIGNATURES OF PLUMES AT EUROPA

A Dissertation
Presented to
The Academic Faculty

By

Hannes Arnold

In Partial Fulfillment
of the Requirements for the Degree
Doctor of Philosophy in the
School of Earth and Atmospheric Sciences

Georgia Institute of Technology

December 2020

PLASMA INTERACTION SIGNATURES OF PLUMES AT EUROPA

Thesis committee:

Dr. Sven Simon
School of Earth and Atmospheric Sciences
Georgia Institute of Technology

Dr. Emanuele Di Lorenzo
School of Earth and Atmospheric Sciences
Georgia Institute of Technology

Dr. Annalisa Bracco
School of Earth and Atmospheric Sciences
Georgia Institute of Technology

Dr. James Wray
School of Earth and Atmospheric Sciences
Georgia Institute of Technology

Dr. Lorenz Roth
Division of Space and Plasma Physics
KTH Royal Institute of Technology

Date approved: October 29, 2020

I am among those who think that science has great beauty.

Marie Curie

To Nova

ACKNOWLEDGMENTS

Four years ago, my plans where very different, until my great friend and fellow student Slawa Kabanovic introduced me to my current advisor Sven Simon. First and foremost, thank you Sven. You made my journey to America possible and your advising was by far the best I experienced up to this day. I enjoyed the countless hours we have spent discussing about my research, taking part in your outstanding classes and the opportunities you made possible during my three years at GaTech. A special thanks to my unofficial second advisor PhD Lucas Liuzzo. You have always been there for my science and non science concerns. Tyler and Peter, thank you for proof reading my thesis! Overall, I would like to thank the whole MOSS group for making the days fly by, especially on our pizza Fridays.

I would not be the person who I am today without all those who I met during my years in academia. A great thank you to my crew from Cologne, Oliver Zingsheim, Johannes Schmidt, Alexander Klug, Jonas Rzezonka, Marc Mertens, Philipp Klatt and Slawa Kabanovic. I had many laughs and discussions about science with all of you. Thanks to Chen Chen and Clara Daniels for keeping my mood up daily and being amazing office mates. Thank you Willi Exner, Moritz Feyerabend, Camilla Harris, Lorenz Roth, Aljona Bloecker and Gabriel Giono for enlightening my days during conferences. Another special thanks goes to Fabrizio Falasca, an amazing roommate and even better friend. Fabri, you always know how to make me laugh with your craziness.

One of the greatest thank yous belongs to my partner Charlotte. Without your support and love this journey would not have been possible. Thank you for being such a great, emphatic partner and giving birth to our wonderful daughter Nova.

Last but not least, I would like to thank my family. Mom and Dad, without your endless patience and support I would not be where I am today. Isabel, our disputes always made me stronger and we share so many fun moments growing up alongside with each other. All of you are part of the best family I could ever have imagined!

TABLE OF CONTENTS

LIST OF TABLES

LIST OF FIGURES

SUMMARY

Europa, the smallest Galilean moon (radius $R_E = 1,560.8$ km) orbits Jupiter at a distance of $9.38R_J$ (radius $R_J = 71,492$ km). As a result of Jupiter's 9.6° tilt between the rotational and magnetic axes, the magnetic field at Europa oscillates. The oscillation induces currents in Europa's conducting material underneath its icy surface, which generates a secondary magnetic field. During several flybys, the Galileo orbiter measured Europa's induced magnetic field signal, and studies have shown that the signal is indicative of a global subsurface ocean. Additionally, observations by the Hubble Space Telescope (HST) in December 2012 measured a localized increase of ultraviolet emission in the south polar region of Europa, which later was interpreted as water vapor plume activity. These findings support the theory of a subsurface ocean, as well as marking a region with accessibility to the material beneath Europa's kilometer thick crust. Subsequent HST observations could not identify the anomalies observed in 2012, indicating that the plumes at Europa are transient in nature.

Recently, additional evidence for the occurrence of transient plumes was found by comparing Galileo magnetometer data from the Galileo E12 flyby on 16 December 1997 to plasma simulation data. Still, the evaluation of Galileo's magnetometer data is incomplete. The goal of our study is to conduct a systematic search of plume signatures in Galileo plasma and magnetic field data from spacecraft flybys of Jupiter's moon Europa. Out of 12 flybys, E12 and E26 were the only flybys that crossed Europa below an altitude of 400 km to it's surface. Studies have shown that electric currents generated by mass loading of the magnetospheric plasma through plume ions would leave an imprint in the Galileo magnetometer data during such a close flyby. We aim to investigate the degree to which

different plume configurations can be obscured by the interaction of Jupiter's magnetospheric plasma with Europa's induced dipole field and its global atmosphere. And, finally, we plan to constrain the diagnostic potential of ion energy spectrograms to identify signatures of water vapor plumes in the thermal plasma environment of Europa.

We apply the parallelized, three-dimensional Adaptive Ion-Kinetic Electron-Fluid (AIKEF) hybrid simulation code to Europa's plasma environment. In contrast to magnetohydrodynamic models that have been used by previous studies, AIKEF can describe asymmetries in the plasma flow near Europa, e.g., due to the ionospheric Hall effect, as well as calculate ion kinetic effects on the small scale height of a plume (an order of magnitude smaller than Europa's radius). To systematically assess the magnitude and structure of the magnetic perturbations associated with plume-plasma interactions at Europa, we plan to vary the plume location across Europa's surface while considering different symmetric and asymmetric density profiles of Europa's global atmosphere. To isolate the impact of a plume on Europa's magnetospheric environment, we will also conduct runs without any global atmosphere. In addition, the model output is used to generate synthetic time series for the count rates of the observable thermal ion population as a function of energy along several hypothetical spacecraft trajectories, as well as for the Galileo E26 flyby. Through comparison of our model results to magnetic field and plasma observations collected near Europa (e.g., by the Galileo spacecraft), we will establish a framework for an in-situ characterization of plumes that complements existing remote studies using the Hubble Space Telescope.

The results of these studies will facilitate the planning of synergistic measurements during upcoming missions to Europa, such as the European Space Agency's upcoming JUpiter ICy moons Explorer mission (JUICE) and the National Aeronautic and Space Administration's Europa Clipper mission.

CHAPTER 1
INTRODUCTION

1.1 Europa

Europa (radius $R_E = 1560.8\,\mathrm{km}$) likely hosts a global subsurface ocean (Kivelson *et al.*, 2000). The study of Schilling *et al.*, 2007 assumes that the ocean is about 100 km deep, whereas the estimates for the thickness of Europa's icy crust ranges from a few km up to 60 km (Hand and Chyba, 2007; Hussmann *et al.*, 2002; Schenk, 2002). Hubble Space Telescope (HST) observations in December 2012 revealed a localized increase in the intensity of ultraviolet emission near the south pole of Europa, associated with a surplus of oxygen and hydrogen. Roth *et al.*, 2014a demonstrated that the observed inhomogeneity in Europa's atmosphere could be explained by two water vapor plumes emanating near 180°W 75°S and 55°S, respectively, each with a scale height of about 200 km (see Figure 1.1). A single, but broader plume could explain the observations equally well. The Europan plumes share many properties with those at Saturn's moon Enceladus. Both sets of plumes have comparable vertical gas speeds at their surface (700 m/s at Europa, estimated by Roth *et al.*, 2014a and 300-2000 m/s at Enceladus, estimated by Hansen *et al.*, 2011; Tian *et al.*, 2007), and nearly identical H_2O column densities ($\approx 1.5 \cdot 10^{20}\ \mathrm{m}^{-2}$ measured at Europa, compared to $\approx 9.0 \cdot 10^{19}\ \mathrm{m}^{-2}$ at Enceladus, Roth *et al.*, 2014a). Thus, similar theories for the formation of plumes at Enceladus have been used to explain the existence of Europa's plumes.

For Enceladus, three theories for the origin of plumes exist: termed "cold faithful", "frigid faithful", and "deep source" (Southworth *et al.*, 2015). In the "cold faithful" model (Porco *et al.*, 2006), plumes originate from boiling explosions of water in shallow ice pockets, ≈ 10 m beneath the surface. A similar theory applied to Europa, however, would imply

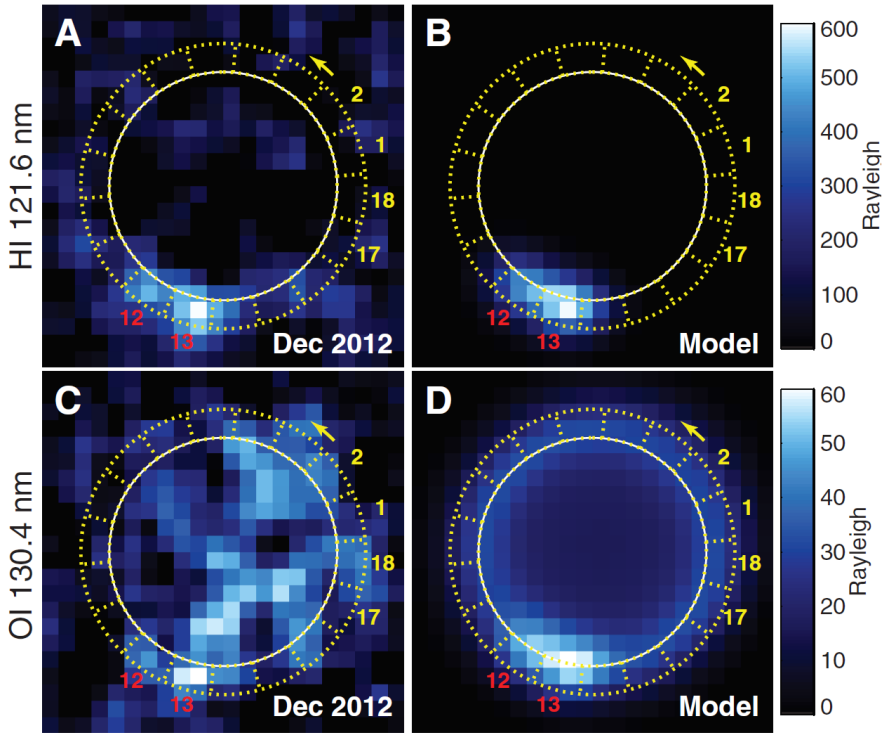

Figure 1.1: A comparison of HST observations from 2012 (panels A and C) and the Roth *et al.*, 2014a plume model (panels B and D). The surplus of oxygen and hydrogen is best visible near the south polar region of Europa, in the red highlighted bins 12 and 13. The patchiness of the 130.4 nm emissions (panel C) might originate from surface reflectance, atmospheric or plasma inhomogeneities. Nevertheless it is still consistent with statistically expected variations across a uniform disk. The schematic has been taken from Roth *et al.*, 2014a.

that the resulting gas velocities of Europa's plumes would be lower than the observed gas velocities (Roth *et al.*, 2014a). The "frigid faithful" model (Kieffer *et al.*, 2006) ascribes the origin of plumes to the decomposition of CO_2, CH_4 and N_2 clathrates located underneath an $H_2O - CO_2$ ice shell at temperatures around 140 K. The vents in this model would be very dilute (Schmidt *et al.*, 2008) and therefore inconsistent with HST observations at Europa. The "deep source" model (Schmidt *et al.*, 2008) describes the outflow of a gas-particle mixture through pressurized vents, evaporating from a reservoir (underneath Europa's surface) at temperatures close to or at the triple point of water. This theory matches observations at Enceladus; however, it is not certain how well this model can be applied to explain Europa's plumes.

After the plume discovery of Roth *et al.*, 2014a in HST data from 2012, Sparks *et al.*, 2016 found plume signatures in three out of ten subsequent HST observations. However, Giono *et al.*, 2020 reanalyzed the limb anomalies discovered by Sparks *et al.*, 2016 and proved that the features can be explained by statistical fluctuations and do not provide evidence for a plume detection. Additionally, Paganini *et al.*, 2019 looked for water vapor signatures at Europa by analyzing infrared observations from the earth-bound Keck observatory. Out of 17 observations, one observation on 26 April 2016 suggests the presence of water vapor in Europa's leading hemisphere. This indicates that (in contrast to the Enceladean plumes), the plumes at Europa seem to be transient in nature (Paganini *et al.*, 2019; Roth *et al.*, 2014b, 2016). Unlike Enceladus, observations of Europa could not connect the mechanism for the plume formation to tidal heating. The precise mechanism is therefore still unknown.

Europa orbits Jupiter at a distance of 9.38 R_J (radius of Jupiter $R_J = 71,492$ km), and is tidally-locked to the planet. The moon is embedded in Jupiter's magnetosphere (the region of space carved out by the presence of the planet's magnetic field, e.g., Smith *et al.*, 1974) and within its plasma sheet (e.g., Kivelson *et al.*, 2009). Since the orbital period of Europa (85.2 h) is significantly larger than Jupiter's rotational period ($\approx$10 h, the synodic period is 11.23 h with respect to Europa), subsonic, magnetospheric plasma continuously impinges onto Europa's "ram side" hemisphere (i.e., its orbital trailing hemisphere).

A high-energy population of magnetospheric particles (on the order of keV-MeV) gyrates along Jupiter's magnetic field lines and impacts the moon's surface, sputtering molecules from it. The incident particles mostly consist of ions (e.g., H^+, O^+,S^+, see Figure 1.2) and electrons (Cooper *et al.*, 2001; Vorburger and Wurz, 2018) and their sputtering results in Europa's thin atmosphere of (mostly) molecular oxygen O_2 (Burger and Johnson, 2004; McGrath *et al.*, 2009), see Figure 1.2. The intensity of the sputtering decreases from Europa's ram side to the moon's wake side (Pospieszalska and Johnson, 1989), as the flux of the magnetospheric particles is reduced in the moon's wake (Cassidy *et al.*, 2013). These

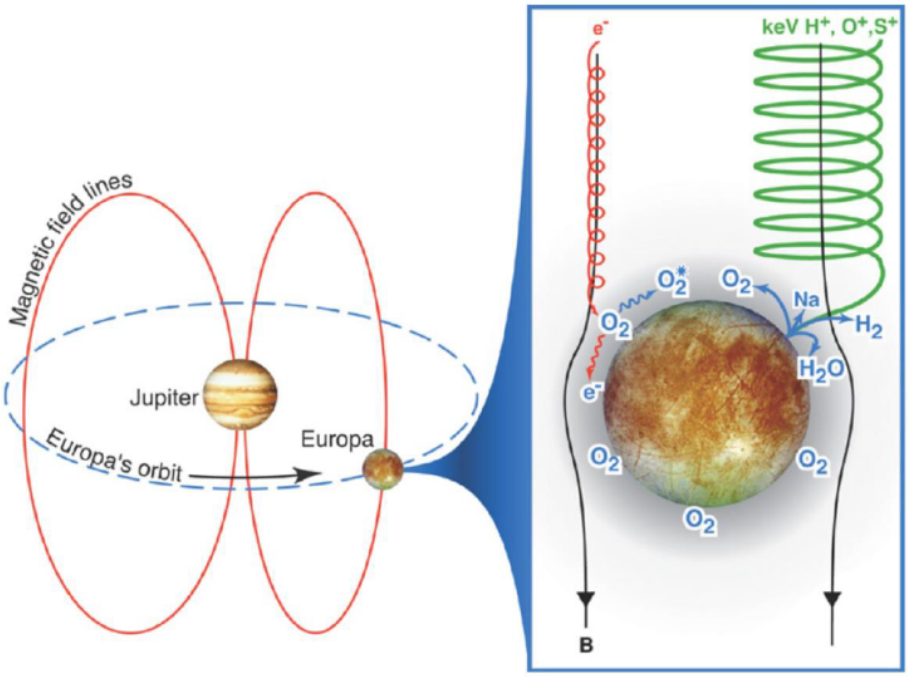

Figure 1.2: A schematic of the formation of Europa's atmosphere and ionosphere. The left side depicts Jupiter's magnetic field lines and Europa's orbit. The right side shows the (high-energy) ion flow along Jupiter's magnetic field lines (represented in green) that is partially responsible for the sputtering of Europa's icy surface. The electron impact ionization is depicted in red. The figure has been adapted from Johnson *et al.*, 2004.

asymmetries can be caused by inhomogeneous solar illumination (Plainaki *et al.*, 2013), the incident plasma flow onto Europa's surface (Plainaki *et al.*, 2013; Pospieszalska and Johnson, 1989) and asymmetries in the magnetic field close to Europa (Breer *et al.*, 2019). During this process, the sputtering releases H_2O molecules into Europa's atmosphere, whereas radiolysis dissociates the molecules to its products, hydrogen and oxygen (Cooper *et al.*, 2001). Electron impact ionization is an order of magnitude stronger than UV ionization and therefore the main ionization process (Saur *et al.*, 1999).

1.2 Plasma Interaction at Europa

The plasma flow past an object (e.g., a moon) can be categorized by the velocity of the upstream plasma and the magnetic environment in the vicinity of the body, thus resulting in a super-magnetosonic or sub-magnetosonic flow. In the case of super-magnetosonic flow, plasma hits the magnetic field of the obstacle at a velocity faster than the magneto sound speed. The information of the body/interaction cannot be transmitted towards the upstream plasma and a bow shock forms. Within the bow shock, the plasma slows to sub-magnetosonic speeds and is deflected around the obstacle. Examples for this interaction scenario are Earth, Saturn and Jupiter. However, within the subsonic flow near Europa, the plasma is slower than the magneto sound speed and information can be transmitted upstream. Therefore, no bow shock forms, but the incident plasma gets deflected around the moon (see Figure 1.3) (Neubauer, 1998). The stagnant flow in front of Europa results in a pile up of magnetic field lines and yields a local increase of the magnetic field strength. In addition, charged ionospheric particles are being picked up by the ambient electromagnetic fields and are accelerated to similar speeds as the ambient flow. This process drains momentum from the incident magnetospheric plasma flow and perturbs the magnetic field in the vicinity of Europa. Collisions in Europa's ionosphere generate an additional current, a motion perpendicular to the incident particle flow and results in magnetic field perturbations (the ionospheric Hall effect).

The kink in Europa's magnetic field propagates north and south (see Figure 1.3, left schematic) with the Alfvén speed $v_A = |\vec{B}|/(\mu_0\rho)^{1/2}$, where $|\vec{B}|$ is the magnitude of the magnetic field, ρ is the mass density of the plasma and μ_0 the vacuum permeability. The draped magnetic field lines transport currents that close within the moon's conducting ionosphere through a system of non-linear standing Alfvén waves (see Figure 1.3, right schematic), and connect Europa to Jupiter's polar ionosphere (Neubauer, 1980; Neubauer, 1998). These tube-like regions are called Alfvén wings. If the plasma flow is perpendic-

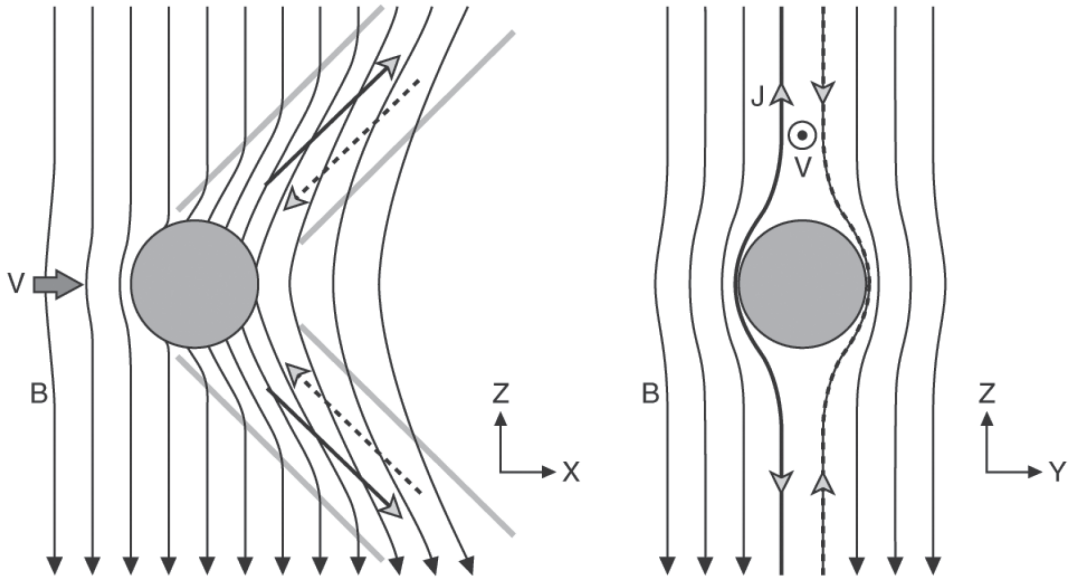

Figure 1.3: Structure of Alfvén wings near Europa. The left schematic shows how Jupiter's magnetic field lines impinge onto Europa and bend during the process. The right side of the figure displays a cut through the center of the moon, in the plane normal to the unperturbed flow. The currents closing in Europa's ionosphere are shown. The schematics are taken from Southwood *et al.*, 1980.

ular to the background field, the angle of the kink θ_A (see Figure 1.3, measured between the undisturbed and bent field lines) can be expressed in terms of the Alfvén Mach number of the flow, $M_A = u/v_A$ (where u is the bulk velocity of the impinging plasma), as $\theta_A = \arctan^{-1} M_A$.

Driven by the 9.6° tilt between Jupiter's magnetic and rotational axes (M and Ω, respectively, see Figure 1.4 (b)), the ambient magnetospheric field near Europa exhibits an oscillation at Jupiter's synodic rotation period. This time variability induces a secondary magnetic field in Europa's conducting subsurface ocean, which has a dipolar shape outside of the moon (Khurana *et al.*, 1998; Zimmer *et al.*, 2000). Therefore, in addition to Europa's atmosphere/ionosphere, the magnetospheric plasma interacts with a (time-varying) dipole field induced in Europa's subsurface ocean (Kivelson *et al.*, 1999). Depending on Europa's location with respect to the center of Jupiter's current sheet, the magnitude of the induced dipole and upstream plasma density varies. For example, if Europa is located at the center

of Jupiter's current sheet, Jupiter's magnetic and rotational axes coincide, the induced magnetic field is at its minimum and the upstream plasma density at its maximum (Figure 1.4 (a)). The induced dipole contributes to the plasma deflection and reduces the cross-sections of the two Alfvénic flux tubes, compared to a scenario without induction (Neubauer, 1999; Volwerk *et al.*, 2007).

This picture considers only the influence of Europa's global atmosphere and induced field on the plasma interaction, but not the impact of a possible plume on the electromagnetic perturbations generated by Europa's interaction. A localized inhomogeneity in Europa's atmosphere would generate a tube-like region of locally enhanced current density and flow deceleration within the main Alfvén wing, referred to as an Alfvén winglet (Blöcker *et al.*, 2016). A plume source, in Europa's southern hemisphere, for example, will therefore break the symmetry of the Alfvén wings between the moon's northern and southern hemispheres (Blöcker *et al.*, 2016). Due to the translational invariance along their characteristics, the Alfvén wings and associated asymmetries can extend to arbitrarily large distances from Europa (Neubauer, 1980). This facilitates a "remote" detection of plumes in magnetic field data from distant Europa flybys.

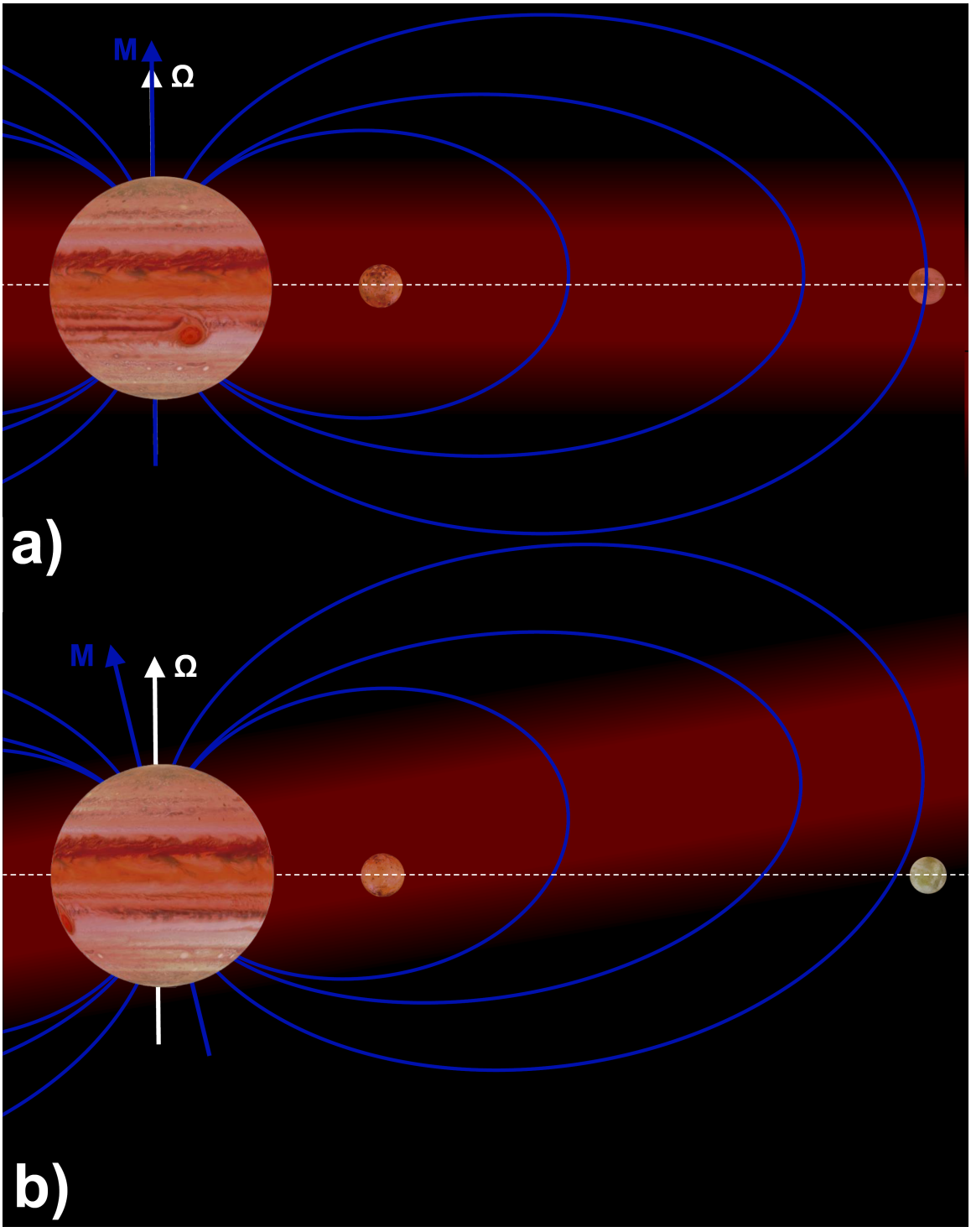

Figure 1.4: This Figure depicts the effect of Jupiter's 9.6° tilt between its magnetic moment (blue M) and rotational axis (white Ω) on Europa's magnetic field environment. Jupiter's plasma torus is depicted in red. The inner most Galilean moons Io and Europa are shown.
(a) When Europa is located at the center of Jupiter's current sheet, Jupiter's magnetic and rotational axes coincide. The induced magnetic field is at its minimum, the upstream plasma density at its maximum.
(b) Through a rotation of Jupiter, Europa's location within Jupiter's current sheet varies due to the tilt between both axes. The current sheet sweeps over the moon, inducing a magnetic field into Europa's subsurface ocean. The upstream plasma density is at its minimum.

1.3 The Galileo Mission

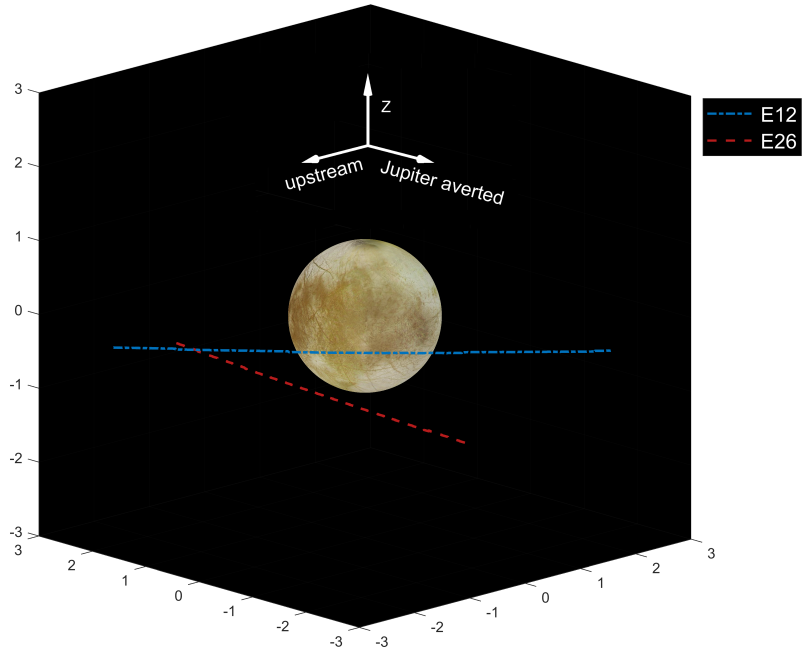

Figure 1.5: Geometry of the Galileo E12 (blue line) and E26 (red line) flybys. The view point is located upstream, from the Jupiter-averted side. Both flybys occurred in the orbital trailing, southern hemisphere of Europa.

Out of 12 Galileo flybys of Europa, only two flybys, E12 (on 16 December 1997) and E26 (on 3 January 2000), have been used to investigate the impact of plumes on the magnetic field perturbations near Europa. ”E” denotes that Europa was the target of the flyby, and the number denotes the orbit of Galileo around Jupiter. Both flybys passed within only 400 km of Europa’s surface, an altitude comparable to the scale height of the plume found by Roth *et al.*, 2014a. They occurred in the orbital trailing hemisphere of Europa: the E12 flyby passed Europa at equatorial latitudes, whereas the E26 flyby occurred at more southern latitudes (see Figure 1.5). As suggested by Blöcker *et al.*, 2016, transverse currents within the plumes (Alfvén winglets) would form inside the main Alfvén wings and should leave a clear imprint in Galileo magnetometer data. Indeed, magnetic field observations from both flybys reveal sharp, highly localized perturbations in all three components of the magnetic field near closest approach (C/A) of the spacecraft (see Figure

1 of Jia *et al.*, 2018 for E12, or Figure 3.2 of this thesis for E26). Additionally, the Energetic Particles Detector (EPD) of the Galileo spacecraft showed energetic ion (115–244 keV) deflection through perturbed fields (e.g., within the Alfvén winglet, Huybrighs *et al.*, 2020) during the E26 and E12 flybys.

1.4 Model of Europa's Plasma Interaction

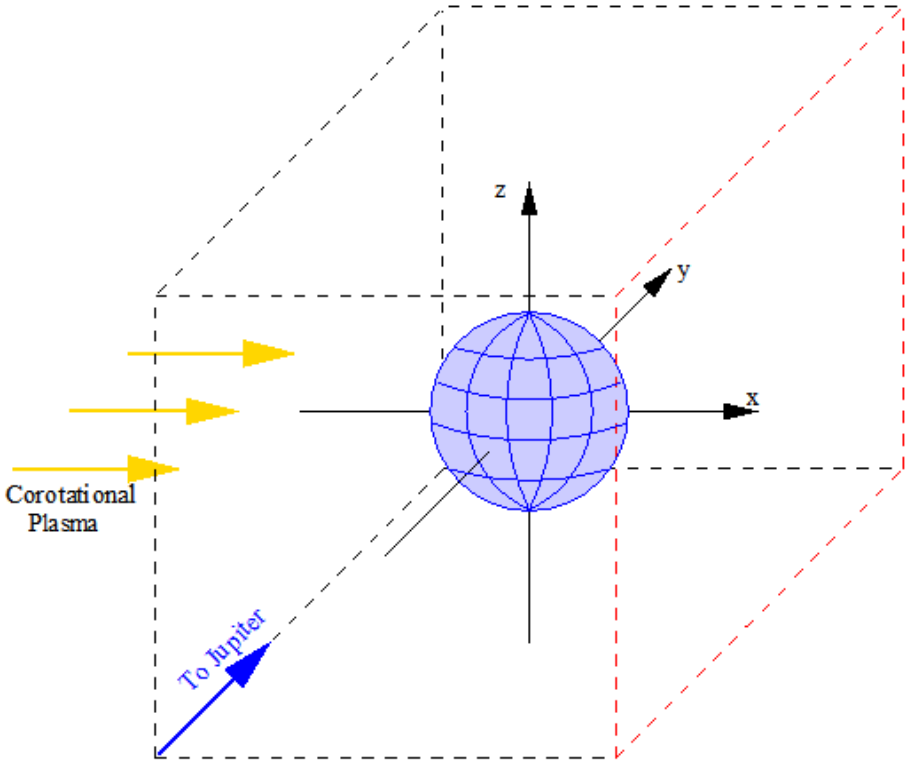

Figure 1.6: In this figure the EPhiO coordinate system is depicted. It is a Cartesian coordinate system, where the x axis is aligned with the co-rotational flow direction, the y axis points towards Jupiter and the z axis completes the right-handed system. The origin of the EPhiO system coincides with the center of Europa.

Throughout this thesis, we use the Europa-centered, Cartesian "EPhiO" coordinate system. In this system the x axis is aligned with the co-rotational flow direction, the y axis points towards Jupiter and the z axis completes the right-handed system (see Figure 1.6). The origin of the EPhiO system coincides with the center of Europa.

1.4.1 Hybrid Code AIKEF

We apply the AIKEF (Adaptive Ion-Kinetic Electron-Fluid) hybrid code (Müller *et al.*, 2011) to simulate Europa's magnetospheric environment. The code treats ions as particles and electrons as a massless, charge-neutralizing fluid. In contrast to the MHD approach of Schilling *et al.*, 2008 and Blöcker *et al.*, 2016, AIKEF can describe asymmetries in the plasma flow due to the ionospheric Hall effect as well as the flow shear between the magnetospheric plasma and the plasma emanating from Europa (e.g., from its ionosphere or a plume source). AIKEF has already been successfully applied to, e.g., model Cassini magnetic field observations from multiple flybys through the Enceladus plume (Kriegel *et al.*, 2009, 2011, 2014) and to study the ion energy distributions observed by the Rosetta spacecraft at comet 67P/Churyumov-Gerasimenko (Koenders *et al.*, 2015).

The ions in our model are represented as macroparticles that have the same charge-to-mass ratio as a real ion. The Newtonian equations of motion are solved for each macroparticle

$$\frac{d\vec{x_i}}{dt} = \vec{v_i} \quad \wedge \quad \frac{d\vec{v_i}}{dt} = \frac{q_i}{m_i}(\vec{E} + \vec{v_i} \times \vec{B}) \quad , \tag{1.1}$$

where q_i and m_i are the ion's charge and mass, respectively. The vectors $\vec{E}$ and $\vec{B}$ are the electric and magnetic field at the particle position $\vec{x_i}$ and determine the ion's velocity $\vec{v_i}$.

For the electrons the starting point is the Vlasov's equation

$$\partial_t f_e + \vec{v}\partial_{\vec{x}} f_e + \frac{e}{m_e}\left[(\vec{E} + \vec{v} \times \vec{B})\partial_{\vec{v}} f_e\right] = 0 \quad , \tag{1.2}$$

where f_e, e, m_e and $\vec{v}$ represent the distribution function, elementary charge, mass and the individual electron velocity of the fluid, respectively. From the Vlasov's equation, we derive a modified Navier-Stokes equation by assuming that the electrons are massless compared to the ions:

$$m_e \frac{d\vec{u_e}}{dt} = 0 = -en_e[\vec{E} + \vec{u_e} \times \vec{B}] - \nabla P_e + n_e \eta \vec{j} \quad , \tag{1.3}$$

where $\vec{j}$ is the current and η the resistivity of the fluid. In order to close this system of equations, an adiabatic equation is assumed for the electron pressure

$$P_e = P_{e,0} \left(\frac{n_e}{n_{e,0}} \right)^{\kappa} \quad , \tag{1.4}$$

where $P_{e,0}$ is the initial electron pressure, $n_{e,0}$ the initial density and the adiabatic exponent κ is set to $\kappa = 2$ (because the magnetic field reduces the degree of freedom).

By using the definition of the electric current $\vec{j} = \vec{j_e} + \vec{j_i} = -en_e\vec{u_e} + \sum_i en_i\vec{u_i}$ and the ion bulk velocity $\vec{u_i}$, the electric field can be written as

$$\vec{E} = -\vec{u_i} \times \vec{B} + \frac{[\nabla \times \vec{B}] \times \vec{B}}{en_i\mu_0} - \frac{\nabla P_e}{en_i} + \frac{\eta}{\mu_0}\nabla \times \vec{B} \quad . \tag{1.5}$$

Finally, the time evolution of the magnetic field is described by Faraday's law $\nabla \times \vec{E} = -\partial_t \vec{B}$.

1.4.2 Model of Europa's Atmosphere

Within AIKEF, Europa's atmosphere consists of molecular oxygen, which is the dominant species at Europa (Hall *et al.*, 1995; McGrath *et al.*, 2009). Sputtering of Europa's surface is not uniform: Pospieszalska and Johnson, 1989 as well as Cassidy *et al.*, 2013 showed that the sputtering rate decreases from the trailing (ram side) hemisphere towards the leading (wake side) hemisphere. Therefore, the distribution of neutral gas is not expected to be uniform across Europa's surface, and we use an analytical description similar to the model of Rubin *et al.*, 2015 to represent this asymmetry. The density profile in the trailing n_T and leading n_L hemispheres reads

$$\begin{aligned} n_L(h) &= n_0 \cdot \exp\left(-\tfrac{h}{h_0}\right), & 90^\circ < \alpha \leq\ 180^\circ \quad , \\ n_T(h,\alpha) &= n_L(h) \cdot (1 + A \cdot \cos(\alpha)), & \alpha \leq\ 90^\circ \quad , \end{aligned} \tag{1.6}$$

with the radial distance $h = |\vec{r}| - R_E$ (where $\vec{r}$ is the position vector from Europa's center) to Europa's surface, the neutral scale height $h_0 = 100$ km and the surface density $n_0 = 5{\cdot}10^{13}$ m^{-3}. Symbol α denotes the angle between the position $\vec{r}$ and the negative x axis (which points into the trailing/ram side hemisphere). The parameter A represents the strength of the trailing/leading asymmetry of the atmosphere. We consider two cases: $A = 0$, similar to the symmetric, barometric profile of Blöcker *et al.*, 2016 and $A > 0$. In this way, we can simulate large-scale/global atmospheric asymmetries and determine whether they obstruct any (locally) observable plume signatures in the magnetic field. The O_2 column density in our runs ranges from $5 \cdot 10^{18}$ m^{-2} (globally for $A = 0$) to $5.5 \cdot 10^{19}$ m^{-2} (at the apex of the ram side hemisphere for $A = 10$). These values are consistent with the interval of $10^{18} - 10^{19}$ m^{-2} inferred for the column density of Europa's atmosphere from HST observations (Hall *et al.*, 1995; Plainaki *et al.*, 2018; Saur *et al.*, 1998).

1.4.3 Model of Europa's Plumes

The neutral density profile in our model is similar to the profile of Jia *et al.*, 2018:

$$n_P(h, \Delta\theta) = n_{P,0} \cdot \exp\left[-\left(\frac{h}{h_p}\right)^2 - \left(\frac{\Delta\theta(\vec{P})}{h_\theta}\right)^2 \right] \quad , \tag{1.7}$$

where $\Delta\theta(\vec{P})$ represents the angular distance from the center of the plume axis $\vec{P}$ (which is *not* necessarily perpendicular to Europa's surface), h_p the scale height of the plume, h_θ the opening angle of the plume and $n_{P,0}$ the surface number density of the plume (see Figure 1.7). Thus, the neutral density profile of the plume is rotationally symmetric around the plume axis $\vec{P}$. In our simulations we use $h_p = 200$ km, $h_\theta = 15°$ and $n_{P,0} = 3.9 \cdot 10^{15}$ m^{-3}, resulting in a H_2O column density (along the plume axis) of $7.8 \cdot 10^{20}$ m^{-2}. This value is consistent with the range of values inferred from HST observations: $1.5 \cdot 10^{20}$ m^{-2} to $2.3 \cdot 10^{21}$ m^{-2} (Roth *et al.*, 2014a). The location of the plume's "footpoint" on Europa's surface and the orientation of its symmetry axis $\vec{P}$ (with respect to the surface) are free

parameters in our model (similar to Jia *et al.*, 2018).

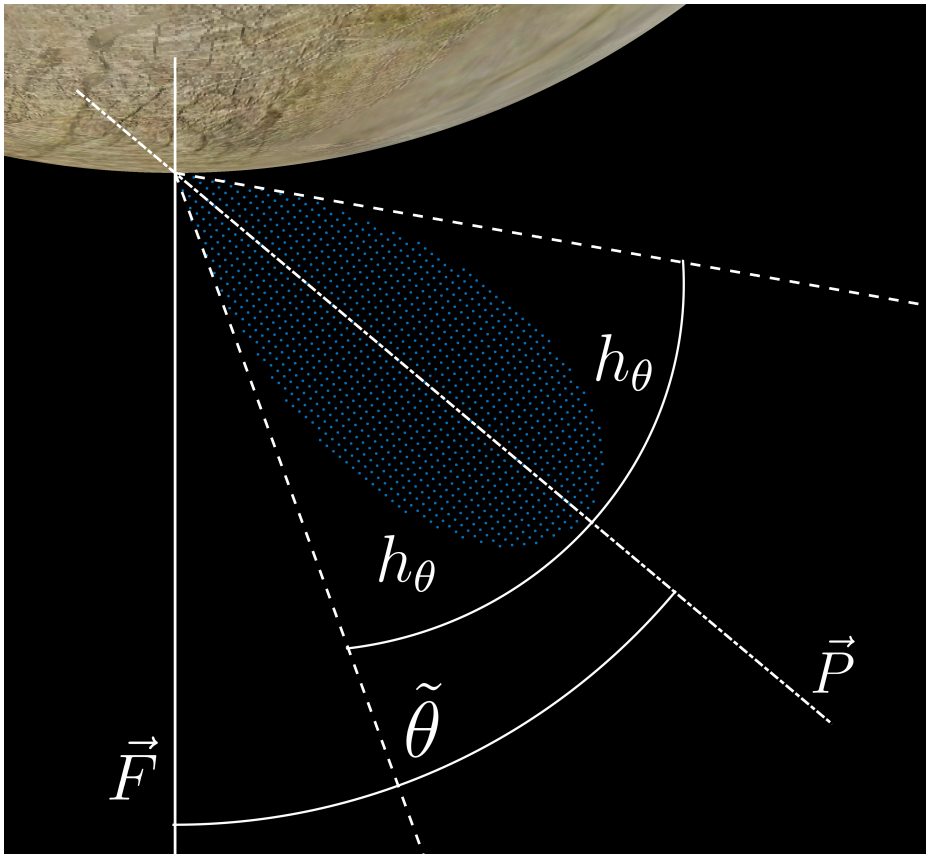

Figure 1.7: Schematic of the plume orientation in 2D. $\vec{F}$ marks the axis orthogonal to the location of the plume footpoint, $\tilde{\Theta}$ corresponds to the inclination of the plume axis $\vec{P}$ against $\vec{F}$ (in the Θ direction) and h_Θ represents the opening angle of a plume. $\tilde{\phi}$ points into the Figure and is therefore not displayed.

The footpoint of a plume at Europa's surface is located at

$$\vec{F}(\theta_F, \phi_F) = R_E(\sin(\theta_F)\cos(\phi_F), \sin(\theta_F)\sin(\phi_F), \cos(\theta_F)) \quad , \tag{1.8}$$

where ϕ_F is measured in the right-handed EPhiO coordinate system and $\phi_F = 0°$ coincides with the apex of Europa's Jupiter facing hemisphere. Angle $\theta_F = 0°$ marks Europa's north pole and $\theta_F = 180°$ Europa's south pole, respectively. $\vec{P}$ represents the inclination of the plume axis against the radial direction at the footpoint $\vec{F}$ and is defined by the angles $\tilde{\theta} = \theta - \theta_F$ and $\tilde{\phi} = \phi - \phi_F$; i.e., $\tilde{\theta} = 0°$, $\tilde{\phi} = 0°$ means that the plume axis $\vec{P}$ is

perpendicular to the surface (see Figure 1.7).

1.4.4 Model of Europa's Ionosphere

Saur *et al.*, 1998 showed that electron impact ionization is the dominant ionization process at Europa. We therefore calculate the ion production rate (in analogy to Schilling *et al.*, 2008, Blöcker *et al.*, 2016, and Jia *et al.*, 2018) by multiplying the electron impact ionization rate $f_{imp}(T_e)$ for H_2O and O_2 with the respective neutral density profile, where T_e is the temperature of the incoming electrons. To derive the electron impact ionization rate of each neutral species, we assume a Maxwellian velocity distribution for the ionizing electrons and integrate over their energy-dependent ionization cross sections (taken from the National Institute of Standards and Technology database, Kim *et al.*, 2004), similar to Banks and Kockarts, 1973. This results in constant ionization rates of $2{\cdot}10^{-6}\ \mathrm{s}^{-1}$ for H_2O^+ and $2.3{\cdot}10^{-6}\ \mathrm{s}^{-1}$ for O_2^+. Our model also considers loss of ionospheric O_2^+ and H_2O^+ ions due to dissociative recombination, with the recombination rates given in Schunk and Nagy, 2000:

$$\begin{aligned} \beta_{O_2^+} &= 2 \cdot 10^{-13} \left(\tfrac{300}{T_e}\right)^{0.7} && \mathrm{m^3 s^{-1}} \\ \beta_{H_2O^+} &= 1.03 \cdot 10^{-9} \left(T_e\right)^{-1.111} && \mathrm{m^3 s^{-1}} \quad . \end{aligned} \tag{1.9}$$

1.4.5 Hybrid Simulation Setup

Due to the vast difference in the timescales of the plasma interaction and induction effects (minutes compared to hours, see Seufert *et al.*, 2011), the field induced in Europa's subsurface ocean can be represented as a static dipole moment (Neubauer, 1999; Zimmer *et al.*, 2000). In analogy to Rubin *et al.*, 2015, Europa's interior is treated as a perfectly conducting sphere by the AIKEF hybrid model, being consistent with Galileo magnetometer data (see also Liuzzo *et al.*, 2015, 2016; Zimmer *et al.*, 2000 for details).

The bulk velocity of the (nearly) co-rotating plasma relative to Europa varies between $u_0 = 56 - 100$ km/s, the upstream density between $n = (18 - 200) \cdot 10^6\ \mathrm{m}^{-3}$ (Bagenal *et*

al., 2015; Kurth *et al.*, 2001), and the magnitude of the magnetospheric background field between $|\vec{B}| = 370 - 460$ nT (Kivelson *et al.*, 1999), depending on Europa's position within Jupiter's plasma sheet. The average mass of the incident ions is $m_i = 18.5$ amu and the temperature of the impinging ions and electrons is set to the same value of $k_B T_{i,e} =$ 100 eV (Kivelson *et al.*, 2004).

The extensions of our simulation domain are $-10\ R_E \leq x \leq 20\ R_E$, $-15\ R_E \leq y \leq 15\ R_E$, and $-30\ R_E \leq z \leq 30\ R_E$. The grid resolution varies between three regions of our simulation box (centered around (0,0,0)): 33 km for $|x, y, z| \leq 1.5\ R_E$, 66 km for $1.5\ R_E < |x, y, z| \leq 3\ R_E$ and 132 km outside of that cube. Analogous to the approach of Blöcker *et al.*, 2016, we discontinue the simulations as soon as the Alfvén wings reach the outer boundaries of the simulation domain in order to prevent reflections at those locations.

1.4.6 Ion Energy Spectra

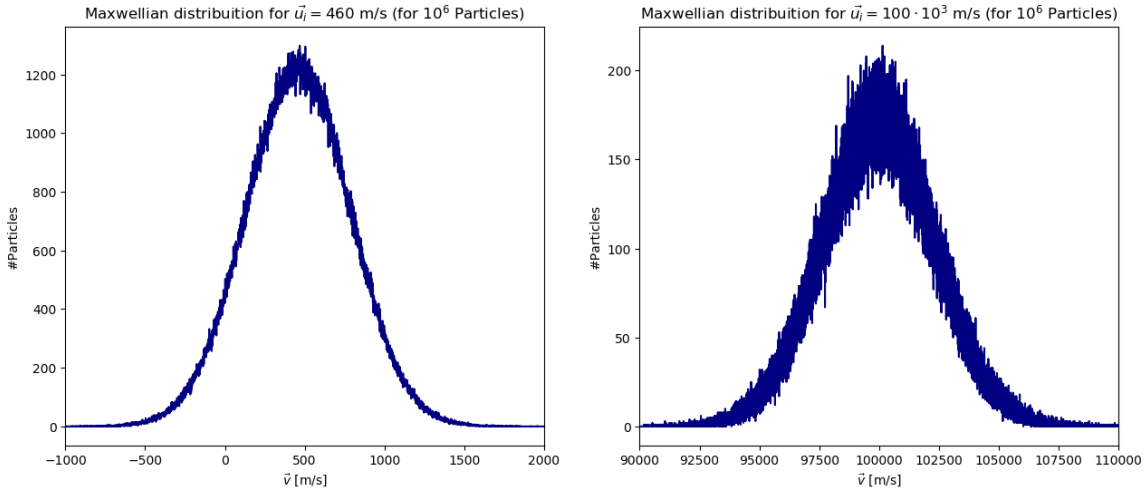

(a) (b)

Figure 1.8: Comparison of: (a) the narrow Maxwellian distribution of a water vapor plume at Europa ($\vec{u_i} = 460$ m/s, $T = 230$ K (Huybrighs *et al.*, 2017)) and a broader distribution (b) for the up streaming plasma at Europa ($\vec{u_i} = 100 \cdot 10^3$ m/s , $T = 100$ eV $\approx 11,600$ K (Kivelson *et al.*, 2004)) for 10^6 particles. Notice the different scaling for the axes in (a) and (b).

The velocity distribution of an undisturbed plasma follows the velocity distribution of

an idealized gas, which is a Maxwellian distribution:

$$f(\vec{v}) \propto \exp\left(-\frac{m(\vec{v}-\vec{u_i})^2}{2k_BT}\right), \tag{1.10}$$

where m is the mass of the ion species, $\vec{u_i}$ the plasma bulk velocity, k_B the Boltzmann's constant and T the temperature of the species. The temperature determines the width of the Maxwellian, whereas the bulk velocity of the plasma corresponds to a shift of the Maxwellian. The ions in the upstream plasma therefore are distributed over a broader velocity range (hot plasma ions $T \approx 11,600$ K, compared to cold plume ions $T = 230$ K) at higher velocities (see Figure 1.8, x-axis of a and b). The noise in Figure 1.8 originates from the finite particle number $n = 10^6$.

The kinetic energy of a particle is

$$E_{kin} = \frac{1}{2}m_i\vec{v}^2, \tag{1.11}$$

where m_i is the mass of the corresponding ion species and $\vec{v}$ denotes the particle's velocity. Thus, a broad velocity range results in a broad energy distribution of the upstream plasma ions, contrary to the narrow distribution of the cold plume ions.

Since AIKEF uses the "particle-in-cell" method (where the simulation domain is divided into discrete cells) and treats ions as particles, the particle number and velocity (which is related to their kinetic energy, see Equation 1.11) is calculated at every location within the simulation domain. We therefore are able to determine the ion energy distribution along spacecraft trajectories in AIKEF.

Figure 1.9 shows an ion energy spectrum generated with AIKEF for the Cassini flyby E3 of Enceladus. A crossing of the Enceladian plumes occurred near closest approach of the flyby. Three distinct regions are visible in the spectrum: in regions (a) and (c), we observe a broad energy distribution around 100 eV, and in region (b) a narrow distribution centered at a lower energy of ≈ 50 eV is visible. According to the velocity distribution (see

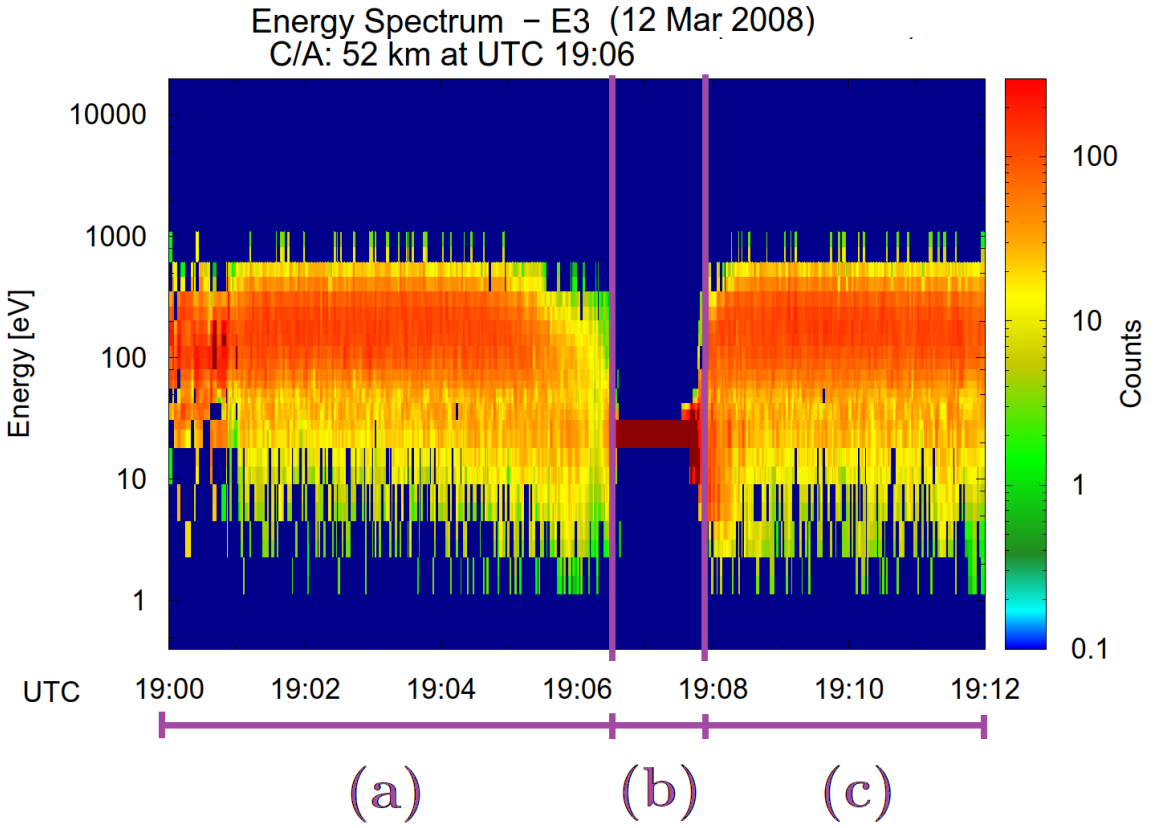

Figure 1.9: A synthetic ion energy spectrum of the Cassini E3 flyby through the plume of Enceladus, generated by the AIKEF hybrid code. The y-axis denotes the ion energy in eV on a logarithmic scale, whereas the color code is the particle number at a given location of the trajectory (x-axis). Three distinct regions from the flyby are highlighted: (a), (b) and (c).
(a) depicts the energy distribution until the spacecraft crosses the cold water vapor region of the plume flyby seen in (b). Similar to (a), (c) shows a region without plume ions. The Figure has been adapted from Dahlke, 2011.

Equation 1.10 and Figure 1.8), regions (a) and (c) correspond to the Maxwellian distribution of the unperturbed plasma flow, whereas (b) marks the cold plume plasma. This result is consistent with observations (Tokar *et al.*, 2009).

CHAPTER 2

GOALS OF THIS DISSERTATION

Up to this dissertation, only Blöcker *et al.*, 2016 and Jia *et al.*, 2018 have attempted to identify a plume near Europa using magnetic field and plasma data. Yet, the results of the MHD approach of Blöcker *et al.*, 2016 are inconclusive about the existence of a plume at Europa, due to limitations of their model (e.g., no ionospheric Hall effect). The study of Jia *et al.*, 2018 is currently under heavy debate because of inconsistencies in plasma data of the E12 flyby (Paterson and Collinson, 2019), the flyby analyzed in their study. Additionally, these studies do not incorporate potential flyby trajectories for upcoming missions. Furthermore, there exists no study that tests the hypothesis of Huybrighs *et al.*, 2016, which suggests the ability to detect signatures of a plume using ion energy spectrograms from close Europa flybys. This thesis therefore aims to answer the following questions:

1. **Detectability of plumes in magnetic field data:**

   (i) Are plumes visible in Galileo magnetic field data of close ($\leq$ 400km) Europa flybys?

   (ii) How do plumes contribute to the plasma interaction at Europa?

   (iii) How does the location of a plume with respect to the upstream magnetospheric flow direction change the structure and magnitude of the perturbations generated by Europa's plasma interaction?

   (iv) At which locations near Europa are the signatures of a plume most prominent, and where should future flyby trajectories occur to detect these features?

   (v) Do asymmetries in Europa's atmosphere potentially obscure the plume signature in MAG data?

2. **Detectability of plumes in ion energy spectra:**

    - Do ion energy distributions provide an additional framework for in-situ plume detectability at Europa?

The Goals are addressed as follows:

- Questions #1.(i) and #1.(ii) are addressed in chapter 3:

  Arnold, H., Liuzzo, L., & Simon, S. (2019). Magnetic signatures of a plume at Europa during the Galileo E26 flyby. Geophysical Research Letters, 46, 1149– 1157. https://doi.org/10.1029/2018GL081544

- Questions #1.(ii)-(v) are addressed in chapter 4:

  Arnold, H., Liuzzo, L., & Simon, S. (2020). Plasma interaction signatures of plumes at Europa. Journal of Geophysical Research: Space Physics, 125, e2019JA027346. https://doi.org/10.1029/2019JA027346

- Question #2 is addressed in chapter 5:

  Arnold, H., Simon, S., & Liuzzo, L. (2020). Applying Ion Energy Spectrograms to Search for Plumes at Europa. Journal of Geophysical Research: Space Physics, 125, e2020JA028376. https://doi.org/10.1029/2020JA028376

CHAPTER 3

MAGNETIC SIGNATURES OF A PLUME AT EUROPA DURING THE GALILEO E26 FLYBY

The following chapter has been published by Arnold *et al.*, 2019 in *Geophysical Research Letters* before submission of this dissertation. It is reproduced here in its entirety with the permission of John Wiley & Sons, Inc. The publication can be found under the following reference:

Arnold, H., Liuzzo, L., & Simon, S. (2019). Magnetic signatures of a plume at Europa during the Galileo E26 flyby. Geophysical Research Letters, 46, 1149– 1157. https://doi.org/10.1029/2018GL081544

3.1 Abstract

We analyze the magnetic field perturbations observed near Jupiter's icy moon Europa by the Galileo spacecraft during the E26 flyby on 03 January 2000. In addition to the expected large-scale signatures of magnetic fieldline draping and induction, the E26 dataset contains various prominent structures on length scales much smaller than the moon's radius. By applying a hybrid (kinetic ions, fluid electrons) model of Europa's interaction with the impinging magnetospheric plasma, we demonstrate that these fine-structures in the magnetic field are consistent with Galileo's passage through a water vapor plume whose source was located in Europa's orbital trailing, southern hemisphere. Considering the large-scale asymmetries of Europa's global atmosphere alone is not sufficient to explain the observed magnetic signatures. Combined with the recent identification of a plume during the earlier E12 flyby of Galileo, our results provide strong evidence that plume activity at Europa was a persistent phenomenon during the Galileo era.

3.2 Introduction

The smallest Galilean moon, Europa (radius $R_E = 1560.8\,\mathrm{km}$), likely hosts a global subsurface ocean (Kivelson *et al.*, 2000). The thickness of the ocean is suspected to be on the order of 100 km (Schilling *et al.*, 2007), whereas the estimates for the thickness of Europa's icy crust range from a few km up to 60 km (Hand and Chyba, 2007; Hussmann *et al.*, 2002; Schenk, 2002). Hubble Space Telescope (HST) observations in December 2012 revealed a localized increase of ultraviolet emission intensity near the south pole of Europa, associated with a surplus of oxygen and hydrogen. Roth *et al.*, 2014a demonstrated that the observed inhomogeneity in Europa's atmosphere could be interpreted as two water vapor plumes emanating near 180°W 75°S and 55°S, respectively, each with a scale height of about 200 km. A single, but broader plume could explain the observations equally well. However, subsequent HST observations in 2014 and 2015 could not identify the anomalies observed in 2012, indicating that (in contrast to the Enceladean plumes), the plumes at Europa seem to be transient in nature (Roth *et al.*, 2014b, 2016). Subsequently, Sparks *et al.*, 2016, 2017 were able to find new, equatorial locations of enhanced neutral column density through image post-processing of available HST data.

Europa orbits Jupiter at a distance of 9.38 R_J (radius of Jupiter $R_J = 71,492$ km. The moon is embedded in Jupiter's magnetosphere and its equatorial plasma sheet (Kivelson *et al.*, 2009). Since the orbital period of Europa is significantly larger than Jupiter's rotational period (the synodic period is 11.23 h with respect to Europa), sub-Alfvénic, magnetospheric plasma continuously impinges onto Europa's tenuous atmosphere and ionosphere. The moon's ionosphere is mainly generated by electron impact ionization, with the contribution of solar UV ionization being an order of magnitude smaller (Saur *et al.*, 1999). Mass loading of the magnetospheric plasma by Europa's ionosphere decelerates the impinging flow and deflects it around the moon (e.g., Rubin *et al.*, 2015). The magnetospheric field drapes around the obstacle, forming Alfvén wings at larger distances to Europa (Neubauer,

1980; Neubauer, 1998).

Driven by the 9.6° tilt between Jupiter's magnetic and rotational axes, the ambient magnetospheric field near Europa exhibits an oscillation at Jupiter's synodic rotation period. This time variability induces a secondary magnetic field in Europa's conducting subsurface ocean, which has a dipolar shape outside of the moon (Khurana *et al.*, 1998; Zimmer *et al.*, 2000). Therefore, in addition to Europa's atmosphere/ionosphere, the magnetospheric plasma interacts with the (time-varying) dipole field induced in Europa's subsurface ocean (Kivelson *et al.*, 1999). The induced dipole contributes to the plasma deflection and reduces the cross-sections of the two Alfvénic fluxtubes, compared to a scenario without induction (Neubauer, 1999; Volwerk *et al.*, 2007).

However, this picture considers only the influence of Europa's global atmosphere and induced field on the plasma interaction, but not the impact of a possible plume. A localized inhomogeneity in the atmosphere generates a tube-like region of locally enhanced current density and flow deceleration within the main Alfvén wing, referred to as an Alfvén winglet by Blöcker *et al.*, 2016. A plume source in, e.g., Europa's southern hemisphere, will also break the symmetry of the Alfvén wings between the moon's northern and southern hemispheres (Blöcker *et al.*, 2016). Due to the translational invariance along their characteristics (Neubauer, 1980) the Alfvén wings and associated asymmetries can extend to arbitrarily large distances from Europa. This facilitates a "remote" detection of plumes in magnetic field data from distant Europa flybys.

Out of the 12 Galileo flybys of Europa, only the E12 (on 16 December 1997) and E26 (on 3 January 2000) flybys passed at a low altitude of only 400 km to Europa's surface, an altitude of the same order as the scale height of the plume found by Roth *et al.*, 2014a. Both of these flybys occurred in the orbital trailing hemisphere of Europa: the E12 flyby occurred at equatorial latitudes, whereas the E26 flyby occurred at more southern latitudes (see Figure 3.1). During E26 Europa was located at 03:00 local time and at a distance of 1.5 R_J below Jupiter's magnetospheric current sheet. As suggested by Blöcker *et al.*, 2016,

transverse currents within the plumes should leave a clear imprint in Galileo magnetometer data from such close flybys. Indeed, magnetic field observations from both flybys reveal sharp, highly localized perturbations in all three components near closest approach (C/A) of the spacecraft that are superimposed on the signatures of the main Alfvén wings.

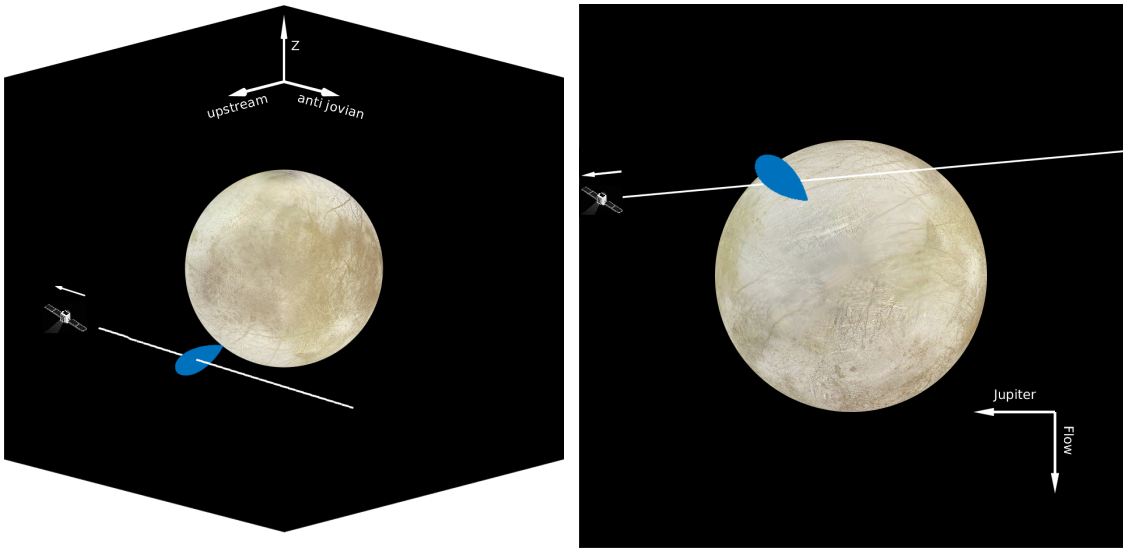

(a) (b)

Figure 3.1: Geometry of the Galileo E26 flyby of Europa in EPhiO coordinates, as seen (a) from the upstream, Jupiter-averted side (b) when looking at the moon's southern hemisphere. The white line denotes the trajectory of the spacecraft. The blue isosurface illustrates the position and orientation of the plume included in simulation run #1 (see section 2 for details). The E26 trajectory is located within the $z \approx -0.8 R_E$ plane of the EPhiO.

The black lines in Figure 3.2 display magnetometer data from the E26 flyby in EPhiO coordinates. In this Cartesian coordinate system, the x axis is aligned with the corotational flow direction, the y axis points towards Jupiter and the z axis completes the right-handed system. The origin of the EPhiO system coincides with the center of Europa. The B_x component observed during E26 shows a broad enhancement between 17:59:00 and 18:05:00, associated with the bending of the field toward downstream in the southern Alfvén wing. Superimposed on the main Alfvén wing signature is a double-peak structure (between 17:59:30-18:01:00) with a magnitude of about $B_x = 150$ nT at the two spikes and a minimum of $B_x = 25$ nT in between the enhancements. The observed perturbation in the B_y

component mainly consists of a single, prominent enhancement of 100 nT near 18:01:00. The B_z component shows multiple drops and enhancements during the same interval as B_x.

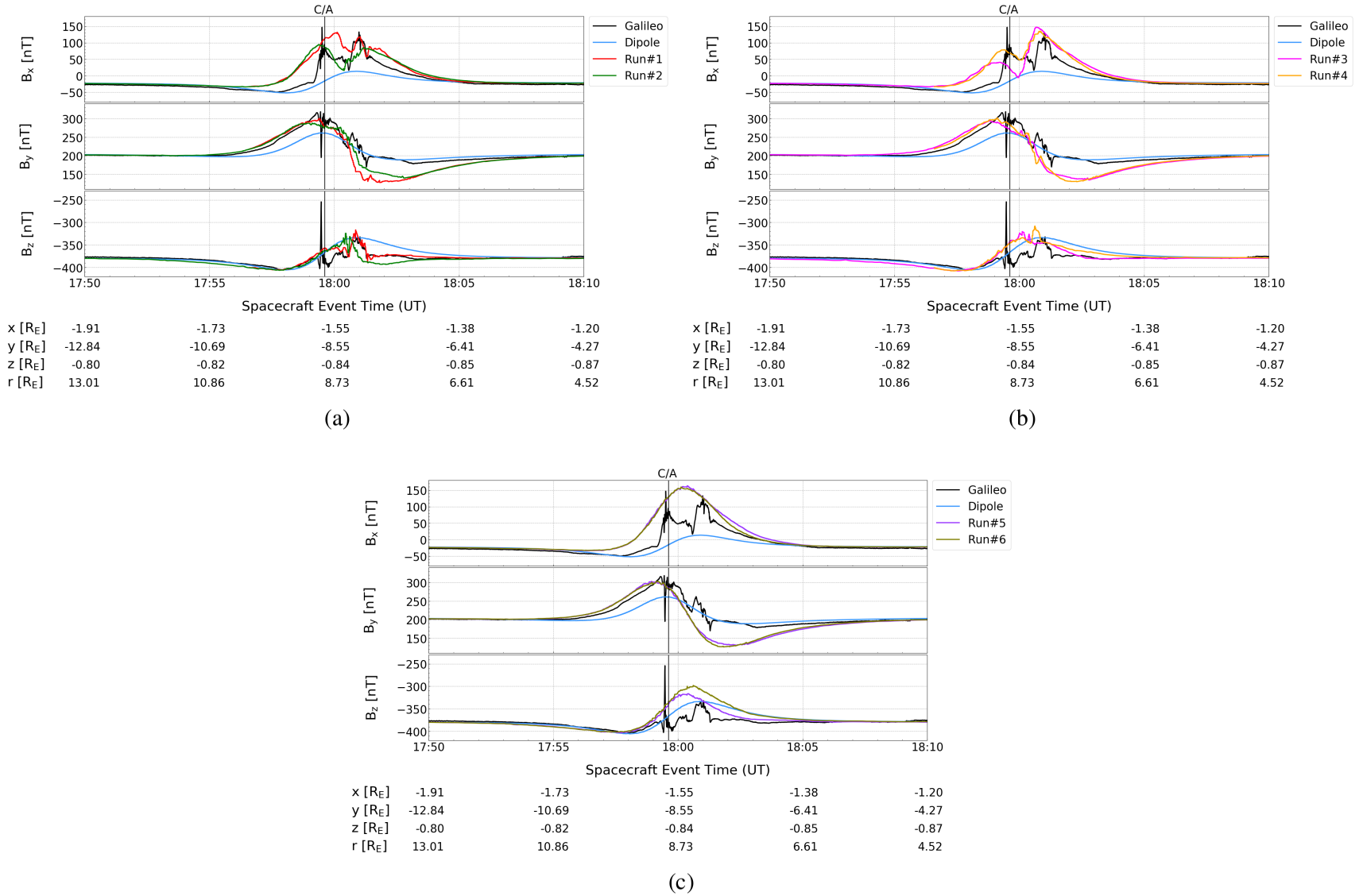

Figure 3.2: Modeled and measured magnetic field along the E26 trajectory. (a,b,c) Each of the three panels illustrates the magnetic field components observed by Galileo (black) as well as the dipolar magnetic field associated with induction in Europa's subsurface ocean alone (light blue). In addition, the modeled magnetic fields from two of the hybrid simulation runs are shown in each panel. To facilitate the identification of fine structures in the magnetic field, each panel contains only the results of two simulations. The vertical black line denotes Galileo's closest approach to Europa at 17:59:37.

Blöcker *et al.*, 2016 applied a three-dimensional magnetohydrodynamic model with a single plume in Europa's southern trailing hemisphere to investigate whether the magnetic perturbations measured during E26 could contain any hints of plume activity during the flyby. With this model, Blöcker *et al.*, 2016 were able to qualitatively reproduce the outbound enhancement in B_x. However their model severely underestimated the magnitude of the B_x peak in the inbound region. Also, the width of the modeled B_x peak in the outbound region was much larger than observed by Galileo. The model of Blöcker *et al.*, 2016 could not reproduce the observed B_y enhancement between 17:56:00-18:02:00. The perturbations in the observed B_z component could not be matched in magnitude nor structure. Blöcker *et al.*, 2016 ascribed the discrepancies between model and observations to the missing ionospheric Hall effect and the radially symmetric atmospheric density profile applied in their model. Their model was therefore unable to determine whether or not Galileo had passed through a plume during the E26 encounter. Several other models tried to explain the magnetic field data from the E26 flyby without inclusion of a local plume source (Rubin *et al.*, 2015; Schilling *et al.*, 2008). While these studies were able to describe the magnitude of the broad B_x enhancement associated with the southern Alfvén wing crossing (during 17:59:00-18:05:00), they did not succeed in explaining the double-peaked fine structure within the Alfvén wing.

Magnetic field data from the E12 flyby display similarly localized perturbations on a scale smaller than the radius of Europa. Using the BATS-R-US multi-fluid MHD model, Jia *et al.*, 2018 searched for plume signatures in magnetic field and plasma data from the E12 encounter. These authors were able to attribute the observed sharp enhancements and drops in all three magnetic field components over a distance of 1,000 km near C/A to a plume at Europa. However, the model of Jia *et al.*, 2018 underestimated the observed amplitudes of the perturbations in B_x and B_y by more than a factor of two. The density enhancement observed by the Galileo Plasma Wave Spectrometer near C/A was reproduced by the model of Jia *et al.*, 2018. However, the structures in the plasma density observed in the outbound

region were not matched by their simulation. Overall, Jia *et al.*, 2018 provided strong evidence that the location and extension of the magnetic field and plasma perturbations observed during the E12 flyby were generated by a plume.

Building upon the work of Blöcker *et al.*, 2016 and the recent, successful plume identification by Jia *et al.*, 2018, the goal of our study is to search Galileo magnetic field data from E26 for evidence of a plume in Europa's orbital trailing, southern hemisphere.

3.3 Model Description

We apply the AIKEF (Adaptive Ion-Kinetic Electron-Fluid) hybrid code (Müller *et al.*, 2011) for our simulations, which treats ions as particles and electrons as a massless, charge-neutralizing fluid. In contrast to the MHD approach of Schilling *et al.*, 2008 and Blöcker *et al.*, 2016, AIKEF can describe asymmetries in the plasma flow due to the ionospheric Hall effect as well as flow shear between the magnetospheric plasma and the plasma emanating from Europa (e.g., from its ionosphere or a plume source). AIKEF has already been successfully applied to model Cassini magnetic field observations from multiple flybys through the Enceladus plume (Kriegel *et al.*, 2009, 2011, 2014).

We use similar magnetospheric upstream parameters as Rubin *et al.*, 2015 and Blöcker *et al.*, 2016 to facilitate a comparison to their results for the E26 flyby. Since the bulk velocity of the (nearly) corotating plasma relative to Europa is not constrained through observations from E26, we use a value of $u_0 = 100$ km/s in agreement with Bagenal *et al.*, 2015. The upstream number density in the simulations ($n = 30 \cdot 10^6\ \mathrm{m}^{-3}$) is consistent with the range of values measured by Galileo during the flyby (Kurth *et al.*, 2001). The plasma density during E26 was about a factor of 20 smaller than the anomalously high density observed during E12 (Kurth *et al.*, 2001), suggesting a much weaker plasma interaction during E26. For the average mass of the incident, singly-charged ions we use $m_i = 18.5$ amu (Kivelson *et al.*, 2004). The temperature of the impinging ions and electrons is set to the same value of $k_B T_{i,e} = 100$ eV (Kivelson *et al.*, 2004), and the magnetospheric

background field during the E26 flyby is $\vec{B}_0 = (-22, 205, -379)$ nT (see Kivelson *et al.*, 1999 and Figure 3.2). These parameters result in an Alfvénic Mach number for the upstream plasma of $M_A = 0.25$.

Due to the vast difference in the timescales of the plasma interaction and induction effects (minutes compared to hours, see Seufert *et al.*, 2011), the field induced in Europa's subsurface ocean during the E26 flyby can be represented in our model as a static dipole moment (Neubauer, 1999; Zimmer *et al.*, 2000). In analogy to Rubin *et al.*, 2015, Europa's interior is treated as a perfectly conducting sphere (see also Kivelson *et al.*, 1999; Zimmer *et al.*, 2000 for details).

In our model, Europa's atmosphere consists of molecular oxygen, which was found to be the dominant species (Hall *et al.*, 1995; McGrath *et al.*, 2009). Sputtering of Europa's surface is not uniform: Pospieszalska and Johnson, 1989 as well as Cassidy *et al.*, 2013 showed that the sputtering rate decreases from the trailing hemisphere towards the leading hemisphere. Therefore, for the neutral density distribution we use an analytical description similar to the model of Rubin *et al.*, 2015. The density profile in the trailing n_T and leading n_L hemispheres reads

$$\begin{aligned} n_L(h) &= n_0 \cdot \exp\left(-\tfrac{h}{h_0}\right), && 90^\circ < \alpha \leq 180^\circ \quad , \\ n_T(h,\alpha) &= n_L(h) \cdot (1 + A \cdot \cos(\alpha)), && \alpha \leq 90^\circ \quad , \end{aligned} \tag{3.1}$$

with the radial distance $h = |\vec{r}| - R_E$ (where $\vec{r}$ is the position vector from Europa's center) to Europa's surface, the neutral scale height $h_0 = 50$ km and the surface density $n_0 = 1{\cdot}10^{14}$ m^{-3}. The symbol α denotes the angle between the position $\vec{r}$ and the negative x axis (which points into the trailing/ramside hemisphere). The parameter A represents the strength of the trailing/leading asymmetry. We consider two cases: $A = 0$, similar to the symmetric, barometric profile of Blöcker *et al.*, 2016 and $A = 10$. In this way, we can systematically assess the potential of large-scale/global atmospheric asymmetries to obstruct any (locally) observable plume signatures in the magnetic field. The O_2 column

density in our runs therefore ranges from $5.5 \cdot 10^{19}$ m^{-2} for $A = 10$ to $5 \cdot 10^{18}$ m^{-2} for $A = 0$, consistent with the interval of $10^{18} - 10^{19}$ m^{-2} inferred from HST observations (Hall *et al.*, 1995; Plainaki *et al.*, 2018; Saur *et al.*, 1998).

We also consider a single water vapor plume with the neutral density profile suggested by Roth *et al.*, 2014a:

$$n_P(h, \Delta\theta) = n_{P,0} \cdot \exp\left[-\left(\frac{h}{h_p}\right)^2 - \left(\frac{\Delta\theta(\vec{P})}{h_\theta}\right)^2\right] \quad , \tag{3.2}$$

where $\Delta\theta(\vec{P})$ represents the angular distance from the plume axis $\vec{P}$ (which is *not* necessarily perpendicular to Europa's surface), h_p the scale height of the plume, h_θ the opening angle of the plume and $n_{P,0}$ the surface number density of the plume. Thus, the neutral density profile of the plume is rotationally symmetric around the plume axis $\vec{P}$. In our simulations we use $h_p = 200$ km, $h_\theta = 15°$ and $n_{P,0} = 3.9 \cdot 10^{15}$ m^{-3}, resulting in a column density of H_2O along the plume axis of $7.8 \cdot 10^{20}$ m^{-2}. This value is consistent with the range of values inferred from HST observations: $1.5 \cdot 10^{20}$ m^{-2} (Roth *et al.*, 2014a) to $2.3 \cdot 10^{21}$ m^{-2} (Sparks *et al.*, 2016). The location of the plume's "footpoint" and orientation of its symmetry axis $\vec{P}$ with respect to the surface are free parameters in our model. However, we place its footpoint in the vicinity of the Butterdon Linea (see Table 1 of Doggett *et al.*, 2009) which is the surface feature closest to the E26 trajectory. Assuming that the generation mechanism of plumes on Europa is similar to that of the plumes at Enceladus (Porco *et al.*, 2006), we allow an inclination of the plume axis $\vec{P}$ against the local radial/zenith direction at its footpoint (see Jia *et al.*, 2018). The footpoint of the plume at Europa's surface is located at

$$\vec{F}(\theta_F, \phi_F) = R_E(\sin(\theta_F)\cos(\phi_F), \sin(\theta_F)\sin(\phi_F), \cos(\theta_F)) \quad , \tag{3.3}$$

where ϕ_F is measured in the right-handed EPhiO coordinates, whereas $\theta_F = 0°$ marks

Europa's north pole and $\theta_F = 180^\circ$ Europa's south pole, respectively. The inclination of the plume axis $\vec{P}$ against the local radial direction at the footpoint $\vec{F}$ is defined by the angles $\tilde{\theta} = \theta - \theta_F$ and $\tilde{\phi} = \phi - \phi_F$; i.e., $\tilde{\theta} = 0^\circ$, $\tilde{\phi} = 0^\circ$ means that the plume axis $\vec{P}$ is perpendicular to the surface. We have carried out multiple simulation runs for various combinations of footpoint locations and orientations of the plume axis. The following four sets of parameters were found to yield best possible agreement between modeled and measured magnetic field perturbations: run #1: $A = 10$, $\vec{P}(\theta, \phi, \tilde{\theta}, \tilde{\phi}) = (140^\circ, 300^\circ, -20^\circ, -20^\circ)$; run #2: $A = 10$, $\vec{P}(\theta, \phi, \tilde{\theta}, \tilde{\phi}) = (140^\circ, 300^\circ, 0^\circ, -10^\circ)$; run #3: $A = 10$, $\vec{P}(\theta, \phi, \tilde{\theta}, \tilde{\phi}) = (140^\circ, 300^\circ, 0^\circ, 35^\circ)$ and run #4: $A = 10$, $\vec{P}(\theta, \phi, \tilde{\theta}, \tilde{\phi}) = (135^\circ, 305^\circ, 0^\circ, 35^\circ)$. For reference, we have also carried out two simulations *without* a plume, using an asymmetric atmosphere (A=10) in run #5 and a symmetric atmosphere (A=0, with a higher base density of $11 \cdot n_0$, to compare it with run #5) in run #6 .

In our model, the neutral atmosphere and plume are ionized by electron impacts, which is the dominant ionization process at Europa (Saur *et al.*, 1998). In analogy to Schilling *et al.*, 2008, Blöcker *et al.*, 2016, and Jia *et al.*, 2018 we calculate the ion production rate by multiplying the electron impact ionization rate $f_{imp}(T_e)$ for H_2O and O_2 with the respective neutral density profile. To derive the electron impact ionization rate of each species, we assume a Maxwellian velocity distribution for the ionizing electrons and integrate over their energy-dependent ionization cross sections (taken from the National Institute of Standards and Technology database (Kim *et al.*, 2004)), see also the approach of Banks and Kockarts, 1973. This leads to constant ionization rates of $2{\cdot}10^{-6}$ s^{-1} for H_2O^+ and $2.3{\cdot}10^{-6}$ s^{-1} for O_2^+. The assumption of a *constant* ionization rate is consistent with the approach of Blöcker *et al.*, 2016 and Jia *et al.*, 2018. Our model also considers loss of ionospheric O_2^+ and H_2O^+ ions due to dissociative recombination, with the recombination rates given in

Schunk and Nagy, 2000:

$$\begin{aligned} \alpha_{O_2^+} &= 2 \cdot 10^{-13} \left(\tfrac{300}{T_e}\right)^{0.7} && \mathrm{m^3 s^{-1}} \quad , \\ \alpha_{H_2O^+} &= 1.03 \cdot 10^{-9} \left(T_e\right)^{-1.111} && \mathrm{m^3 s^{-1}} \quad . \end{aligned} \tag{3.4}$$

The extensions of our simulation domain are $-10\ R_E \leq x \leq 20\ R_E$, $-15\ R_E \leq y \leq 15\ R_E$, and $-30\ R_E \leq z \leq 30\ R_E$. The grid resolution varies between three regions of our simulation box (centered around (0,0,0)): 33 km for $|x, y, z| \leq 1.5\ R_E$, 66 km for $1.5\ R_E < |x, y, z| \leq 3\ R_E$ and 132 km outside of that cube. Analogous to the approach of Blöcker *et al.*, 2016, we discontinue the simulations as soon as the Alfvén wings reach the outer boundaries of the domain.

3.4 Results

In Figure 3.2(a)-(c), the comparison between the modeled (runs #1-6 from section 2) and measured magnetic field signatures (black lines) is depicted. For reference, we also show the dipolar field induced in the subsurface ocean (without any contributions from plasma currents, light blue line) in all panels.

The B_x component in all six runs shows a broad enhancement between 17:57:00 and 18:04:00, corresponding to the crossing of the southern Alfvén wing, similar to the results of Schilling *et al.*, 2007, Rubin *et al.*, 2015, and Blöcker *et al.*, 2016. Runs #1 to #4 (which include a plume) also reveal the prominent double-peak feature in B_x between 17:59:30 and 18:01:00. The relative strength of the two enhancements varies between our simulations. Runs #3 and #4 display a weaker inbound (18:00:00) than outbound peak (18:01:30) in B_x, whereas the magnitude and shape of the two peaks in run #2 are nearly symmetric around the local minimum (18:00:30). In run #1, the inbound enhancement in B_x is about 10 nT stronger than the outbound enhancement. The fine structure of the B_x signature observable along the E26 trajectory is highly sensitive to even slight changes in the orientation and footpoint of the plume axis $\vec{P}$. However, the width of the modeled B_x signature in all four

runs with a plume is consistent with the Galileo data.

All six model runs produce a bipolar perturbation in the B_y component: an enhancement in the inbound region is followed by a decrease in the outbound region. Comparison to the pure induction signal (light blue line) illustrates that the inbound B_y signature is generated when the dipole field is compressed by the plasma interaction, thereby amplifying the perturbations associated with an induced dipole field alone. The magnitude and width of the B_y enhancement observed in the inbound region are well reproduced by all six model runs. However, compared to observations, the contribution of plasma currents is overestimated in the outbound region. All other models which have been applied to E26 without a plume (Rubin *et al.*, 2015; Schilling *et al.*, 2007) as well as with a plume (Blöcker *et al.*, 2016) produced a similar outbound depletion in B_y as our model. The discrepancy in the outbound region of B_y may be caused by a locally enhanced current density within the plume that is not reproduced by the analytical density profile applied here (Equation 3.2). An analysis of the two-dimensional magnetic field structures in the E26 flyby plane (Figure 3.3, see below) will shed additional light on the origin of this structure. If a plume is considered, only the sharp flank between the inbound and outbound signatures in B_y (17:59:00-18:00:01) changes quantitatively. The modeled B_y component therefore contains the least indicative signatures for the presence of a plume.

The observed B_z component displays a bipolar structure as well: an enhanced $|B_z|$ was detected by Galileo in the inbound region (17:51:00-17:59:30), followed by a decrease in the outbound region immediately after 17:59:30. The inbound enhancement of $|B_z|$ is nearly identical to the pure induction signal, indicating that plasma currents made only a weak contribution to this feature. The width and magnitude of the inbound $|B_z|$ increase are well reproduced by all six hybrid runs. The B_z perturbation observed outbound is highly localized: it possesses an extension of only $0.1\ R_E$ along the flyby trajectory (crossed between 18:01:00 and 18:02:00) and is bounded by discontinuity-like jumps of B_z on both sides. Furthermore, the location of the outbound depression in $|B_z|$ nearly coincides with

the outbound spike seen in B_x (which could clearly be associated with Galileo's passage through a plume). The model's ability to reproduce the pillar-like outbound depletion of $|B_z|$ near 18:01:00 strongly depends on the plume orientation and location of its footpoint: even slight changes of either lead to a drastic change of width and magnitude of the modeled B_z structure (e.g., run #1 versus run #4). The best agreement in both, width and magnitude of the outbound B_z feature is achieved in run#1: in this case, model and observation are nearly indistinguishable. The model used by Blöcker *et al.*, 2016 was not able to reproduce the observed orientation of B_z *anywhere* in the perturbed segment.

In conclusion, each of the four runs reproduces certain features of the observed magnetic field components better than the other three. Therefore, we refrain from choosing a "best fit" run.

For comparison, Figure 3.2(c) displays the modeled magnetic field signatures for the case of an asymmetric (run #5) and symmetric (run #6) global atmosphere, but *without* a plume included. Neither of these runs is able to reproduce any of the magnetic fine-structures observed by Galileo around closest approach, consistent with the modeling results of Schilling *et al.*, 2008 and Rubin *et al.*, 2015 (see Figures 10 in both works). This provides strong additional evidence that the magnetic signatures observed around closest approach of E26 were (partially) generated by a localized atmospheric inhomogeneity with an extension much smaller than Europa. A comparison of the magnetic signatures from runs #5 and #6 also indicates that a global ram/wake asymmetry of Europa's atmosphere makes only minor quantitative contributions to the magnetic field signatures observable upstream of the moon: it mainly affects the B_z signatures in the outbound region.

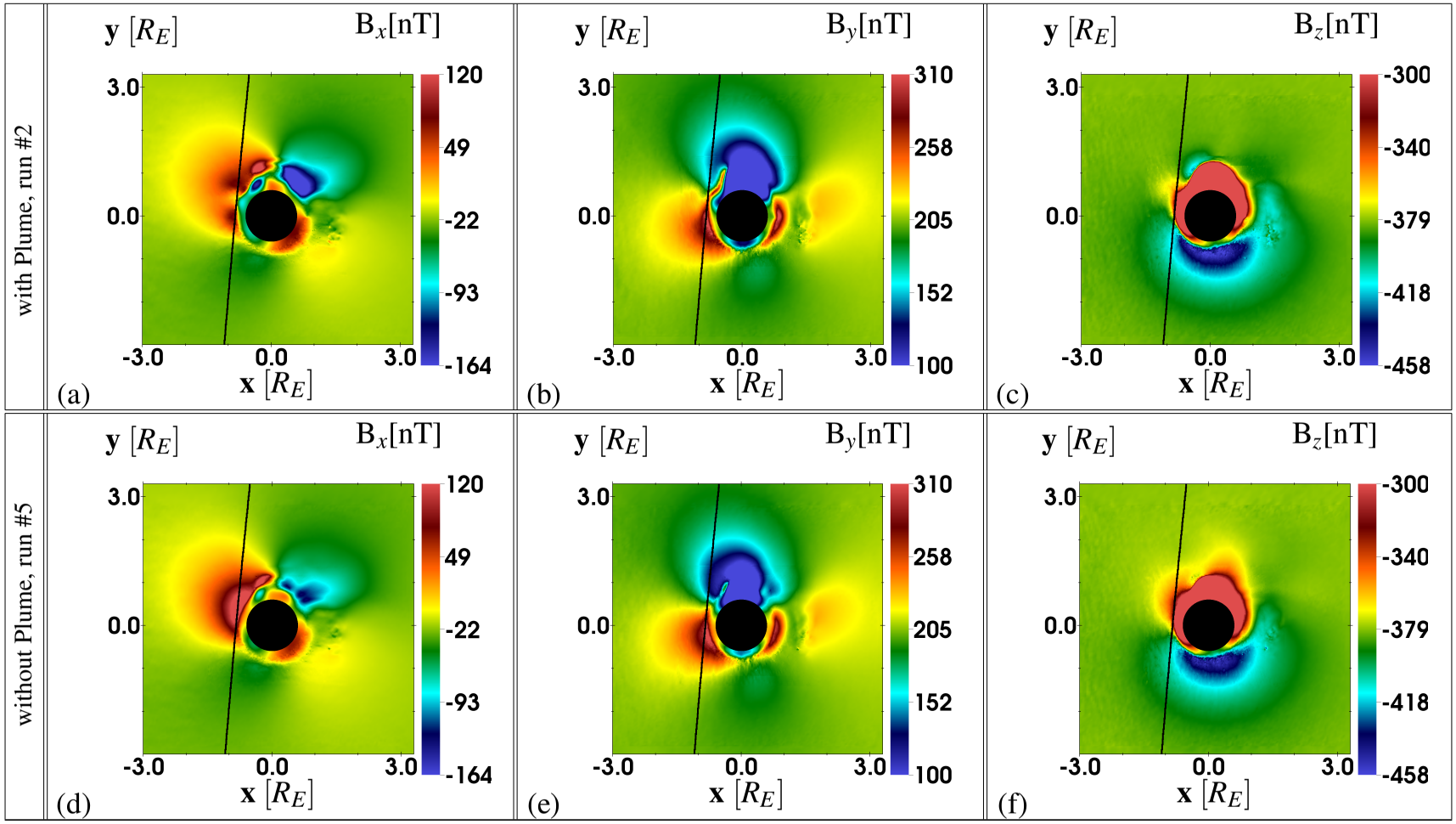

Figure 3.3: Two-dimensional illustration of the magnetic field components (B_x, B_y, B_z) close to Galileo's E26 flyby, in the plane of $z = -0.8\ R_E$. For a scenario with (run #2, panels (a)–(c)) and without (run #5, panels (d)–(f)) a plume, the figure illustrates Europa's magnetic environment near the E26 trajectory. The solid black lines indicate the flyby trajectory.

Figure 3.3 shows two-dimensional cuts through the magnetic field near the flyby plane at $z = -0.8\ R_E$. Results are displayed for run #2 (plume included, panels (a)-(c)) and run #5 (no plume, panels (d)-(f)). Note that the background field $\vec{B_0}$ is not parallel to any plane of the EPhiO coordinate system.

In the model results with the plume included (see Figure 3.3(a)), the B_x component exhibits three distinct signatures along the trajectory: the two enhanced (dark red) outer segments of the double-peak structure and the narrow region in between (orange/yellow), where B_x is reduced compared to the peak values at the spikes. A similar B_x depletion occurs in all four runs with a plume included. In the run without the plume (see Figure 3.3(d)), the region of reduced B_x is moved closer to Europa because the local bulge in the field generated by the plume is no longer present. Changes due to a plume in the overall B_x topology are rather subtle and occur on length scales much smaller than Europa's radius. Therefore, if the spacecraft trajectory during the E26 flyby were only slightly displaced, an unambiguous identification of a local plume source may have been severely complicated.

For B_y (see panels Figure 3.3(b) and Figure 3.3(e)) the model displays only minor quantitative differences between both cases, which is consistent with the results obtained along the flyby trajectory (see Figure 3.2). It is important to note that Figure 3.3(b) displays a "finger-like", narrow region of enhanced B_y (depicted in dark red and yellow) along the outbound segment of the E26 trajectory. This enhancement locally interrupts the extended region of negative B_y perturbation in the Jupiter-facing hemisphere associated with field line draping. A slightly different plume orientation or a slightly different shape of the neutral gas profile may shift this feature closer the path of the spacecraft, thereby eliminating large portions of the outbound decrease in B_y visible in our simulations. Using the plume model from Equation 3.2, we did not find a parameter set that *simultaneously* explains B_x, B_z as well as the observed, weak dip in the outbound segment of B_y. However, our results clearly indicate that a plume source may indeed generate a highly localized channel through the region of reduced B_y, along which Galileo may have traveled during the E26

flyby. Due to the uncertainties in the upstream conditions (especially the bulk velocity of the incident magnetospheric flow during E26 is not well constrained) and the numerous degrees of freedom in the shape and orientation of the plume model, the parameter space to be explored for improving agreement in the outbound segment of B_y is vast. This effort is beyond the scope of the present study.

Panels Figure 3.3(c) and Figure 3.3(f) depict two-dimensional cuts through the modeled B_z component. In the Jupiter-averted hemisphere ($y < 0$) we see an extended region of enhanced $|B_z|$, associated with the induced dipole alone. In the Jupiter-facing hemisphere, the region of locally reduced $|B_z|$ (which is strongly shaped by plasma currents) is slightly different between panels Figure 3.3(c) and (f). Galileo just "scratched" the outer regions of this structure. In the run with a plume included, the outbound B_z feature is more confined, which explains the localized, narrow "pillar" visible in both, the modeled and the observed magnetic field time series.

3.5 Summary and Concluding Remarks

Our model shows that a plume source is required to explain the fine structures in the magnetic field perturbations observed by Galileo during the E26 flyby of Europa. The modeled magnetic signatures along the E26 trajectory are highly sensitive to the plume orientation and the location of the plume's footpoint at Europa's surface. Multiple sets of plume parameters were found to be in similarly good agreement with observations. It is therefore not feasible to quantitatively constrain parameters of the plume (e.g., the neutral gas content or shape) based on magnetic field observations alone. In addition to the E12 flyby (Jia *et al.*, 2018), E26 has become the second Galileo encounter with a strong indication of plume activity. Although yet unnoticed, plumes at Europa seem to have been a persistent phenomenon during the Galileo area.

CHAPTER 4

PLASMA INTERACTION SIGNATURES OF PLUMES AT EUROPA

The following chapter has been published by Arnold *et al.*, 2020a in the *Journal of Geophysical Research (Space Physics)* before submission of this dissertation. It is reproduced here in its entirety with the permission of John Wiley & Sons, Inc. The publication can be found under the following reference:

Arnold, H., Liuzzo, L., & Simon, S. (2020). Plasma interaction signatures of plumes at Europa. Journal of Geophysical Research: Space Physics, 125, e2019JA027346. https://doi.org/10.1029/2019JA027346

4.1 Abstract

The goal of our study is to present a systematic modeling framework for the identification of water vapor plumes in plasma and magnetic field data from spacecraft flybys of Europa. In particular, we determine the degree to which different plume configurations can be obscured by the interaction of Jupiter's magnetospheric plasma with Europa's induced dipole field and its global atmosphere. We apply the hybrid model AIKEF (kinetic ions, fluid electrons) to investigate the effect of inhomogeneities in Europa's atmosphere (plumes) on the plasma interaction with the Jovian magnetosphere. To systematically assess the magnitude and structure of the perturbations associated with the plume-plasma interaction at Europa, we vary the plume location across Europa's surface whilst considering different symmetric and asymmetric density profiles of the moon's global atmosphere. To isolate the impact of a plume on Europa's magnetospheric environment, we also conduct model runs without any global atmosphere. To quantify the magnetic perturbations caused by plumes we analyze the field components along hypothetical spacecraft trajectories through each plume. Conclusions of our study are: (1) Localized regions of stagnant flow are most indicative of

the presence of a plume. (2) The visibility of plumes in the magnetic field strongly depends on the density profile (whether it is symmetric or asymmetric) of the global atmosphere. (3) The presence of an induced dipole complicates the identification of magnetic signatures associated with a plume and dominates Europa's magnetic environment in its intermediate vicinity. (4) Complex fine structures are visible in the tail of escaping plume ions.

4.2 Introduction

Europa, Jupiter's innermost icy moon, orbits its parent planet at a distance of 9.38 R_J (radius of Jupiter $R_J = 71,492$ km), and is tidally locked to the planet. The moon is located within Jupiter's magnetosphere (Smith *et al.*, 1974) and its plasma sheet (Kivelson *et al.*, 2009). Europa's orbital period is significantly larger than Jupiter's rotational period, resulting in a synodic period of 11.23 h with respect to Europa. Subsonic and subalfvénic magnetospheric plasma therefore continuously impinges onto the moon's atmosphere and ionosphere (Kivelson *et al.*, 2004).

Impinging magnetospheric particles sputter molecules off Europa's icy surface, thereby generating a thin atmosphere which mostly consists of molecular oxygen O_2 (Burger and Johnson, 2004; Ip *et al.*, 1998; McGrath *et al.*, 2009). The magnetospheric particle precipitation is not homogeneous, but depends strongly on the orientation of the magnetospheric background field (Cassidy *et al.*, 2013) and also, on the local electromagnetic field perturbations near Europa (Breer *et al.*, 2019). The intensity of the sputtering decreases from Europa's ramside to its wake (Pospieszalska and Johnson, 1989), as the flux of the impinging magnetospheric particles is reduced in the moon's wakeside hemisphere (Cassidy *et al.*, 2013). Yet, the detailed understanding of the mechanisms responsible for the formation of Europa's O_2 atmosphere are still under heavy debate (Plainaki *et al.*, 2018). The neutral atmosphere is partially ionized, mainly by electron impact ionization, with the contribution of solar UV ionization being an order of magnitude weaker (Saur *et al.*, 1999). The large-scale asymmetries in the atmosphere are imprinted onto the shape of Europa's

ionosphere.

The impinging magnetospheric plasma slows down in the vicinity of the moon due to mass loading from its ionosphere. Newly generated ionospheric ions are picked up by the ambient electromagnetic fields and are incorporated into the magnetospheric flow, causing a deceleration of the flow and an increase of the magnetic field strength upstream of the moon. The magnetospheric field drapes around the obstacle, generating Alfvén wings at larger distances to the moon which propagate northward and southward along the Alfvén characteristics $\vec{u}_0 \pm \vec{v}_{A0}$, where $\vec{u}_0$ is the bulk velocity of the magnetospheric upstream plasma and $\vec{v}_{A0}$ is the Alfvén velocity (Neubauer, 1980; Neubauer, 1998). In addition to Europa's atmosphere and ionosphere, the magnetospheric plasma interacts with the (time-varying) dipole field induced in the moon's subsurface ocean (Kivelson *et al.*, 1999; Zimmer *et al.*, 2000), which is driven by the 9.6° tilt between Jupiter's magnetic and rotational axes. This induced dipole field is compressed at Europa's ramside and stretched at its wake-side, locally contributing to transverse currents and therefore to the Alfvén wings (Liuzzo *et al.*, 2016). The coupling of the dipole-magnetosphere interaction and the ionospheric mass loading reduces the cross section of the Alfvén wings and generates a slight displacement of the wings with respect to the moon (Neubauer, 1999; Volwerk *et al.*, 2007).

However, the view of Europa's neutral gas environment was changed drastically when, in December 2012, Hubble Space Telescope (HST) observations of the moon's ultraviolet (UV) aurora revealed a localized surplus of UV emission intensity near its south pole, associated with an increase in oxygen and hydrogen column densities. Roth *et al.*, 2014a showed that two water vapor plumes emanating near 180° W 75° S and 55° S, each with a scale height of about 200 km, quantitatively match the HST observations. Through image post-processing, Sparks *et al.*, 2016 found hints of additional transient plumes, located near the south pole at 271° W 63° S and in the equatorial region at 275.7° W 16.4° S. However, subsequent observations from HST could not identify the anomalies observed in 2012 (Roth *et al.*, 2014a, 2016).

Blöcker *et al.*, 2016 used a three-dimensional magnetohydrodynamic model to investigate the detectability of a plume in Europa's magnetic environment. They showed that a plume in Europa's southern hemisphere generates a tube-like region of enhanced current density within the main southern Alfvén wing, called an *Alfvén winglet*. Like the main Alfvén wing, the winglet's current system will extend to arbitrarily large distances from Europa (due to the translational invariance of the Alfvén wing along its characteristics, see Neubauer, 1980) and may allow for a "remote" detection of plumes in magnetic field data from distant Europa flybys. Nevertheless, due to limitations of their model (e.g., the missing ionospheric Hall effect), Blöcker *et al.*, 2016 were not able to present conclusive evidence for a plume crossing in magnetic field data from Galileo's flybys of Europa.

Only two out of eleven Galileo flybys passed Europa at a low altitude of just 400 km during closest approach, the E12 and E26 flybys (Kivelson *et al.*, 2009). Magnetic field observations from both flybys show narrow, distinct perturbations in all three field components, as suggested by Blöcker *et al.*, 2016 due to a potential Alfvén winglet. By using the BATS-R-US multi-fluid model, Jia *et al.*, 2018 presented strong evidence for a plume near Europa's equator in magnetic field data from the E12 encounter on December 1997. These authors showed that the observed sharp drops and enhancements in all three magnetic field components are consistent with the spacecraft passing through a plume around closest approach. Additionally, they strengthened their hypothesis by matching the density enhancement observed by the Galileo Plasma Wave Spectrometer near closest approach (C/A). Arnold *et al.*, 2019 presented evidence for plume activity in Europa's southern trailing hemisphere during Galileo's E26 flyby on 3 January 2000 by using the hybrid code AIKEF (Adaptive Ion-Kinetic Electron-Fluid, (Müller *et al.*, 2011)). These authors showed that the fine structures in the draping signatures observed during E26 are not reproducible without taking into account a plume, whereas with the plume incorporated, numerous key features of the modeled magnetic field signatures are nearly indistinguishable from observations. Plumes at Europa therefore seem to have been a persistent phenomenon during the

Galileo era.

Until now, plumes at Europa have been identified in plasma and magnetic field data only for two specific magnetospheric field orientations and plume locations. However, a systematic understanding of how the plume's location affects the plasma flow and magnetic field is still missing. Also, it is yet unclear to which degree the plasma interaction with the global atmosphere and the induced field can obscure the local interaction signatures of a plume at different locations. Our study therefore aims to systematically assess the magnitude and structure of the perturbations associated with plume-plasma interactions at Europa for various plume locations at the moon's surface and for different representations of the moon's global atmosphere. We will consider symmetric and asymmetric density profiles of Europa's neutral gas envelope. To isolate the impact of a plume on Europa's magnetospheric environment, we will also model Europa's plasma interaction without any global atmosphere. We will determine the degree to which different plume configurations can be obscured by the plasma interaction with Europa's induced dipole field and its global atmosphere. We note, that due to their large closest approach altitudes, we do not expect to find new plume signatures in magnetic field data from flybys other than E12 and E26 (which have already been studied).

The structure of the paper is as follows: In section 4.3 a description of the simulation model and the model parameters are given. section 4.4 presents and discusses the results of our study. section 4.5 concludes the paper with a summary of our findings.

4.3 Model description

To model Europa's interaction with its magnetospheric environment, we use the AIKEF (Adaptive Ion-Kinetic Electron-Fluid) hybrid code (Müller *et al.*, 2011), which treats ions as particles and electrons as a massless, charge-neutralizing fluid. Therefore, our model can describe the flow shear between the magnetospheric plasma and ionospheric particles emanating from Europa, as well as the ionospheric Hall effect. The results of Blöcker *et*

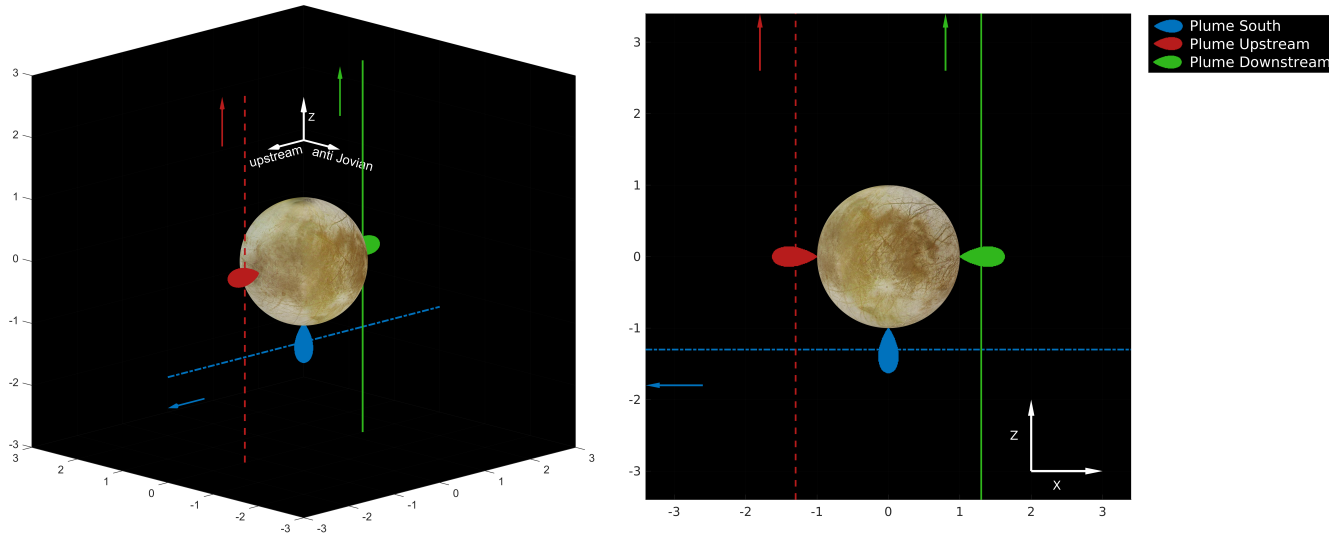

(a) (b)

Figure 4.1: Geometry of the three plume locations analyzed in this work as well as the synthetic trajectories used to study the magnetic signatures of these plumes (see subsection 4.4.5). In panel (a), the view point is located upstream, from the Jupiter-averted side, whereas in panel (b) we see Europa from the viewing angles $(\theta, \phi) = (180°, 90°)$. The dotted, red line represents a (hypothetical) flyby through a plume located upstream ($x = -1.3$ R_E, $y = 0$ and z varying), the blue line depicts a crossing of a south-polar plume (x varying, $y = 0$ and $z = -1.3$ R_E), and the green line corresponds to a flyby through a plume located at Europa's leading/downstream apex ($x = 1.3$ R_E, $y = 0$ and z varying), respectively.

al., 2016 and Jia *et al.*, 2018 indicate that any reasonable model of plume-plasma interactions at Europa should take into account the Hall effect within the plumes. The AIKEF code has already been successfully applied to study plume-plasma interactions at Europa during the Galileo E26 flyby (Arnold *et al.*, 2019). Previously, the code has been used to model Cassini magnetic field observations from multiple flybys through the Enceladus plume (Kriegel *et al.*, 2009, 2011, 2014) and also, to study the plasma interaction of Callisto, another Galilean moon of Jupiter (Liuzzo *et al.*, 2015, 2016; Liuzzo *et al.*, 2017; Liuzzo *et al.*, 2018). In addition, AIKEF has been successfully applied to, e.g. Titan (Feyerabend *et al.*, 2015, 2016) and Mercury (Müller *et al.*, 2012).

In our model we use the EPhiO coordinate system. It is a Cartesian coordinate system, where the x axis is aligned with the corotational flow direction, the y axis points toward Jupiter and the z axis completes the right-handed system. The origin of the EPhiO system is located at the center of Europa. The spherical coordinate system (r, θ, ϕ) associated with the EPhiO coordinate system is described by the radius r, the latitude θ measured from the positive z axis and ϕ denotes West Longitude measured clockwise from the positive y axis. The parameters for our simulations can be found in Table 4.1. Parameters are categorized in values for the upstream plasma, global atmosphere, and plume. For each of our simulations, the plume is either located at the apex of the trailing hemisphere (upstream "U", in spherical EphiO coordinates, $(r, \theta_F, \phi_F) = (R_E, 90°, 270°)$), the apex of the leading hemisphere (downstream "D", $(r, \theta_F, \phi_F) = (R_E, 90°, 90°)$), or at Europa's south pole ("S", $(r, \theta_F, \phi_F) = (R_E, 180°, 0°)$), as seen in Figure 4.1. At all three locations, the plume axis is oriented perpendicular to Europa's surface. By choosing these locations, we keep the geometry of the interaction scenario as simple as possible, while the locations of the plume foot points are still similar to observations by HST (similar to the south-polar foot point of Roth *et al.*, 2014a and the equatorial foot point of Sparks *et al.*, 2016). For each of these three plume locations, a series of four simulation runs has been carried out: Runs denoted by label ".1" do not consider any global atmosphere at all, i.e., the incident plasma interacts with the plume or directly with Europa's absorbing surface. The goal of these runs is to define a "baseline" for subsequent studies of the obstruction of a plume by an atmosphere (of varying complexity) and an induced dipole. For each plume configuration, runs denoted by ".2" and ".3" take into account a global symmetric or asymmetric atmosphere, respectively. Even though the asymmetric model for the atmosphere seems to be closer to reality (Cassidy *et al.*, 2013; Plainaki *et al.*, 2018; Rubin *et al.*, 2015), the simulations with a symmetric atmosphere facilitate a discrimination between asymmetries in the plasma interaction generated by the global atmosphere or by the location of the plume source. Runs labeled ".4" consider the plasma interaction with a plume source, Europa's

asymmetric global atmosphere and an induced dipolar field from the moon's subsurface ocean. This is the most realistic scenario and will be likely observed during flybys (e.g., (Arnold *et al.*, 2019; Jia *et al.*, 2018)).

To facilitate a comparison to previous results (e.g., to Blöcker *et al.*, 2016 and Arnold *et al.*, 2019), we apply a similar set of parameters for the upstream plasma. The value for the bulk velocity of the (partially) corotating plasma is $u_0 = 100$ km/s, which is in agreement with Bagenal *et al.*, 2015; Kivelson *et al.*, 2009. The upstream number density in our model, $n = 60 \cdot 10^6$ m^{-3}, is within the range measured during various Galileo flybys (Kivelson *et al.*, 2004; Kurth *et al.*, 2001). Although the incident plasma parameters depend on Europa's distance to the Jovian current sheet, the Alfvénic Mach number M_A remains always $\ll 1$, i.e. the key features of the interaction change only quantitatively, but not qualitatively (Kivelson *et al.*, 2009). The mass of the singly-charged upstream ions is set to $m_i = 18.5$ amu, and the ion and electron temperatures read $k_B T_i = k_B T_e = 100$ eV (Kivelson *et al.*, 2004). We set the magnetospheric background field to $\vec{B_0} = (0, 0, -450)$ nT for the simulation runs ".1"-".3", similar to Blöcker *et al.*, 2016. This orientation and strength of the field are consistent with measurements taken when Europa was located close the center of Jupiter's magnetospheric current sheet (Kivelson *et al.*, 1999). The scenario of runs ".4", where the external magnetospheric field is set to $\vec{B_0} = (0, -210, -450)$ nT, corresponds to Europa being located north of the magnetospheric current sheet, where the field also has a radial component. The corotation-aligned component of the background field along Europa's orbit is usually negligible (see, e.g., Kivelson *et al.*, 1999 and Arnold *et al.*, 2019). By treating the subsurface ocean as a highly conducting medium, the induced magnetic moment can be written as

$$\vec{M}_{ind} = -\frac{2\pi R_E^3}{\mu_0}(B_{x,0}\vec{x} + B_{y,0}\vec{y}), \tag{4.1}$$

where $B_{x,0}$, $B_{y,0}$ are the components of the background magnetic field vector $\vec{B_0} = B_{x,0}\vec{x} +$

$B_{y,0}\vec{y} + B_{z,0}\vec{z}$ and $\vec{x}$, $\vec{y}$, $\vec{z}$ denote the unit vectors of the EPhiO system (see Kivelson *et al.*, 1999; Liuzzo *et al.*, 2016; Zimmer *et al.*, 2000). Thus, the induced magnetic field is absent in runs ".1" to ".3", whereas the slight change in the orientation of $\vec{B}_0$ for run ".4" generates an induced magnetic moment that is aligned with the y axis. The parameters for all runs result in a plasma beta of $\beta \approx 0.01$, Alfvénic Mach number of $M_A \approx 0.3$ and a magnetosonic Mach number of $M_{MS} \approx 0.3$.

In our model, Europa's global atmosphere consists of molecular oxygen, which is in agreement with observations (Hall *et al.*, 1995; McGrath *et al.*, 2009). Pospieszalska and Johnson, 1989 as well as Cassidy *et al.*, 2013 have shown that the surface sputtering and therefore, the distribution of neutral gas is not uniform at Europa. The sputtering rate was found to decrease from the trailing towards the leading hemisphere. Similar to Rubin *et al.*, 2015, Jia *et al.*, 2018 and Arnold *et al.*, 2019, these asymmetries are taken into account by our model through the following density profile for the neutral gas:

$$\begin{aligned} n_L(h) &= n_0 \cdot \exp\left(-\tfrac{h}{h_0}\right), & 90^\circ < \alpha \leq 180^\circ \quad , \\ n_T(h,\alpha) &= n_L(h) \cdot (1 + A \cdot \cos(\alpha)), & \alpha \leq 90^\circ \quad , \end{aligned} \tag{4.2}$$

where n_T is the density profile in the trailing ($x < 0$) and n_L the profile in the leading hemisphere ($x > 0$). The symbol n_0 represents the density at the surface, h the radial distance $h = |\vec{r}| - R_E$ (where $\vec{r}$ is the position vector from Europa's center in EPhiO coordinates) to Europa's surface and h_0 the neutral scale height. The angle α is measured from the negative x axis and denotes the angle between the upstream direction ($-x$ axis) and the position vector $\vec{r}$. Therefore, α ranges from 0° to 180°. Thus, the model atmosphere exhibits rotational symmetry around the x axis, i.e., the isolines of the atmospheric neutral density are circles around the x axis. The asymmetry between leading and trailing hemisphere is controlled through the parameter A, where $A = 0$ results in a symmetric (runs ".2") and $A = 10$ (adopted from Arnold *et al.*, 2019) in an asymmetric density distribution (runs ".3" and ".4"). In agreement with the model of Arnold *et al.*, 2019 and HST observations (Hall

et al., 1995; Plainaki *et al.*, 2018; Saur *et al.*, 1998), we have chosen a neutral scale height of $h_0 = 100$ km and a surface density of $n_0 = 5 \cdot 10^{13}$ m^{-3}.

To model a water vapor plume at Europa's surface we use a neutral density profile similar to Jia *et al.*, 2018 and Arnold *et al.*, 2019:

$$n_P(h, \Delta\theta) = n_{P,0} \cdot \exp\left[-\left(\frac{h}{h_p}\right)^2 - \left(\frac{\Delta\theta}{h_\theta}\right)^2\right] \quad , \tag{4.3}$$

where $n_{P,0}$ is the plume's density at its foot point on Europa's surface, h_p the scale height and $2 \cdot h_\theta$ the opening angle of the plume. The parameter $\Delta\theta$ represents the angular distance from the center of the plume axis. The "origin" for the definition of $\Delta\theta$ is located at the foot point of the plume and *not* at the center of Europa. In contrast to Jia *et al.*, 2018 and Arnold *et al.*, 2019 the plume axis is perpendicular to Europa's surface at all three plume locations. Since we aim to understand the general physics of plume-plasma interactions at Europa instead of analyzing a specific flyby dataset, this approach facilitates straightforward access to the involved mechanisms. Again, to facilitate a comparison to Jia *et al.*, 2018 and Arnold *et al.*, 2019, we have chosen similar parameters, $h_p = 200$ km, $h_\theta = 15°$ and $n_{p,0} = 3.9 \cdot 10^{15}$ m^{-3}, resulting in column densities of the plume similar to those observed by HST (Roth *et al.*, 2014a; Sparks *et al.*, 2016).

Europa's neutral gas envelope is partially ionized by electron impact ionization, which is an order of magnitude stronger than photoionization (Saur *et al.*, 1998). In analogy to Schilling *et al.*, 2008, Blöcker *et al.*, 2016, Jia *et al.*, 2018 and Arnold *et al.*, 2019, we obtain the ion production rate by multiplying the electron impact ionization rate $f_{imp}(T_e)$ for H_2O and O_2 with the respective neutral density profile. The loss process included for the ionized molecules is dissociative recombination, which is several orders of magnitude weaker than ionization (Arnold *et al.*, 2019; Jia *et al.*, 2018). The generated ions are H_2O^+ from the plume and O_2^+ from the global atmosphere, respectively. We note that the mass-to-charge ratio of H_2O^+ is representative for the entire range of water group ion species.

These ions are referred to as "plume" ions in the following. For a detailed description of the ionization model and the applied values of ionization/loss rates, we refer the reader to section 2 of Arnold *et al.*, 2019.

The extension of the simulation domain is $-10\ R_E \leq x \leq 20\ R_E$, $-15\ R_E \leq y \leq 15\ R_E$, and $-30\ R_E \leq z \leq -30\ R_E$. The simulation grid contains two refinement levels centered around (0,0,0): the grid resolution is 33 km for $|x, y, z| \leq 1.5\ R_E$, 66 km for $1.5\ R_E < |x, y, z| \leq 3\ R_E$ and 132 km at larger distances. The simulations reach stationarity after a passage of the plasma flow through the simulation domain.

To quantify the magnetic field perturbations caused by plumes at different surface locations, we analyze all three magnetic field components B_x, B_y and B_z, along a hypothetical spacecraft trajectory through each plume (seeFigure 4.1). Similar to the Galileo E12 and E26 flybys, we have chosen a closest approach altitude of 0.3 R_E and keep the flyby geometries simple, by varying only one coordinate along each trajectory (x for the south-polar plume and z for the plumes located at the upstream and downstream apices). To assess the plume's imprint on the magnetic field along a given spacecraft trajectory, we conducted an additional series of runs "JA" (just atmosphere), with just a symmetric atmosphere ($A = 0$, *without a plume*), see subsection 4.4.5.

Table 4.1: The plasma, atmosphere and plume parameters of the simulation runs. The symbols in the first column denote the "ingredients" of each model scenario: "U" (upstream, referring to a plume located at $(r, \theta_F, \phi_F) = (R_E, 90°, 270°)$), "S" (south pole, a plume located at $(r, \theta_F, \phi_F) = (R_E, 180°, 0°)$) and "D" (downstream, a plume at $(r, \theta_F, \phi_F) = (R_E, 90°, 90°)$). For each model setup, runs ending with ".1" denote the case without any global atmosphere at all, where as ".2" and ".3" stand for the case with a symmetric and asymmetric global atmosphere, respectively. Runs ending with ".4" consider the plasma interaction with a local plume source, Europa's asymmetric global atmosphere and a induced dipolar field from the moon's subsurface ocean. All other symbols from the table are defined in the text. The final run (labeled JA) considers only a symmetric global atmosphere, but no plume source at all.

	Upstream Plasma				Global Atmosphere			Plume					
Scenario	$\vec{B_0}$ [nT]	u_0 [km/s]	n [m^{-3}]	$kT_i = kT_e$ [eV]	n_0 [m^{-3}]	h_0 [km]	A	$n_{p,0}$ [m^{-3}]	h_p [km]	$\Delta\theta$ [°]	θ_F [°]	ϕ_F [°]	kT_{H_2O} [eV]
#U.1	(0,0,-450)	100	$60 \cdot 10^6$	100	-	-	-	$3.9 \cdot 10^{15}$	200	15	90	270	0.1
#U.2	(0,0,-450)	100	$60 \cdot 10^6$	100	$5 \cdot 10^{13}$	100	0	$3.9 \cdot 10^{15}$	200	15	90	270	0.1
#U.3	(0,0,-450)	100	$60 \cdot 10^6$	100	$5 \cdot 10^{13}$	100	10	$3.9 \cdot 10^{15}$	200	15	90	270	0.1
#U.4	(0,-210,-450)	100	$60 \cdot 10^6$	100	$5 \cdot 10^{13}$	100	10	$3.9 \cdot 10^{15}$	200	15	90	270	0.1
#S.1	(0,0,-450)	100	$60 \cdot 10^6$	100	-	-	-	$3.9 \cdot 10^{15}$	200	15	180	0	0.1
#S.2	(0,0,-450)	100	$60 \cdot 10^6$	100	$5 \cdot 10^{13}$	100	0	$3.9 \cdot 10^{15}$	200	15	180	0	0.1
#S.3	(0,0,-450)	100	$60 \cdot 10^6$	100	$5 \cdot 10^{13}$	100	10	$3.9 \cdot 10^{15}$	200	15	180	0	0.1
#S.4	(0,-210,-450)	100	$60 \cdot 10^6$	100	$5 \cdot 10^{13}$	100	10	$3.9 \cdot 10^{15}$	200	15	180	0	0.1
#D.1	(0,0,-450)	100	$60 \cdot 10^6$	100	-	-	-	$3.9 \cdot 10^{15}$	200	15	90	90	0.1
#D.2	(0,0,-450)	100	$60 \cdot 10^6$	100	$5 \cdot 10^{13}$	100	0	$3.9 \cdot 10^{15}$	200	15	90	90	0.1
#D.3	(0,0,-450)	100	$60 \cdot 10^6$	100	$5 \cdot 10^{13}$	100	10	$3.9 \cdot 10^{15}$	200	15	90	90	0.1
#D.4	(0,-210,-450)	100	$60 \cdot 10^6$	100	$5 \cdot 10^{13}$	100	10	$3.9 \cdot 10^{15}$	200	15	90	90	0.1
#JA	(0,0,-450)	100	$60 \cdot 10^6$	100	$5 \cdot 10^{13}$	100	0	-	-	-	-	-	-

4.4 Results

4.4.1 Case 1: Plasma interaction with a plume and Europa's solid body

In Figure 4.2(a)-(c) the B_x component of the magnetic field for runs ".1" (without a global atmosphere) is shown. Figure 4.2(a) corresponds to the scenario where the plume is located at Europa's south pole ("S"). In this scenario mass loading through ionization of plume neutrals results in an Alfvén wing in Europa's southern hemisphere. Due to hemisphere coupling between Europa's southern and northern hemisphere (Saur *et al.*, 2007), there is a weak ($B_x \approx 2\% B_0$, where B_0 is the magnetospheric background field) draping signature visible in Europa's northern hemisphere and in its intermediate wake (within $2.5 R_E$). A similar effect was observed at Enceladus by the Cassini spacecraft (Simon *et al.*, 2011, 2014). In Figure 4.2(b) (plume located at "D") and Figure 4.2(c) (plume located at "U") a narrow Alfvén wing forms at the plume's location, resulting in a wing downstream in Figure 4.2(b) and upstream in Figure 4.2(c), respectively. However, the solid body of the moon itself does not impose any discernible draping on the magnetic field lines. As can be seen from panels Figure 4.2(b) and Figure 4.2(c), the B_x perturbations "above" and "below" Europa are partially zero. In principle, a plasma-absorbing moon (without any atmosphere) still generates a weak Alfvén wing, as shown by Simon *et al.*, 2012 for Rhea. However, the intensity of the associated B_x perturbations is proportional to $1/B_0$, . Due to the strong background field at Europa (more than a factor of 20 stronger than at Rhea), this effect does not make any discernible contribution to the field perturbations in Figure 4.2(b) and Figure 4.2(c). Ionized particles from a plume located at the upstream apex are transported toward Europa because of the $\vec{E} \times \vec{B}$ drift, i.e., the flow of picked-up ions "overlaps" with the ion population within the plume. This effect results in a higher ion density in the plume for case "U", compared to case "D". This is also visible in the strength of the B_x perturbations (≈ 20 nT stronger in case "U" than in case "D").

Panels Figure 4.2(d)-(f) show the B_z component of the magnetic field. In the case of

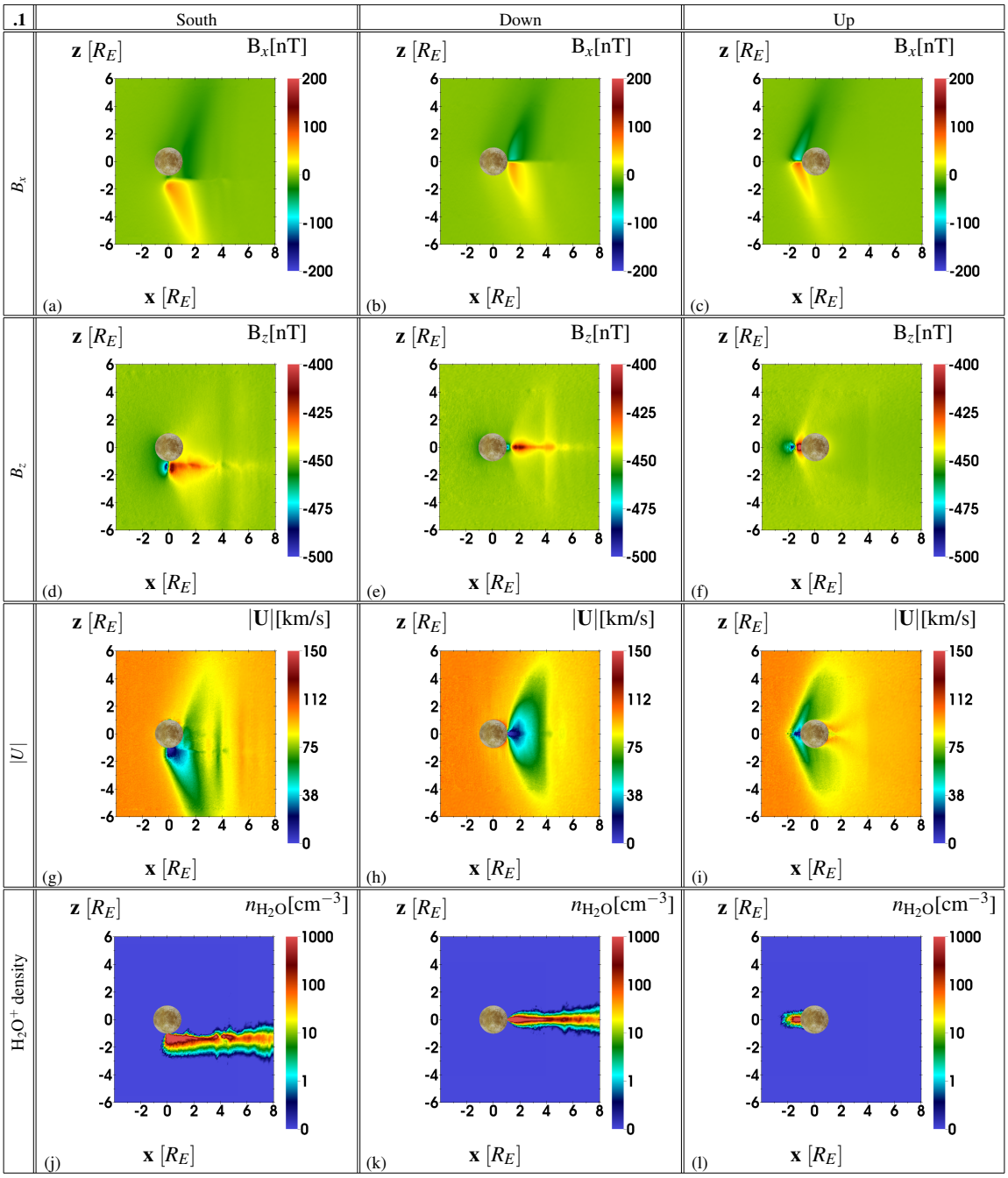

Figure 4.2: Two-dimensional cuts through the AIKEF simulation domain in the $y = 0$ plane, showing the B_x and B_z components (first and second row), as well as the bulk velocity of the plasma (third row) and the plume ion density (fourth row) for runs of configuration ".1" (without any global atmosphere). For the runs in the first column, the plume is located at Europa's south pole ("S"), whereas in the second and third columns the plume is located at the downstream ("D") and upstream ("U") apices, respectively (see section 4.3 for details).

a south-polar plume, a localized pile-up of 25 nT in front of the plume can be observed. In contrast to this, the field lines pass through Europa's solid body unimpeded, i.e., no discernible pile-up is formed in front of the moon itself. In Figure 4.2(e) the pile-up structure of the plume forms at Europa's wakeside, where the magnetospheric field lines re-enter the plasma after diffusing through the moon's solid body and encounter the narrow tail of slow plume plasma (with same magnitude as in case "S"). In Figure 4.2(f) the plume obstacle is encountered by the incident plasma before it even reaches Europa's surface, resulting in a localized, narrow pile-up structure (of $0.5 - 1\ R_E$ width) in front of the moon. In all three cases, the extension of the pile-up is determined by the size of the plume and *not* by the diameter of Europa.

The bulk velocity $|\vec{U}|$ in panels Figure 4.2(g)-(i) reveals the locations of the plumes, through slowing of the upstream plasma due to mass loading by the plume particles. These panels also show that the region where the plasma flow is decelerated by mass loading to $|\vec{U}| \leq 0.1U_0$ is much larger than the region where $|B_z|$ differs significantly from the background value of 450 nT. For a plume located at Europa's south pole or at the wakeside, the extension of this region is comparable to that of Europa. This results in an asymmetry between the plasma flow in the northern and southern hemispheres in the case of a south-polar plume, as shown in panel Figure 4.2(g). Thus, the electric field and the associated velocity of the pick-up ions are smaller in the southern than in the northern hemisphere. In the case of a plume located at the downstream or upstream apex, the perturbations in the velocity (and all other quantities) are symmetric between both hemispheres, as shown, e.g., in panels Figure 4.2(h) and Figure 4.2(i). This is the result of the plume axis being located in the $z = 0$ plane and the symmetric Alfvén wave propagation perpendicular to that plane (due to the chosen orientation of $\vec{B}_0$).

The plume ion density is depicted in panels Figure 4.2(j)-(l). For a plume located at the upstream apex (Figure 4.2(l)), plume ions are confined to a pillar-like region (≈ 1.5 R_E in length and width) upstream of Europa. There is no pick-up tail in Europa's wake-

side hemisphere, since plasma produced through ionization of water vapor immediately re-encounters Europa's surface and is unable to flow around the moon. The reason is the small extent (opening angle: $h_\theta = 15°$) of the plume, compared to the size of the moon, which is a major difference to the Enceladus plume. The width of the pick-up tail (in z direction) in panel Figure 4.2(j) is determined by the scale height of the plume (since the plume axis is perpendicular to the upstream flow), whereas in panel Figure 4.2(k) the plume axis is aligned with the upstream flow, and therefore, the width of the tail is determined by the opening angle of the plume.

4.4.2 Case 2: Plasma interaction with a plume and a symmetric global atmosphere at Europa

In Figure 4.3(a)-(c) the B_x component of the magnetic field for runs ".2" (with a global, symmetric atmosphere) is shown. In these runs, the overall plasma interaction is mainly driven by the mass loading from the global atmosphere, rather than the mass loading from the local plume source. This results in a modeled draping signature of $|B_x| \approx 150$ nT, which is an order of magnitude stronger than the draping in series ".1" (see Figure 4.2), where the global atmosphere was not yet considered. The diameter of the Alfvén wings, mainly driven by the atmosphere, is now comparable to the size of the Europa obstacle (panels Figure 4.3(a)-(c)). The magnitude of magnetic pile-up (visible in the B_z component, see panels Figure 4.3(d)-(f)) upstream of the obstacle is of the same order as the pile-up due to a plume alone (see panels Figure 4.2(d)-(f)), but much more extended. Thus, the plume signature in B_z is almost completely "buried" within this extended pile-up region. Nonetheless, the plumes in all three scenarios are still visible in the fine structures of the magnetic field. In panel Figure 4.3(a) we see a localized (within 0.5 R_E from the surface) enhancement of the draping below Europa's south pole (depicted in dark red), compared to the rather uniform B_x perturbations above the moon's north pole. Additionally, panels Figure 4.3(d) and Figure 4.3(f) reveal a highly localized pile-up in front of the plume's lo-

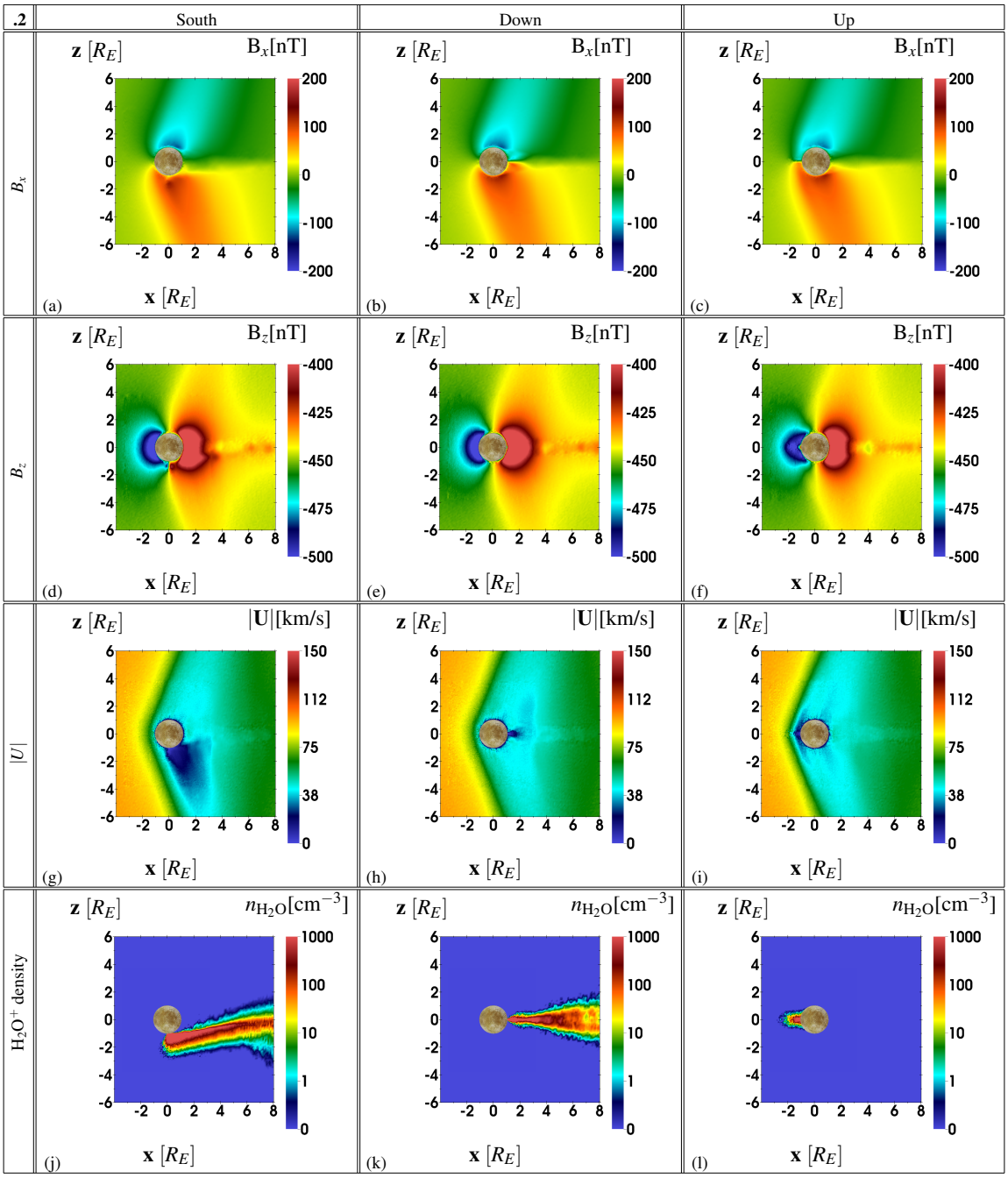

Figure 4.3: Two-dimensional cuts through the AIKEF simulation domain in the $y = 0$ plane for runs of configuration ".2". The quantities shown in the panels are the same as in Figure 4.2.

cation (within 0.5 R_E, depicted in dark blue), whereas panel Figure 4.3(e) shows no plume signature at all and the plume completely "disappears" in the magnetic depletion region downstream of Europa (dark red). Hence, the inclusion of a global atmosphere obscures

large portions of the magnetic signatures generated by a plume source alone.

The plasma quantity that is again most indicative of a plume is the bulk velocity $|\vec{U}|$ (Figure 4.3(g)-(i)). When a global atmosphere is included, the deceleration of the flow due to the mass loading is much more pronounced than in Figure 4.2: the plasma flow within the Alfvén wing tubes is slowed down to below 40 km/s. In case ".1" such a strong deceleration occurs only in the immediate vicinity of the plume. In case ".2", the region of decelerated flow extends to Europa's wakeside (up to several R_E in the x-direction). Again, this region is symmetric between the moon's northern and southern hemispheres for a plume located at "U" and "D". For a plume located at the south pole, the region of nearly stagnating flow still possesses a pronounced north-south asymmetry (see panel Figure 4.3(g)) that should be detectable by a spacecraft, despite the superimposed reduction in flow speed caused by Europa's global atmosphere.

The plume ion density is depicted in Figure 4.3(j)-(l). In the case of a plume at Europa's south pole (Figure 4.3(j)), the pick-up tail is slightly inclined northward due to the $\vec{E} \times \vec{B}$ drift perpendicular to the draped magnetic field lines. At larger distances along the corotation direction, where the field lines straighten again, the tail becomes more aligned with the x axis. This tilt of the pick-up tail is not visible in runs of series ".1" (without a global atmosphere) because the mass loading and therefore, the draping of the magnetic field lines is significantly weaker. In the case of a plume at Europa's downstream apex, the pick-up tail is again symmetric between the northern and southern hemispheres (Figure 4.3(k)). We note that this symmetry is also partially caused by the chosen orientation of the background field (in negative z direction) and would disappear, if Europa were placed outside of the Jovian magnetospheric current sheet (see case ".4", visible in panel Figure 4.3(k)). For a plume located at Europa's downstream apex, the pick-up ions tend to "refill" the region of reduced magnetic field in Europa's geometric plasma shadow, which results in a broadening of the pick-up tail. For a plume located upstream, again, no pick-up tail is visible at Europa's wakeside, because newly generated ions immediately "rain" down onto the moon.

The mass of plume ions is much lower than the mass of exospheric O_2^+ pick-up ions. Therefore, the ray-like density enhancement associated with the plume should be clearly discernible in spacecraft data. Also, plume ions (H_2O^+) would generate pick-up waves at a significantly higher frequency than exospheric O_2^+ (≈ 2 times higher, due to the mass difference between the species), thus being visible in magnetic field data (Desai *et al.*, 2017; Volwerk *et al.*, 2001).

4.4.3 Case 3: Plasma interaction with a plume and an asymmetric global atmosphere at Europa

In Figure 4.4(a)-(f) the magnetic field components for the plasma interaction with a plume and an asymmetric global atmosphere are shown. The most prominent effect of a ram-wake asymmetry in the global atmosphere is visible in the B_x component (Figure 4.4(a)-(c)). Whereas the B_x signature in case ".2" is nearly homogeneous across Europa's north and south-polar caps (in cases "U" and "D"), in scenario ".3", $|B_x|$ is stronger by ≈ 50 nT at Europa's ram side. This enhancement is generated by the increased mass loading due to a thicker neutral atmosphere around Europa's ram side apex (due to the asymmetry factor $A = 10$ in Equation 4.2). Similar to case ".2", the plume causes additional perturbations of only a few nT in its immediate vicinity, whereas the Alfvén winglet at larger distances is barely visible within the "main" wing generated by the global atmosphere. In B_z (panels Figure 4.4(d)-(f)), subtle changes due to inclusion of global asymmetries in the atmosphere now "compete" with the signatures of a local plume source. For the run with a south-polar plume, the plume location coincides with the transition from the angle-dependent to the radially symmetric neutral gas profile (see Equation 4.2). Therefore, while the plume still generates a distinct "kink" in the B_z component below Europa's south pole, the separate pile-up feature in front of the plume has vanished (see panel Figure 4.4(d)). For the case of a plume located at Europa's ram side, the associated pile-up is completely obscured by the magnetic signatures of the enhanced neutral density of the global atmosphere (see

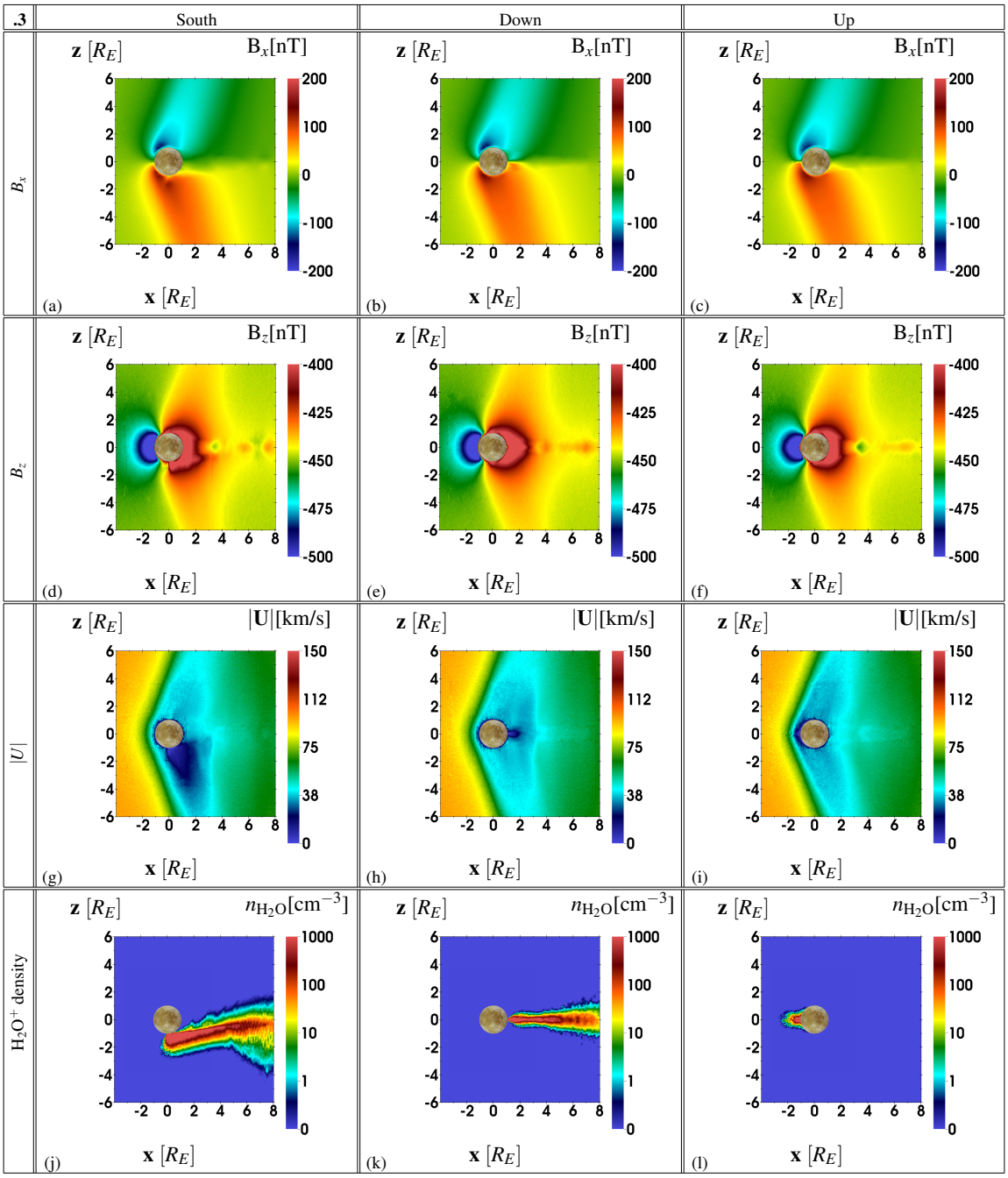

Figure 4.4: Two-dimensional cuts through the AIKEF simulation domain in the $y = 0$ plane for runs of configuration ".3". The quantities shown in the panels are the same as in Figure 4.2 and Figure 4.3.

panel Figure 4.4(f). For the plume located at Europa's wakeside apex, the plume signature remains buried within the mass loading signatures of Europa's global atmosphere, similar to case ".2".

The localized drop in the plasma's bulk velocity (Figure 4.4(g)-(i)) is again most indicative for the presence of a plume. However, compared to case ".2", shape and strength of the flow deceleration are nearly unaffected by inclusion of global asymmetries in the atmosphere. The enhanced neutral densities in case ".3" are confined to Europa's ramside hemisphere. Hence, many newly generated ions from the "surplus" of neutral gas immediately re-encounter the moon and are absorbed, rather than contributing to mass loading and pick-up (similar to the plume ions in the "U" scenarios). Therefore, the effect of the enhanced atmospheric ramside density on the flow is rather subtle. The shape of the plume's pick-up tail (Figure 4.4(j)-(l)) is nearly unaffected by the asymmetry in Europa's global atmosphere. Only the width of the plume's pick-up tail is slightly broader in case ".2" than in case ".3" (see Figure 4.3 and Figure 4.4). These subtle differences are caused by the slightly stronger deflection of the upstream plasma in the case of an asymmetric atmosphere, which also affects the fields and flow pattern downstream of Europa.

4.4.4 Case 4: Plasma interaction with a plume, induced dipole and an asymmetric global atmosphere at Europa

Figure 4.5(a)-(c) show the B_x component for case ".4", the plasma interaction with a plume, induced dipole and an asymmetric global atmosphere. Due to $B_{y,0}$ being non-zero, the Alfvén wing characteristics are no longer parallel to any plane of the EPhiO system. Therefore, for a better understanding of the involved physics we display the plasma interaction signatures in a rotated system (x, $\tilde{y}$, $\tilde{z}$) such that the (x, $\tilde{z}$) plane contains the wing characteristics. The rotation angle α around the x axis is $\alpha = \arctan(B_{y,0}/B_{z,0}) = 25°$. The magnetic field orientation in case ".4" results in a highly complex geometry for the case of a south- polar plume, where the plume axis is no longer contained within any of the coordinate planes. Therefore, we subsequently study the magnetic field along hypothetical trajectories to better understand the local influence of the plume.

The diameter of the Alfvén wings is visibly shrunk compared to cases ".2" and ".3"

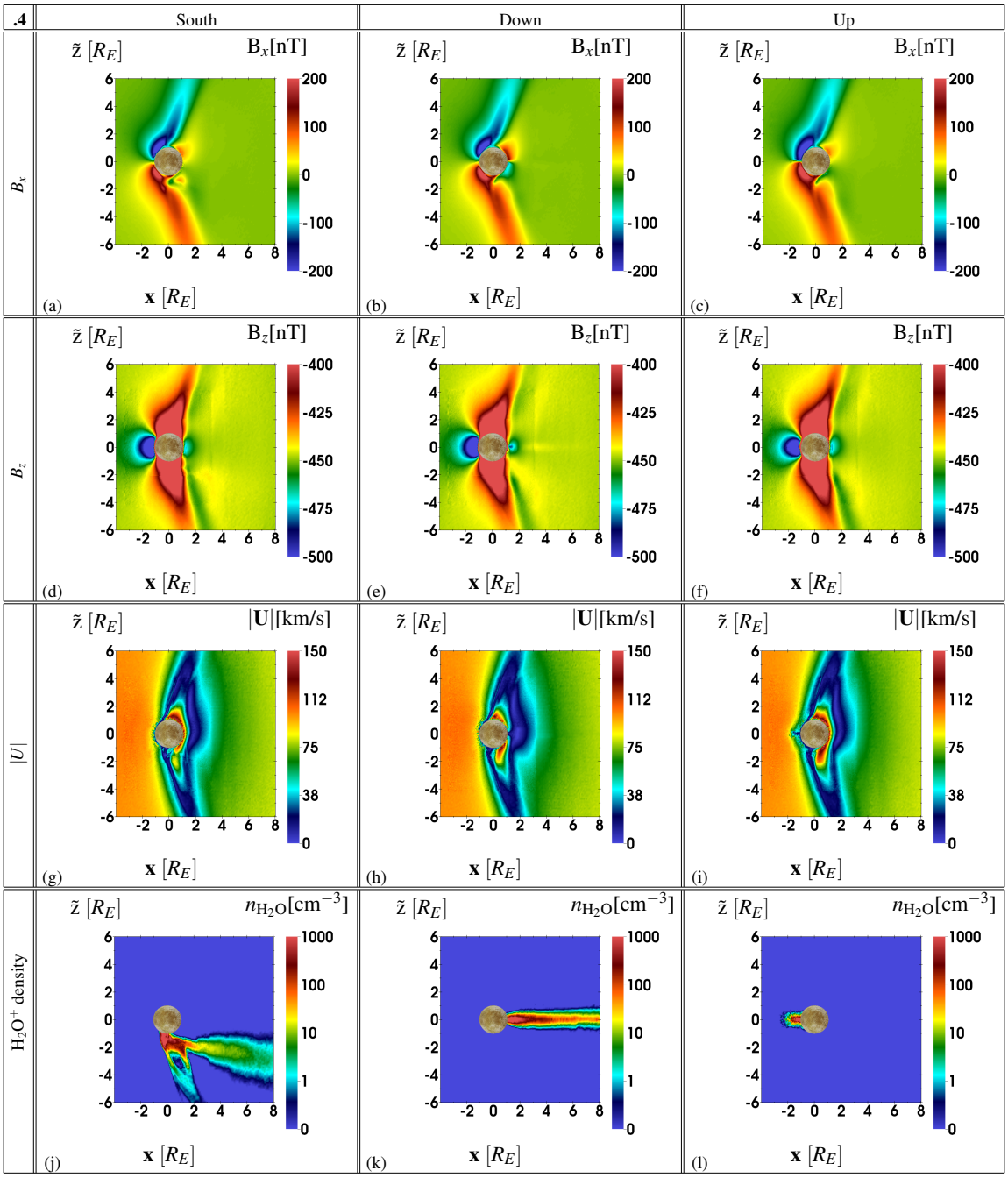

Figure 4.5: Two-dimensional cuts through the AIKEF simulation domain for case ".4", where $\tilde{z}$ is rotated around the x axis by the angle $\alpha_{\tilde{z}} = \arctan(B_{y,0}/B_{z,0}) \approx 25°$, therefore showing the interaction region in the plane which contains the Alfvén characteristics $\vec{v}_{a0} \pm \vec{u}_0$ and the upstream flow velocity $\vec{u}_0$. The quantities shown in the panels are the same as in Figure 4.2-Figure 4.4.

(less than 2 R_E compared to 3 R_E), due to the local twist of $\vec{B}$ caused in the immediate vicinity of Europa by the induced dipole. This shrinkage has been theoretically predicted

by Neubauer, 1999 and it was observed at Europa by Galileo, e.g., during the E26 flyby (Volwerk *et al.*, 2007). Without any plasma effects the induced dipole field would generate a shamrock-like structure in the B_x component (see Liuzzo *et al.*, 2016 for a detailed discussion). In Figure 4.5(b)-(c) these "shamrock leaves" are still discernible at Europa's wakeside ($B_x > 0$ for $\tilde{z} > 0$ and $B_x < 0$ for $\tilde{z} < 0$), albeit being compressed by the Alfvén wings. In the case of a south- polar plume (panel Figure 4.5(a)), asymmetric draping near the plume's location is visible. For a plume at Europa's wakeside, the signature of the two B_x "leaves" in Europa's downstream hemisphere is amplified (see panel Figure 4.5(b)). The "leaf"-like structure in Europa's wake gets compressed by the Alfvén wings from the "outside" and by the plume located in between the two regions of opposite B_x polarity. A plume located at Europa's ramside apex counteracts the compression of the dipole and leads to a small extension of the field line draping ($< 1\ R_E$). Overall, due to the more compact structure of the Alfvén wings, the Alfvén winglet in B_x (visible in cases ".1"-".3", see Figure 4.2–Figure 4.4) is not discernible over the "main" wing any more. This finding is also true for cutting planes other than the (x, $\tilde{y}$, $\tilde{z}$) plane shown in Figure 4.5. The B_z component (panels Figure 4.5(d)–(f)) shows only minor quantitative differences between the three plume locations. The pile-up structure in front of the plume is now completely buried within the signatures generated by the plasma interaction with the atmosphere and induced dipole. In other words, considering the induced dipole eliminates most of the signatures associated with a plume in scenarios ".1"-".3". Therefore, a flyby that is most "suitable" for the identification of plumes in magnetic field data should take place with Europa located close to the center of the Jovian current sheet (our cases 2-3), where the induced dipole is weak or even vanishes (Zimmer *et al.*, 2000).

The bulk velocity $|\vec{U}|$ (Figure 4.5(g)-(i)) no longer shows a distinct region (with a similar size as Europa) of reduced momentum due to mass loading by the plume plasma (in contrast to cases ".1"-".3"). The induced dipole increases the strength of the obstacle to the plasma flow and reduces the plasma bulk velocity to below 20 km/s within the entire

Alfvén wing (compared to ≈ 40 km/s in the cases without a dipole). Due to the tilt of the plume axis in scenario "S" (out of the $x - \tilde{z}$ plane), the plasma is already re-accelerated at the flanks of the plume (resulting in the yellow region directly below the south pole in panel Figure 4.5(g)). For a plume located at Europa's ramside apex, upstream flow stagnation associated with the plume is visible in a ray-like region (see panel Figure 4.5(i)). Overall, the plume signature with a dipole included is barely noticeable in the bulk velocity (on length scales of $\leq 1\ R_E$).

In panel Figure 4.5(j), where the south-polar plume axis is inclined against both, the background magnetic field and the induced dipole, our model reveals a complex, three-dimensional outflow pattern with several ray-like regions of enhanced ion density. Such a filamentation of the pick-up tail has been observed by Cassini at Titan (Coates *et al.*, 2012) and also occurs in hybrid simulations of the Titan interaction (Feyerabend *et al.*, 2015). For plumes located at Europa's ramside (see Figure 4.5(l)) or wakeside (see Figure 4.5(k)), the geometry of the pick-up ion tail does not change compared to cases ".1-.3".

In our hybrid model results, the obscuring effect of the induced dipole seems to be more "drastic" than in the MHD model of Blöcker *et al.*, 2016, see section 3.3 in that work. Using the same upstream magnetic field as our model, these authors found that inclusion of the dipole mainly causes quantitative changes in the flow deflection pattern, but the local enhancements generated by the plume are still clearly discernible.

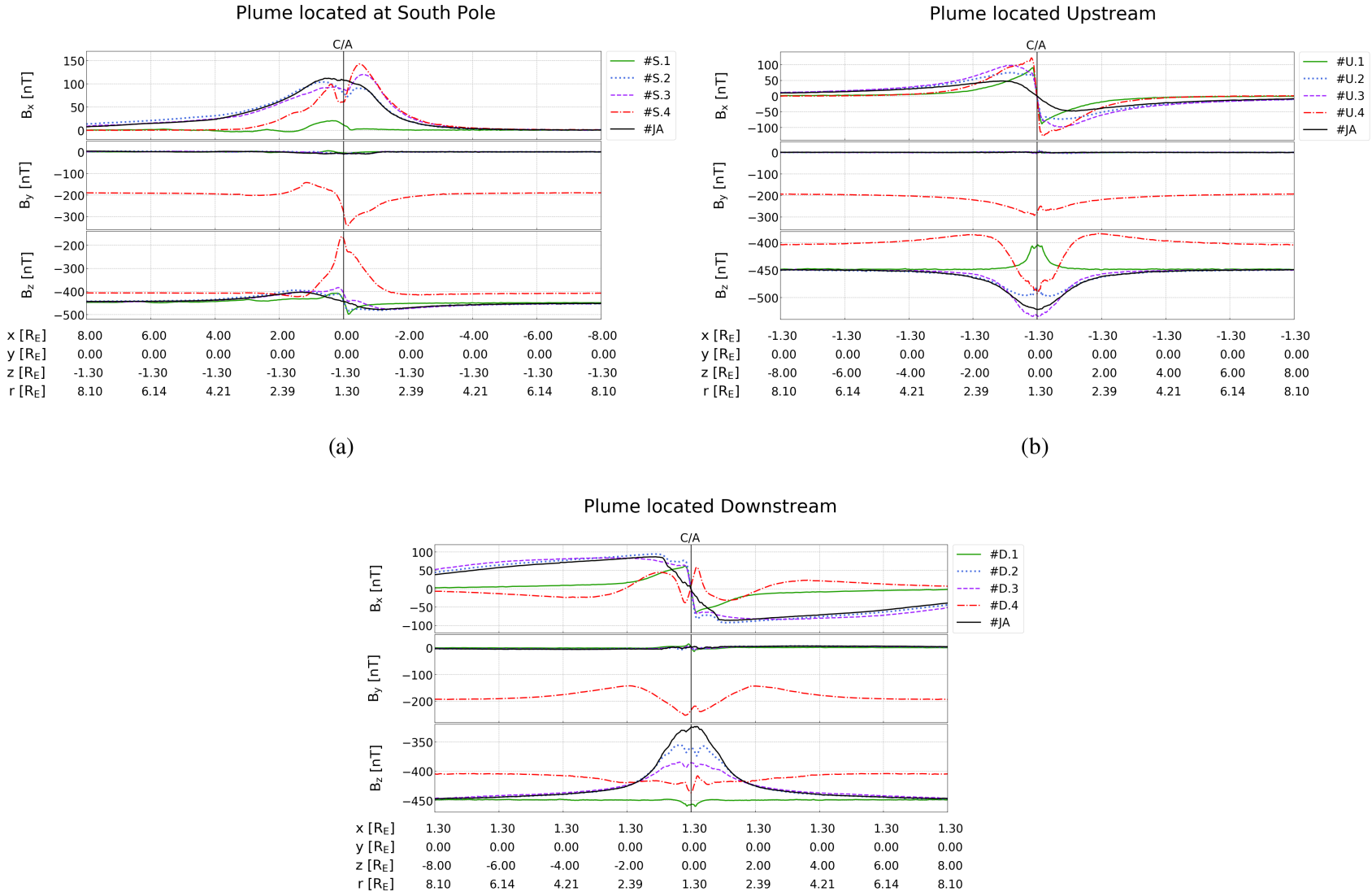

Figure 4.6: Modeled magnetic field along hypothetical flyby trajectories, as displayed in Figure 4.1. Each panel displays the field perturbations for a scenario without a plume "JA" and scenarios with a specific plume location: (a) a plume located at Europa's south pole, (b) a plume located at Europa's upstream apex and (c) a plume located at Europa's downstream apex. Figure 4.1 shows the geometries for each of the three hypothetical flybys considered here. In that figure, the geometry of panel (a) is represented by the blue line, panel (b) by the red line, and panel (c) by the green line. Each hypothetical trajectory has a closest approach altitude of 0.3 R_E, similar to the Galileo E12 and E26 flybys where magnetic signatures of plumes were actually observed at Europa.

4.4.5 Magnetic field analysis along hypothetical spacecraft trajectories

Figure 4.6(a)-(c) show all three magnetic field components B_x, B_y and B_z along hypothetical trajectories through the plumes for scenarios ".1"-".4" and a scenario without a plume "JA", considering only the plasma interaction with a symmetric ($A = 0$) global atmosphere. This setup is similar to the one used by Blöcker *et al.*, 2016, thereby facilitating a direct comparison of the results from both studies. The hypothetical flyby trajectories discussed in this section are displayed in Figure 4.1. Modeled magnetic field data for a plume located at the south pole (see Figure 4.6(a)) are obtained along a trajectory where x changes, $y = 0$ and $z = -1.3\ R_E$. For the plume located at Europa's upstream apex, modeled magnetic field data (see Figure 4.6(b)) is shown along a trajectory where z varies, $x = -1.3\ R_E$ and $y = 0$. Finally, modeled magnetic field data for a passage through a downstream plume (see Figure 4.6(c)) is shown along a trajectory where z changes, $x = 1.3\ R_E$ and $y = 0$. At higher altitudes, the magnetic signatures of the plumes quickly faint and become indiscernible from the signatures of the atmospheric interaction. This may be one of the reasons why Galileo detected signatures of plumes only during E12 and E26.

In panel Figure 4.6(a) we display the magnetic signatures generated by a plume located at Europa's south pole. The perturbations in B_x near closest approach are weakest for case "S.1" (no global atmosphere, just a plume), whereas in the other four cases the draping in B_x is of similar magnitude. The draping signature in B_x, for cases "S.2"-"S.4" and "JA", is associated with the crossing of the southern Alfvén wing. Without a plume (case "JA", black line), a single, broad enhancement is visible in B_x, whereas the inclusion of a plume generates an "M-like" drop in the strength of the draping near closest approach, similar to observations from the E26 Galileo flyby (see Arnold *et al.*, 2019). The shape of this feature is qualitatively similar in cases ".2"-".4", while the magnitude of the perturbation depends on the chosen atmosphere model and whether the dipole is included. The magnitude of the B_x perturbations is slightly strongest for the case with a dipole included (dashed red line in Figure 4.6, also shown in Figure 4.5(a)). In agreement with Arnold *et al.*, 2019, there are

no clear signatures of a plume in B_y. In the case with a dipole ".4", the y-component of the magnetic background field differs from the other runs ($B_{y,0} = -210$ nT instead of $B_{y,0} = 0$ nT). This finding is indeed independent of the location of the plume, see Figure 4.6(a)–(c). The perturbation signature in B_z is most prominent when a dipole is included (case "S.4", the red dash-dotted line). The dipole pushes the pile-up region so far toward upstream that in this case (and only in this case) the spacecraft passes through the magnetic depletion region downstream of the enhanced field. The signature of the induced dipole in B_z is much broader and more prominent than any signature associated with the plume, see also Figure 2(c) of Arnold *et al.*, 2019.

For the flyby upstream of Europa, shown in panel Figure 4.6(b), the trajectory intersects both Alfvén wings. The perturbation in B_x therefore is positive in Europa's southern hemisphere ($z < 0$) and negative in Europa's northern hemisphere ($z > 0$). In the case without a plume ("JA", black line), a smooth transition between both Alfvén wings can be seen, whereas the inclusion of a plume amplifies the B_x perturbations near closest approach and generates a sharp, discontinuity-like transition from the southern to the northern wing. Due to the C/A altitude of $\approx$ 460 km, the flyby occurs upstream of Europa's atmosphere (scale height 100 km) i.e., the trajectory intersects the compact Alfvén winglet generated by the plume and not the "main" Alfvén wing, which leads to the sharp transition seen in the B_x component. Looking at B_z, for cases with a symmetric atmosphere ("U.2") and a plume only ("U.1"), the plume source pushes the pile-up region away from Europa's surface, i.e., the pile-up is above the closest approach altitude and the field along the trajectory is slightly reduced. In scenario "U.3", the surface density of the neutral atmosphere is one order of magnitude larger at Europa's ramside than at the wakeside and comparable to the surface density of the plume source ($\alpha = 0°$: global atmosphere with 5 $\cdot 10^{12}$ m^{-3} and plume with 1.6 $\cdot 10^{13}$ m^{-3}). Therefore, the plume is not visible in the pile-up structure around C/A of "U.3" (violet dashed line) anymore. The strongest pile-up is visible in the case of a plume combined with an asymmetric atmosphere and the dipole included (case "U.4", red dashed

dotted line in Figure 4.6(b)), where the dipole again dominates the signature and the plume only causes a very weak kink outbound of C/A.

In Figure 4.6(c), the magnetic field perturbations for a plume located at Europa's wakeside apex are shown. Similar to the scenarios of Figure 4.6(b) (a plume located upstream), the plume generates characteristic fine structures in B_x near closest approach that are not present without a plume (run "JA", black line). Again, in cases ".1"-".3" (with a plume, without a dipole) a sharp transition between the northern and southern wing is visible around C/A due to the passage through the Alfvén winglet caused by the plume. In the scenario with a dipole included ("D.4", red dash-dotted line in Figure 4.6(c)), the Alfvén wings envelop the quasi-dipolar "shamrock leaf" structure in Europa's wake: in the southern hemisphere ($z < 0$), the perturbation of B_x is positive for the southern Alfvén wing, whereas the adjacent dipolar contribution is negative (and the other way around for Europa's northern hemisphere). This scenario is similar to observations of Callisto's wake during the Galileo C10 flyby (see Liuzzo *et al.*, 2016).

In the scenario without a global atmosphere, case "D.1" (green line), a weak enhancement in $|B_z|$, caused by plasma absorption at Europa's surface and deceleration of field lines by the slow plume plasma. The flyby in scenario "D.1" crossed a small region in between the pile up of the magnetic field and the depletion region (see Figure 4.2(e)). Therefore, case "D.1" shows almost no perturbations in B_z, even though shifting the trajectory by $\approx 0.1\ R_E$ in x-direction would reveal the pile-up structure much more clearly (again, see Figure 4.2(e)). This case is a perfect example for the sensitivity of the detectability of plume signatures in magnetic field data, due to chosen flyby geometries. When the global atmosphere is included, the wakeside field B_z is reduced due to the flow deflection around the Alfvén wings, being strongest in the case of just an atmosphere ("JA", black line). The other cases ("D.2"-"D.4") reveal the presence of the plume in the form of a wiggly structure near C/A of similar magnitude. This feature is superimposed on the B_z signature generated by the global atmosphere, being weakest for case "D.4" (red dash-dotted line) and strongest

for "D.2" (blue dotted line).

4.5 Summary and Concluding Remarks

In this study, we have applied the three-dimensional hybrid simulation code AIKEF to investigate the effect of inhomogeneities in Europa's atmosphere (plumes) on the plasma interaction with the Jovian magnetosphere. To systematically assess the magnitude and structure of the perturbations associated with the plume-plasma interaction, we considered three locations of the plume source at Europa's surface: Europa's south pole, as well as the apices of its upstream and downstream hemispheres. These local plume sources have been combined with different symmetric and asymmetric density profiles (taken from Arnold *et al.*, 2019) of Europa's global atmosphere. To isolate the impact of a plume on Europa's magnetospheric environment, we also conducted a series of runs without any global atmosphere.

Runs with a plume at Europa's ramside apex showed highly confined regions (≈ 1.5 R_E in length and width) of water ions upstream of Europa. No pick-up tail in Europa's wakeside hemisphere is visible because the ions immediately re-encounter Europa's surface and are unable to gyrate around the moon. The reason for the absence of a pick-up tail in this case is the small extent of the plume, compared to the size of the moon, which is a major difference to the Enceladus plume. For a plume located at Europa's south pole, a complex, filamented fine structure forms in the plume's pick-up tail. For a plume located at Europa's downstream apex, a narrow, almost ray-like pick-up tail of plume ions forms along the corotation direction.

At a distance below 400 km to Europa's surface, the induced dipole from Europa's subsurface ocean dominates the magnetic field perturbations. Hence, when the dipole is included, the magnetic signatures of a plume will be close to the detection threshold. Flybys close to the center of Jupiter's magnetospheric plasma sheet, where the horizontal component of the background field is weak (resulting in a weak induced dipole (Zimmer *et al.*,

2000)) are therefore most suitable for plume detection through in-situ magnetic field and plasma observations.

The magnetic signatures of a plume are best visible in the (hypothetical) case without a global atmosphere. In this case, the plume generates an Alfvén wing with a pronounced north-south asymmetry. Taking into account the plasma interaction of Europa's global ionosphere severely complicates plume identification. While the plume still generates an Alfvén winglet superimposed on the main wing (see also Blöcker *et al.*, 2016), its visibility is determined by the ratio of the plume's density and the atmospheric density around the plume location. Our model shows that in the case of an asymmetric atmosphere (denser at Europa's ramside by a factor of 10), the signatures of a plume at the ramside apex are almost indiscernible. Irrespective of their location, plumes locally modify the draping signatures in B_x and generate distinct pile-up features in B_z, but remain almost "invisible" in B_y. The plasma quantity most diagnostic for the crossing of a plume is the bulk velocity $|\vec{U}|$, which is reduced within a radius of several R_E around the plume source. Overall, precise knowledge of the plasma's upstream parameters and the density profile of Europa's global atmosphere is required to identify plumes in plasma data. The detectability of their signatures depends highly on the spacecraft's trajectory.

CHAPTER 5
APPLYING ION ENERGY SPECTROGRAMS TO SEARCH FOR PLUMES AT EUROPA

The following chapter has been published by Arnold *et al.*, 2020b in the *Journal of Geophysical Research (Space Physics)* before submission of this dissertation. It is reproduced here in its entirety with the permission of John Wiley & Sons, Inc. The publication can be found under the following reference:

Arnold, H., Simon, S., & Liuzzo, L. (2020). Applying Ion Energy Spectrograms to Search for Plumes at Europa. Journal of Geophysical Research: Space Physics, 125, e2020JA028376. https://doi.org/10.1029/2020JA028376

5.1 Abstract

We constrain the diagnostic potential of ion energy spectrograms to identify signatures of water vapor plumes in the thermal plasma environment of Jupiter's moon Europa. For this purpose, we apply a hybrid model of Europa's Alfvénic plasma interaction to calculate the perturbations of the flow and the electromagnetic fields near the moon for various plume locations on its surface, combined with different sets of magnetospheric upstream conditions (corresponding to different distances between Europa and the center of Jupiter's plasma sheet). The model output is used to generate synthetic time series for the count rates of the observable thermal ion population as a function of energy along several hypothetical spacecraft trajectories as well as for the Galileo E26 flyby.

We demonstrate that the observability of characteristic plume signatures depends strongly on the viewing direction of the detector. Most surprisingly, for certain plume locations a particle detector facing away from Europa captures more clearly discernible signatures of a plume passage than a detector looking into the direction of the moon. This puzzling

result is caused by the deflection of magnetospheric and plume ions near Europa's Alfvén wings as well as a "contamination" of the spectrograms by cold plasma from the moon's global exosphere. The signature of the plume crossed during E26 is most clearly visible for a detector orientation that simultaneously captures the cold plume ions and a portion of the incident magnetospheric ion population. The results of this study will facilitate the planning of synergistic measurements during upcoming missions to Europa.

5.2 Introduction

Based on induction signatures seen in Galileo magnetometer data, Kivelson *et al.*, 2000 showed that Europa (radius $R_E = 1,560.8$ km) likely hosts a subsurface ocean with a depth on the order of 100 km. The thickness of Europa's icy crust proposed in the literature varies from a few km up to 60 km (Hand and Chyba, 2007; Hussmann *et al.*, 2002; Schenk, 2002). In December 2012, Hubble Space Telescope (HST) observations revealed an increase of ultraviolet emission in Europa's south polar region, which can be interpreted as a surplus of oxygen and hydrogen. Roth *et al.*, 2014a demonstrated that this inhomogeneity in Europa's atmosphere is consistent with one or two water vapor plumes with a scale height of about 200 km. Both plumes are expected to have vertical outgassing speeds of 500-700 m/s at Europa's surface (Roth *et al.*, 2014a). Based on further image post-processing of HST data, Sparks *et al.*, 2016, 2017 suggested the presence of two additional plume sources close to Europa's south pole and equator. However, this finding was recently put into question (Giono *et al.*, 2020). An additional transient source of water vapor on Europa's surface was recently identified in data from the Keck observatory (Paganini *et al.*, 2019).

Orbiting at a distance of 9.38 R_J (radius of Jupiter $R_J = 71,492$km), Europa is located within the Jovian plasma sheet (Kivelson *et al.*, 2009) and magnetosphere (Smith *et al.*, 1974). Because of Europa's large orbital period compared to Jupiter's rotational period, subsonic magnetospheric plasma continuously hits the moon's exosphere and ionosphere. The main mechanism behind the generation of Europa's thin molecular oxygen O_2 exo-

sphere (Burger and Johnson, 2004; McGrath *et al.*, 2009) is a combination of sputtering of its icy surface and radiolysis of the sputtered material by energetic particles (Cooper *et al.*, 2001). The intensity of Europa's surface sputtering decreases from the moon's ramside to its wakeside (Breer *et al.*, 2019; Cassidy *et al.*, 2013; Pospieszalska and Johnson, 1989), which results in a denser atmosphere in the trailing hemisphere (that faces the plasma flow) compared to the leading (wakeside) hemisphere. Electron impact ionization (being an order of magnitude stronger than UV ionization, see Saur *et al.*, 1999) partially ionizes Europa's thin exosphere. The asymmetry in the global atmosphere therefore maps into the structure of Europa's ionosphere.

The interaction between the sub-magnetosonic plasma flow at Europa, the induced magnetic field and the moon's ionosphere results in a "kink" in the magnetic field lines which propagates in both directions, northward and southward, along the field with the Alfvén velocity $v_A = |\vec{B}|/(\mu_0\rho)^{1/2}$, where $|\vec{B}|$ is the magnitude of the magnetospheric field, ρ is the mass density of the plasma and μ_0 the vacuum permeability. A system of non-linear standing Alfvén waves (called Alfvén wings) connects Europa to Jupiter's polar ionosphere (Neubauer, 1980; Neubauer, 1998). These wings carry currents that close within the moon's conducting ionosphere. A localized inhomogeneity in the atmosphere, due to, e.g., the presence of a plume in Europa's southern hemisphere, will enhance the current density and flow deceleration within the main Alfvén wing (Arnold *et al.*, 2019; Arnold *et al.*, 2020a; Blöcker *et al.*, 2016). This tube-like region of enhanced current density can extend to arbitrarily large distances from Europa (due to the translational invariance along the Alfvén wing characteristics, see Neubauer, 1980) and is referred to as an Alfvén winglet by Blöcker *et al.*, 2016. Therefore, a plume at, e.g., Europa's south pole, will break the symmetry of the Alfvén wings between the moon's northern and southern hemispheres. Jupiter's time-varying field at Europa induces a dipolar magnetic field in Europa's subsurface ocean (Khurana *et al.*, 1998; Zimmer *et al.*, 2000). Neubauer, 1999 predicted, Volwerk *et al.*, 2007 demonstrated (by analyzing Galileo Europa flyby data) and

Arnold *et al.*, 2020a confirmed (by using a hybrid plasma model) shrinking of the Alfvén wing cross-sections due to Europa's induced magnetic field.

In addition to remote telescope observations, recent studies have attempted to use magnetic field and plasma data from the Galileo encounters to identify plumes at Europa. Out of 12 targeted Europa flybys, only two flybys –E12 (on 16 December 1997) and E26 (on 3 January 2000)– passed by Europa's surface at an altitude comparable to the plumes' scale height (closer than 400 km, see Roth *et al.*, 2014a). Blöcker *et al.*, 2016 analyzed the magnetic field signatures observed during Galileo's E26 encounter by using a three-dimensional magnetohydrodynamic model. Their work led to novel findings regarding the physics of plume-plasma interactions (e.g., the concept of an Alfvén winglet) and also provided initial hints of a plume crossing during E26. Arnold *et al.*, 2019 re-analyzed magnetic field data from the E26 flyby by using the hybrid model AIKEF (Adaptive Ion-Kinetic Electron-Fluid, see Müller *et al.*, 2011). These authors were able to present strong evidence for a plume crossing by achieving good agreement with magnetic field data and by demonstrating that the observed fine structures in the magnetic field are not reproducible by simulations without a plume. Additional evidence for the crossing of a plume during E26 was recently found in energetic proton observations by Huybrighs *et al.*, 2020. These authors demonstrated that charge exchange and ion deflection near the plume cause a local decrease in the count rates of protons in the 115–244 keV regime, as observed by Galileo. Further, Jia *et al.*, 2018 analyzed magnetic field and plasma perturbations from the E12 flyby by using the BATS-R-US multifluid model. Similar to Arnold *et al.*, 2019, they were able to present strong evidence for a plume crossing in magnetic field and additionally, in plasma density data acquired around closest approach (C/A) of that flyby.

However, despite these findings, knowledge on the signatures that a plume would leave in in-situ spacecraft data is still limited. In particular, magnetic field data are available only along the spacecraft's trajectory, the orientation of the magnetic background field is variable in time and the locations of potential plumes across Europa's surface are largely

unknown and probably transient (Paganini *et al.*, 2019; Roth *et al.*, 2014a, 2016; Sparks *et al.*, 2016). Therefore, Arnold *et al.*, 2020a presented a systematic modeling framework for the identification of water vapor plumes in plasma and magnetic field data along hypothetical spacecraft flybys for different magnetospheric background field conditions, plume orientations, and exosphere models at Europa. In particular, Arnold *et al.*, 2020a considered plumes at Europa's south pole as well as at the apices of the moon's leading and trailing hemispheres. They systematically investigated how the observable magnetic field perturbations change when, e.g., the complexity of the model for Europa's global exosphere is increased or the induced dipole field from the subsurface ocean is taken into account. Overall, Arnold *et al.*, 2020a found that localized regions of stagnant flow are most indicative of the presence of a plume and that the visibility of plumes in the magnetic field is highly dependent on the density profile of the global atmosphere. However, Arnold *et al.*, 2020a mainly focused on the observable magnetic field perturbations and did not consider the imprint that potential plumes leave in, e.g., the particle energy spectra typically acquired by plasma detectors aboard spacecraft. The goal of the present study is to close this gap in our understanding of plume-plasma interactions at Europa.

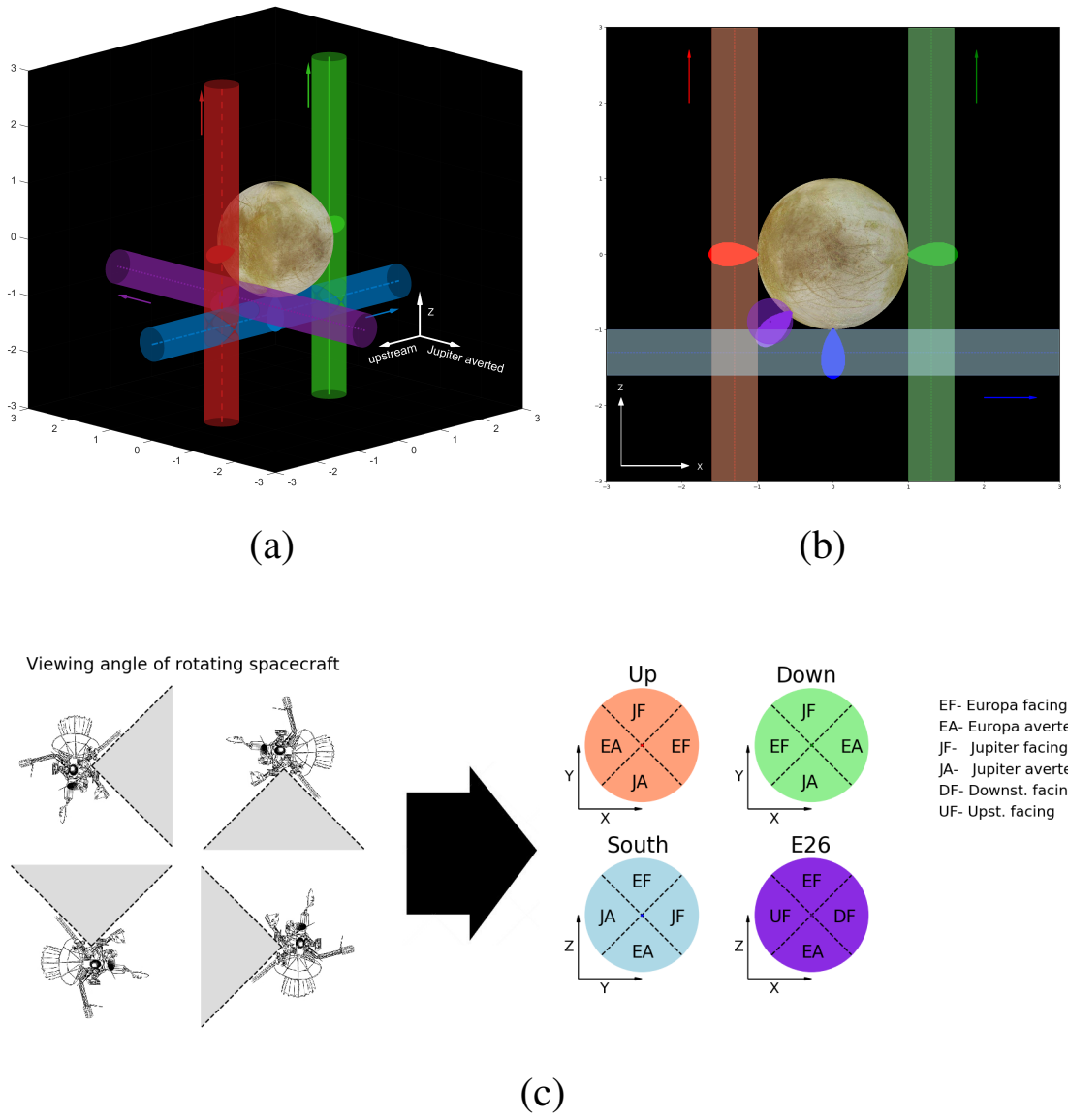

Figure 5.1: Setup of the synthetic detector geometry used to extract ion energy spectra from the hybrid simulations. In panels (a) and (b) the synthetic trajectories and plume locations considered in this study are displayed. The viewing point in panel (a) is located upstream of Europa and at the Jupiter-averted side, whereas in panel (b) we see Europa from viewing angles $(\theta, \phi) = (180°, 90°)$. The flyby trajectories considered are the same as in Arnold *et al.*, 2019; Arnold *et al.*, 2020a: the dotted, red line represents a (hypothetical) flyby through a plume located upstream ($x = -1.3\ R_E$, $y = 0$ and z varying), the blue line depicts a crossing of a south-polar plume (x varying, $y = 0$ and $z = -1.3\ R_E$), and the green line corresponds to a flyby through a plume located at Europa's leading/downstream apex ($x = 1.3\ R_E$, $y = 0$ and z varying), respectively. During the upstream (red) and downstream (green) flybys, the spacecraft travels northward (toward positive z values), whereas during the south-polar flyby the spacecraft travels toward downstream (x value increasing). Additionally, the violet line corresponds to the E26 flyby geometry, which is approximated by a line fit through the C/A of the E26 encounter ($x = -0.83 R_E$, y varying and $z = -0.89 R_E$), see Arnold *et al.*, 2019. The light colors in panels (a) and (b) depict the tube-like regions around the respective trajectories (with radius $0.3\ R_E$) in which particles are collected. The bottom row (c) illustrates the idea behind the detector geometry. In our model, the particle detector is divided into four wedge-like quarter-cylinders, each with an opening angle of 90°. The axis of each quarter-cylinder is aligned with the spacecraft trajectory, i.e., the model detectors always "look" in directions perpendicular to the trajectory. On the left side of (c), the resulting viewing angle is presented for different orientations of the spacecraft. On the right side of (c), we show the orientation of the four quarter-cylindrical detectors for each trajectory and their corresponding nomenclature.

This study will build upon the work of Arnold *et al.*, 2020a. The hybrid model of Arnold

et al., 2020a treats ions as individual (macro)particles, allowing us to analyze the kinetic energy distribution of particles in any given cell of the simulation domain (in contrast to fluid models of moon-plasma interactions, which need to make assumptions on the shape of the local velocity distribution). In this way, we can determine the ion energy distribution along hypothetical trajectories that intersect plumes at different surface locations, similar to the magnetic field signatures along synthetic trajectories discussed by Arnold *et al.*, 2020a. Unfortunately, thermal ion energy spectrograms from the Galileo E12 and E26 flybys are not available in the peer-reviewed literature, and the time resolution of the Galileo datasets is likely too coarse to further constrain any signatures of the plumes seen in magnetic field data. However, future missions (like, e.g., the Europa Clipper and the JUpiter Icy moons Explorer JUICE) may very well be able to acquire time series of the ion energy distribution that are sufficiently detailed to search for possible plume signatures. For Enceladus it has already been shown that plumes are visible in thermal ion energy spectrograms obtained by the Cassini spacecraft (Tokar *et al.*, 2009). Therefore, we will conduct a systematic search for characteristic signatures of cold plume plasma in our modeled energy spectrograms and provide a framework for identification of plume signatures in particle data for upcoming in-situ flyby missions.

In their preceding studies, Arnold *et al.*, 2019; Arnold *et al.*, 2020a have generated an extensive pool of hybrid plasma simulations for different upstream conditions, global exosphere models and plume configurations at Europa. For this study, we shall select several hybrid model runs from that pool and use them to generate synthetic ion energy spectrograms. These spectrograms will then be applied to evaluate the challenges associated with the identification of plume signatures using in-situ particle data.

This paper is organized as follows: In section 2 we give a brief introduction to the model of Arnold *et al.*, 2019; Arnold *et al.*, 2020a and describe the assumptions necessary to generate synthetic ion energy spectra. In particular, we explain how the limited field of view of a ”real” particle detector is taken into account. Section 3 presents the analysis

of synthetic ion energy spectrograms for different plume-plasma interaction scenarios and detector viewing geometries. We consider the same plasma interaction scenarios as Arnold *et al.*, 2019; Arnold *et al.*, 2020a to complement the analysis of magnetic field signatures along synthetic and real flyby trajectories presented in these two studies. In particular, we present model results for the expected particle signatures of the plume observed during E26 (Arnold *et al.*, 2019). Section 4 concludes the paper with a summary of our major findings.

5.3 Model Description

5.3.1 Hybrid Code Setup

Like Arnold *et al.*, 2019; Arnold *et al.*, 2020a we use the hybrid code AIKEF (Müller *et al.*, 2011), which treats ions as (macro)particles and electrons as a massless, charge-neutralizing fluid. Thus, our model is able to describe the flow shear between the magnetospheric plasma and Europa's ionospheric species (plume and exosphere). Blöcker *et al.*, 2016 and Arnold *et al.*, 2019 showed that, to study plume-plasma interactions at Europa, it is essential to use a model that takes into account the ionospheric Hall effect within the plumes. In addition to Europa's plasma environment, AIKEF has already been applied, e.g., to analyze flybys through the Enceladus plume (Kriegel *et al.*, 2009, 2011, 2014) and to study induction and plasma interaction signatures at Callisto (Liuzzo *et al.*, 2015, 2016; Liuzzo *et al.*, 2017; Liuzzo *et al.*, 2018).

In this study we analyze synthetic ion energy spectrograms for three model setups. Within each setup, the magnetospheric upstream parameters and the model of Europa's global atmosphere are kept the same. For each of these three setups we have carried out multiple simulation runs, placing a local plume source at different locations on Europa's surface. Setups #1 and #2 consist of three runs each, with the plume source located at Europa's south pole and the apices of its leading and trailing hemispheres, respectively. In each model run, only a *single* plume source is considered. For the spectrograms of setups #1 and #2 we use the model configurations described in detail in sections 2 and 3 of

Arnold *et al.*, 2020a. Setups $\#1$ and $\#2$ differ only in the strength and orientation of the magnetospheric background field $\vec{B}_0$, which also determines the magnetic moment induced in Europa's subsurface ocean. For the third setup, we use the model parameters of Arnold *et al.*, 2019, which correspond to the plasma environment during the Galileo E26 flyby of Europa. In this setup, the location of the plume is chosen in agreement with actual Galileo magnetometer observations from E26.

We use the Cartesian coordinate system EPhiO for our model. In this coordinate system, the x axis is aligned with the corotational plasma flow direction, the y axis points toward Jupiter, the z axis completes the right-handed system and the origin coincides with Europa's center. Additionally, to describe the location of the plume's footpoint for our different plasma interaction scenarios, we use a spherical coordinate system on Europa's surface. In this system (r, θ, ϕ), r is equal to Europa's radius, the latitude θ is measured from the positive z axis and ϕ denotes West Longitude measured clockwise from the positive y axis.

In all seven model runs presented in this paper (three runs each for setups $\#1$ and $\#2$, and one run for the E26 setup), we apply an asymmetric density profile for Europa's global atmosphere, which we assume to consist of molecular oxygen and which is in agreement with observations (Hall *et al.*, 1995; McGrath *et al.*, 2009). A detailed description of the applied model for Europa's atmospheric density profile can be found in Arnold *et al.*, 2020a. All model runs of setups $\#1$ and $\#2$ have already been discussed in Arnold *et al.*, 2020a. Therefore, we only provide a brief recap of the upstream parameters. The bulk velocity of the (partially) corotating plasma is set to $u_0 = 100$ km/s, which is in agreement with Kivelson *et al.*, 2009 and Bagenal *et al.*, 2015. The number density of the upstream ions is $n = 60 \cdot 10^6$ m^{-3}, within the range measured during various Galileo flybys (Kivelson *et al.*, 2004; Kurth *et al.*, 2001). The mass of the singly charged upstream ions is set to $m_i = 18.5$ amu, and the ion and electron temperatures read $k_B T_i = k_B T_e = 100$ eV (Kivelson *et al.*, 2004). The plasma parameters for the third setup (conditions during the Galileo E26 flyby) are equal to run $\#2$ of Arnold *et al.*, 2019. The bulk velocity of the

upstream plasma is again $u_0 = 100$ km/s along the x axis (Bagenal *et al.*, 2015) and its number density is set to $n = 30 \cdot 10^6$ m^{-3} (Kurth *et al.*, 2001), as observed during the E26 flyby.

The vector of the magnetospheric background field for runs of setup $\#1$ is $\vec{B_0} = (0, 0, -450)$ nT. This field orientation and strength coincide with measurements taken when Europa was located close to the center of Jupiter's magnetospheric plasma sheet (Kivelson *et al.*, 1999). The induced magnetic moment from Europa's subsurface ocean disappears under these conditions, i.e., the magnetospheric plasma interacts with the moon's atmosphere/ionosphere alone. In setup $\#2$ we set the vector of the magnetospheric background field to $\vec{B_0} = (0, -210, -450)$ nT. This orientation corresponds to the case when Europa is located near the northern edge of Jupiter's magnetospheric plasma sheet. In this scenario the induced dipole from Europa's subsurface ocean dominates the plasma interaction. The induced dipole moment points in $(+y)$ direction and its magnitude can be found in Arnold *et al.*, 2020a. For the E26 scenario we use the magnetospheric background field observed during the actual Galileo flyby: $\vec{B_0} = (-22, 205, -379)$ nT (Kivelson *et al.*, 2009), again yielding a non-vanishing induced dipole moment that is (mostly) antiparallel to the y axis. The parameters for all three setups result in a plasma beta of $\beta \approx 0.01$, an Alfvénic Mach number of $M_A \approx 0.3$, and a magnetosonic Mach number of $M_{MS} \approx 0.3$.

For model setups $\#1$ and $\#2$, we analyzed runs for three plume locations, as provided by Arnold *et al.*, 2020a. The footpoint F of the plume is located either at the apex of the trailing hemisphere (upstream "U", in spherical coordinates $(r, \theta_F, \phi_F) = (R_E, 90°, 270°)$), the apex of the leading hemisphere (downstream "D", $(r, \theta_F, \phi_F) = (R_E, 90°, 90°)$), or at Europa's south pole ("S", $(r, \theta_F, \phi_F) = (R_E, 180°, 0°)$). In all runs of setups $\#1$ and $\#2$ the plume axis is oriented perpendicular to Europa's surface. For the E26 setup, the plume observed by Galileo was located in Europa's trailing, southern hemisphere ($(r, \theta_F, \phi_F) = (R_E, 140°, 300°)$) and (in contrast to setups $\#1$ and $\#2$) the plume axis is not perpendicular to Europa's surface anymore (see Arnold *et al.*, 2019 for details). The properties of the

plume within all three model setups are kept unchanged, with a scale height of $h_p = 200$ km, opening angle $h_\theta = 15°$ and surface density $n_{p,0} = 3.9 \cdot 10^{15}$ m^{-3}. These values are consistent with the models of Jia *et al.*, 2018 and Arnold *et al.*, 2019; Arnold *et al.*, 2020a and result in column densities of the plume similar to those observed by HST (Roth *et al.*, 2014a; Sparks *et al.*, 2016).

The extension of the simulation domain is the same as in Arnold *et al.*, 2019; Arnold *et al.*, 2020a: $-10\ R_E \leq x \leq 20\ R_E$, $-15\ R_E \leq y \leq 15\ R_E$, and $-30\ R_E \leq z \leq -30\ R_E$. The simulation grid contains two refinement levels centered around (0,0,0): the grid resolution is 33 km for $|x, y, z| \leq 1.5\ R_E$, 66 km for $1.5\ R_E < |x, y, z| \leq 3\ R_E$ and 132 km at larger distances. The simulations reach stationarity after about one passage of the plasma flow through the simulation domain.

5.3.2 Particle Detector Setup

Galileo was equipped with two instrument suites which were able to measure particle energies: the Plasma Subsystem (PLS) and the Energetic Particles Detector (EPD). The purpose of PLS was to study Jupiter's thermal plasma environment, whereas EPD was designed to measure the high-energy particle populations within Jupiter's radiation belts. Therefore, PLS covered an energy-per-charge (E/q) range from 0.9 eV to 52 keV and EPD from 20 keV to 55 MeV, respectively (Frank *et al.*, 1992; Paterson *et al.*, 1999). Plume ions are injected into the corotating plasma at energies below 1 eV (e.g., Arnold *et al.*, 2019; Blöcker *et al.*, 2016); therefore we do not expect them to leave a discernible signature in the data collected by an energetic particle detector. However, we note that a plume source may *indirectly* affect energetic ion observations near Europa by, e.g., deflecting the energetic ions through the perturbed fields within the Alfvén winglet (Breer *et al.*, 2019; Huybrighs *et al.*, 2020). Our study focuses on generating synthetic ion energy spectra for the thermal plasma flow near Europa at energies below a few keV.

Due to computational limitations on the number of particles within the hybrid simulation, our model can not capture the exact details of an actual ion detector that is point-like compared to any length scales of the plasma interaction. However, one limiting factor of both Galileo instruments was the finite viewing angle of the respective detector. Our model allows to explore the influence of a finite viewing angle on ion observations near Europa and on the feasibility to identify local plume sources in ion energy spectra. To create a suitable simulation setup, we have chosen to move a spacecraft along synthetic trajectories through the plume sources described in section 2.1 (see Figure 5.1, panels (a) and (b)). The model detector has a viewing angle of 90° and covers the energy range of $0 - 3000$ eV, thereby capturing the entirety of the (thermal) plasma population within the hybrid simulations.

Similar to the Galileo E12 and E26 flybys (which were the only encounters to detect plume sources at Europa), we have chosen a closest approach altitude of 0.3 R_E for the synthetic trajectories in setups #1 and #2. We also keep the flyby geometries simple, by varying only one coordinate along each trajectory (x for the south-polar plume and z for the plumes located at the upstream and downstream apices), in exactly the same way as Arnold *et al.*, 2020a. Additionally we generate a set of synthetic ion energy spectra for the E26 flyby geometry, by analyzing ion energies along a straight line fit through C/A of the E26 encounter (see also Figure 1 in Arnold *et al.*, 2019). The synthetic flyby geometries and the associated plume sources are illustrated in the top row of Figure 5.1: (red) upstream flyby, plume at Europa's ramside apex, (green) downstream flyby, plume at Europa's wakeside apex, (blue) south-polar flyby, plume at Europa's south-pole, (purple) E26 flyby geometry and plume source, as observed by Galileo. The magnetic field perturbations observable along these trajectories are discussed in Arnold *et al.*, 2020a for the first three cases and in Arnold *et al.*, 2019 for E26.

On the length scales of the plasma interaction, a spacecraft has negligible size, and within our hybrid model it would be completely "buried" within a single cell of the simula-

tion grid. However, such a point-like spacecraft would barely be hit by any macroparticles in the model, thereby drastically blurring the modeled spectrograms and increasing the simulation runtime beyond feasibility. Therefore, to generate meaningful results, we have to artificially increase the "effective size" of the region where the detector is able to collect particles. While this region is much larger than in reality, we still keep its size way below the length scales upon which the fields in Europa's plasma interaction region undergo significant changes. In this way, we ensure that the model detector does not average over structures of different physical origin. As shown in Figure 5.1 (c), our model detectors are able to "capture" all particles within a cylindrical tube around each spacecraft trajectory. To study the impact of a finite viewing angle on the modeled spectrograms, each tube is divided into four quarter-cylindrical, wedge-like "sub-detectors", the axes of which are aligned with the spacecraft trajectory. The opening angle of each sub-detector is $90°$. This setup roughly simulates what the Europa Clipper plasma instrument would see during a flyby with fixed orientation of the spacecraft (Grey *et al.*, 2018).

For the plume crossings in setups # 1 and # 2, this results in a segment facing Europa (therefore facing the plume source), an Europa-averted segment, as well as a Jupiter-facing and Jupiter-averted segment, respectively (see Figure 5.1 (c)). During E26, the Galileo spacecraft moved mainly in $(+y)$ direction. In this case, the four sub-detectors used to generate synthetic ion energy spectrograms look in $\pm x$ direction (i.e., toward upstream/downstream) and in $\pm z$ direction (i.e., northward/southward), respectively. The synthetic ion energy spectrograms recorded by *each* of the four "sub-detectors" are analyzed in our study.

This study mainly focuses on isolating the role of a finite viewing angle for a low-energy plasma detector on observations of plume-plasma interactions. To facilitate straightforward access to the involved physics, the model spacecraft does *not* rotate as it travels through the hybrid simulation domain, i.e., the four quarter-cylindrical detectors have a *fixed* orientation and viewing direction with respect to the EPhiO system and the spacecraft trajectory.

During an actual spacecraft flyby through a plume at Europa, the situation would be more complicated (see section 4). However, there are no observed ion energy spectrograms of plume-plasma interactions at Europa available in the literature (neither for E12 nor for E26) to which our model output could be compared at the present time. Therefore, our study rather serves as a "guide" for the interpretation of thermal ion observations from future flybys of Europa.

In our simulation setup, ions are represented by 45 macroparticles per cell and species (collections of particles, that have the same charge-to-mass ratio as a real ion) at the highest refinement level (cubes with a length of 33 km). This value is by many orders of magnitude lower than the number of ions populating such a cube in reality. We therefore extend the area of detection to a cylindrical tube of radius $0.3\ R_E$ around each trajectory (see Figure 5.1, panels (a) and (b)). We have verified that while reducing the radius of the cylindrical detection region to values below 0.3 R_E does blur the spectrograms, it does *not* add or change any of the physical structures seen. However, only a small fraction of the particles located within the quarter-cylindrical detection segment is actually counted by the respective detector: In order to be registered by a certain detector segment, the velocity vector of a particle must point toward the detector and must be (anti)parallel to the symmetry axis of the respective quarter-cylindrical segment. For example, the velocity vectors $\vec{v} = (v_x, v_y, v_z)$ of particles inside the tube-like region around the upstream flyby trajectory (the red area in panels (a) and (b) of Figure 5.1) have to fulfill the following criteria to be detected: $v_y < 0$ for the Jupiter-facing, $v_y > 0$ for the Jupiter-averted, $v_x > 0$ for the Europa-averted and $v_x < 0$ for the Europa-facing segment, respectively (see Figure 5.1 (c)). This approach partially takes into account the limitations associated with the finite viewing angle of an actual particle detector: in a real world scenario, the velocity vector of a particle has to be opposite to the temporary viewing direction and location of the detector to enter the device and be registered.

We note that our approach does *not* consider several components of the interaction that

the plumes may contribute to: (1) Our model does not take into account any interaction between the thermal ions and the neutral gas. However, ion detectors are sensitive to dropouts in the particle signatures that result from locally increased neutral densities (Huybrighs *et al.*, 2020). (2) For some missions, the spacecraft velocity may be sufficient to change the observable energy of the ions by a few eV. This effect would have to be included at the lowest energies considered. However, since we do not attempt to reproduce ion observations from a specific, real-world flyby scenario (with known spacecraft velocity), this slight change in energy is not taken into account by our model. (3) Depending on the configuration of the mission, spacecraft charging may also locally affect the dynamics of the thermal ions.

5.4 Results

In this section, we discuss the synthetic ion energy spectrograms generated for the two generic plasma interaction setups ($\#1$, $\#2$) as well as for the E26 flyby. To facilitate the interpretation of the spectrograms, we also display the bulk parameters of the plasma flow. A more detailed discussion of the macroscopic plasma properties (bulk velocity U and the number densities of the three ion species) for setups $\#1$ and $\#2$ can be found in Arnold *et al.*, 2020a. The plasma properties for the E26 flyby have been discussed in more detail by Arnold *et al.*, 2019.

The spectrograms presented in this study take into account all three ion species included in the hybrid model (upstream ions O^+, exospheric ions O_2^+, and plume ions H_2O^+), see Arnold *et al.*, 2019; Arnold *et al.*, 2020a. The upstream plasma properties discussed in section subsection 5.3.1 result in a drifting Maxwellian distribution centered around an energy of $E = 0.5\ m(\mathrm{O}) \cdot (100\ \mathrm{km/s})^2 = 835$ eV with width of $kT = 100$ eV, extending symmetrically to both, higher and lower energies. This distribution is visible at sufficiently large distances to Europa where the plasma perturbations fade away. The plume ions are inserted with an initial velocity of 0.5 km/s along the plume axis (which is slightly below

the escape velocity), i.e., their initial energy right after ionization is $E = 0.5\, m(\mathrm{H_2O}) \cdot (0.5$ km/s$)^2 \approx 0.02$ eV.

5.4.1 Setup #1: Plasma interaction with a plume and an asymmetric global atmosphere

In the following, we discuss the ion energy spectrograms obtained for flybys through plumes at three different locations. We again emphasize that a separate simulation run has been carried out for each plume location, i.e., there is *no* run that considers all three plumes simultaneously. The model results for the electromagnetic fields in setup #1 are presented by Arnold *et al.*, 2020a.

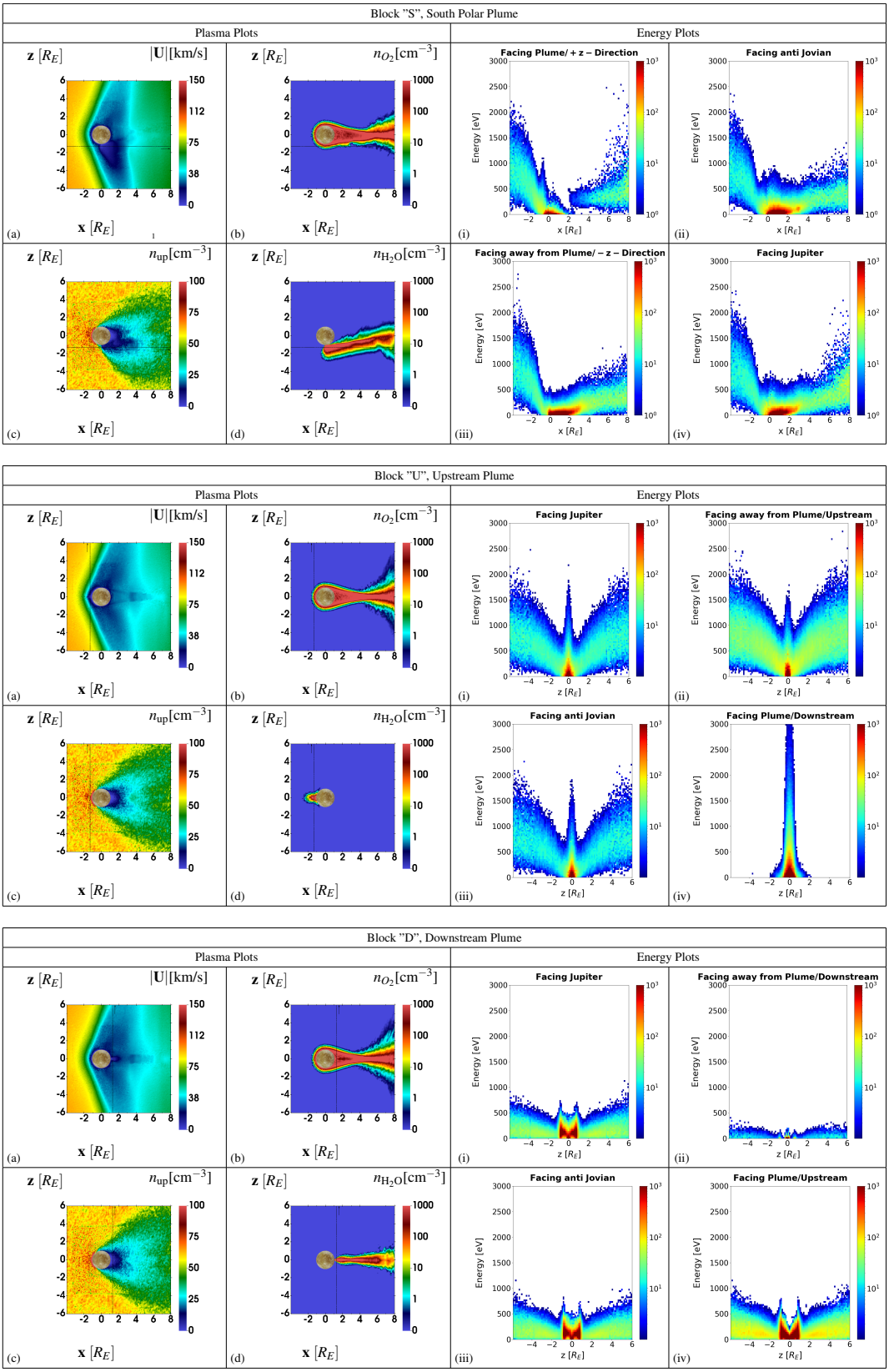

Figure 5.2: Bulk properties of the plasma flow and synthetic ion energy spectrograms for setup #1. For each plume location on the surface ("S": south-polar, "U": upstream, "D": downstream), the three blocks of the figure display, on the left side, (a) the ion bulk velocity, (b) the ion density associated with Europa's global exosphere, (c) the upstream ion density, and (d) the plume ion density in the (x, z) plane of the EPhiO system. The panels on the right side ((i)–(iv)) show the modeled ion energy spectrograms for the corresponding spacecraft trajectories and detector orientations from Figure 5.1. In the spectrograms, the color bar provides the number of counts and energy is given in eV. In block "S", the spacecraft moves along the $(y = 0, z = -1.3R_E)$ line, whereas in block "U" the hypothetical trajectory is located at $(x = -1.3R_E, y = 0)$. In block "D", the spacecraft trajectory is given by $(x = +1.3R_E, y = 0)$.

South-polar plume

In the scenario of a south-polar plume, the hybrid model results show the stagnation of the plasma flow (see Figure 5.2, block "S", panel (a)) near the symmetric main Alfvén wing, as well as the plume's Alfvén winglet in Europa's southern hemisphere. Since $\vec{B_0}$ is aligned with the $(-z)$-axis, the ions from Europa's global atmosphere escape in a narrow tail, symmetric between the $z > 0$ and $z < 0$ hemispheres (see Figure 5.2, block "S", panel (b)). The plume ions, on the other hand, leave Europa in a pick-up tail inclined toward the north, since the $\vec{E} \times \vec{B}$ drift is perpendicular to the draped field lines within the southern wing characteristic (see Figure 5.2, block "S", panel (d)).

In Figure 5.2, block "S", panels (i)-(iv) the ion energy spectra for the flyby through a south-polar plume are shown. Approaching the plume from the upstream side ($x < 0$), all four spectrograms display the gradually declining contribution of the unperturbed upstream plasma (drifting Maxwellian centered around 835 eV) to the total particle counts for all four viewing directions of the detector. At $x \approx -2\ R_E$ the spacecraft begins to observe the energy drop of the upstream ion population because of the deceleration of the plasma within the main Alfvén wing. This effect is particularly strong near $x \approx 0\ R_E$, when the spacecraft enters the Alfvén winglet generated by the cold plume plasma (see Figure 5.2, block "S", panel (a)). Around this point along the trajectory, the spacecraft also enters the tail of newly generated plume ions. The plume ions form a distinct region of dense, low-energy plasma downstream of $x = 0$ (dark red in all four spectrograms for the southern plume, see Figure 5.2, block "S", panels (i)-(iv)). The spacecraft remains immersed into low-energy plume plasma as it continues to travel toward downstream, until the trajectory leaves the dense center of the inclined tail of plume ions beyond $x > 5\ R_E$. This is particularly well visible in Figure 5.2, block "S", panel (iii) where the particle energy steadily increases as the spacecraft travels farther downstream and the contribution of the cold plume ions to the total number of counts gradually drops.

The spectrograms observed by a Jupiter-facing (Figure 5.2, block "S", panel (iv)) and

a Jupiter-averted (Figure 5.2, block "S", panel (ii)) detector are nearly identical, since the gyroradii of plume ions (≈10 km) in the strong magnetic field near Europa are only a small fraction of moon's radius. However, the most striking result of this run is revealed by comparing the spectrograms in panels (i) (detector pointing toward Europa) and (iii) (detector pointing away from Europa) of Figure 5.2, block "S": the signature of the plume in the ion energy spectrograms is much more prominent when the detector is directed *away* from the surface of Europa, i.e., *away* from the actual location of the plume. Due to the inclination of the magnetic field lines in the southern Alfvén wing, the guiding center trajectories of the drifting plume ions are slightly inclined northward. Therefore, these pick-up ions move *away* from a detector looking toward Europa and *toward* a detector facing the opposite direction.

For a spacecraft trajectory that passes Europa closer than the scale height of a south-polar plume this means that even a weak tilt in the magnetic field near Europa has a discernible effect on the detectability of the plume in thermal ion energy spectrograms. The strongest signal of a south-polar plume in ion energy data is expected when the spacecraft actually crosses the plume, but the detector looks *away* from Europa. With increasing Alfvénic Mach number of the upstream flow and thus, increasing tilt of the southern wing characteristic against the z axis, this surprising effect will become more pronounced. For a detector looking toward Europa, the tilt in the plume ion trajectories even causes a complete (but very narrow) depletion of the observable ion population immediately downstream of $x = 0$ (see Figure 5.2, block "S", panel (i)): the plume ions can not enter this detector, since their motion is aligned with the viewing direction. Simultaneously, the magnetospheric ions are deflected around the densest region of the plume (Arnold *et al.*, 2020a) and can not reach this detector either.

Upstream plume

The plasma quantities for a plume located at Europa's upstream apex are nearly symmetric between the $z > 0$ and $z < 0$ half spaces, since the plume axis is aligned with $z = 0$ and the magnetic field points in $(-z)$-direction (see Figure 5.2, block "U", panels (a)–(d)). The perturbations generated by the plume are mainly confined to the upstream region, since newly generated plume ions are immediately picked-up and "rain" back onto Europa's surface (see Figure 5.2, block "U", panel (d) and discussion in Arnold *et al.*, 2019; Arnold *et al.*, 2020a). Most notably, the plume ions do *not* form a pick-up tail downstream of Europa in this case. The narrow tail formed by ions from the global atmosphere qualitatively resembles the tail formed in the case of a south-polar plume, with the slight differences in the electromagnetic field perturbations introducing only very subtle changes to the overall tail structure far downstream of Europa (see Figure 5.2, block "U", panels (b) and (d)).

In the modeled ion energy spectra for a plume located at Europa's upstream apex, the plume generates a distinct, ray-like enhancement in the ion count rates (at low energies of only a few eV) around $x = 0$. This enhancement is much narrower than in the south-polar case since the spacecraft only briefly intersects the region populated by cold plume ions. Except for the detector looking toward Europa (see Figure 5.2, block "U", panel (iv)), the drifting Maxwellian distribution of the magnetospheric upstream ions is clearly discernible around energies of 835 eV. The "gap" in the upstream ion population is much narrower than in the south-polar case because the region populated by plume ions is confined to a narrow "pillar" upstream of Europa (see Figure 5.2, block "U", panel (d)). In addition, the trajectory in front of Europa passes the ion deflection region around the Alfvén wings within the interval of $-2R_E \leq z \leq 2R_E$. The plume signal is most clearly visible in the detector facing Europa's surface (see Figure 5.2, block "U", panel (iv)), since no upstream plasma enters this detector from the $(-x)$ direction. Also, the scale height of the plume exceeds the scale height of the global atmosphere, i.e., only very few pick-up ions from the global atmosphere contribute to the observed signature. The spectrogram recorded by the

Europa-facing detector is therefore not ”contaminated” by signatures of the other thermal ion species involved in Europa's plasma interaction. This is “convenient”, since only a highly sensitive mass spectrometer could discriminate between the water group ions from the plume and oxygen ions from the upstream flow.

The upstream flow directly enters the Europa-averted detector (see Figure 5.2, block ”U”, panel (ii)) and generates a broad signature throughout almost the entire flyby. Since the twisting of the plasma flow direction by the Hall effect within Europa's “main” Alfvén wings (generated by the global exosphere) is rather weak (Arnold *et al.*, 2020a; Kivelson *et al.*, 2004; Simon *et al.*, 2011), there is no significant motion of the plasma toward the Jupiter-facing (Figure 5.2, block ”U”, panel (i)) and Jupiter-averted detectors (Figure 5.2, block ”U”, panel (iii)) along a trajectory in the $y = 0$ plane. Upstream particles entering these two detectors are mainly driven by thermal motion. Therefore, the upstream ion counts observed by a detector facing upstream are higher than the counts measured in the other three detector orientations.

Hence, to identify an upstream plume in ion energy spectra without ”contamination” by other ion species, a detector looking toward Europa (while remaining outside of the global atmosphere) seems to be the most promising approach. Additionally, we note that the plume location in this run is not too dissimilar from that of the E26 plume. Therefore, these results suggest that, if the PLS detector aboard Galileo had been looking toward Europa, the chances of capturing a signature of the E26 plume would have been high. However, the E26 scenario is still more complicated due to the induced dipole field and the inclination of the upstream field. Details are discussed in section 3.3.

Downstream plume

Similar to the run with an upstream plume, the Alfvén wings are symmetric between the north and south (see Figure 5.2, block ”D”, panel (a)). No longer being blocked by Europa, the plume forms a narrow pick-up tail (Figure 5.2, block ”D”, panel (d)) that is completely

immersed in the ”main” pick-up tail emerging from the global ionosphere (Figure 5.2, block ”D”, panel (b)). Since the plume is not directly exposed to the upstream plasma, the plume's signature is nearly invisible in the bulk velocity and the magnetic field (Arnold *et al.*, 2020a). The deflection of the plasma flow is mainly determined by the interaction with Europa's global ionosphere, rather than by the plume ”hidden” in Europa's wake.

The ion spectra for a flyby through a plume at Europa's downstream apex are nearly devoid of any signatures of the upstream plasma. In Europa's wake the flow has already been drastically decelerated by mass loading. As can be seen from Figure 5.2, block ”D”, panels (i)-(iv), there are practically no plasma particles observed with energies in excess of 500 eV. For a detector facing downstream (Figure 5.2, block ”D”, panel (ii)) no clear signal is visible from any ion population, since all ion species mainly move into the Europa-averted direction. Only the thermal motion of magnetospheric and exospheric plasma can be captured by a detector in this viewing geometry. The other detector geometries show an M-like signature of cold plasma within the moon's geometric plasma shadow ($-1R_E < z < 1R_E$). While the masses of plume ions and exospheric ions are very similar, the M-like signature visible in panels (i), (iii), and (iv) of Figure 5.2, block ”D”, is indeed mainly generated by Europa's global exosphere. The two ”spikes” of the M feature occur near the points where the spacecraft enters or leaves Europa's geometric plasma shadow. Around these locations, the column density of ionospheric plasma is largest (along straight lines parallel to the x axis), whereas it minimizes in the middle of the M feature around $x = 0$ (see also Figure 1 of Simon, 2015). Since the gyroradii of escaping ions at Europa are small, assuming them to move along straight lines parallel to the x axis is a reasonable approximation, at least in the immediate vicinity of the moon. Therefore, the amount of escaping plasma ”along a line of sight” (parallel to the x axis) is largest at the edges of Europa's geometric plasma shadow and minimizes at its center, thereby generating the M-like feature in our modeled spectrograms. In other words, at the edges of Europa's geometric plasma shadow, escaping ions from the moon's ramside are no longer “blocked”

by the solid body, thereby causing a local enhancement in the net outflow.

The fact that the escaping plume ions are unable to generate a third spike in the middle of the M signature suggests that the contribution of these ions is completely "obscured" by pick-up from the global exosphere. However, as will be discussed in the next section, this actually changes when Europa is located away from the center of Jupiter's plasma sheet and the induced dipole field needs to be included.

Like in Arnold *et al.*, 2020a, the downstream plume is neither visible in the magnetic field nor in the plasma bulk velocity. The plume is not clearly discernible in the ion energy spectra either. In order to identify the downstream plume in the admixture of ion species in Europa's wake, a high-resolution mass spectrometer would be needed to discriminate between the H_2O (plume), the O (upstream) and the O_2 (ionosphere) species. Judging from magnetic field and ion energy spectrograms only, a spacecraft could indeed cross an active plume at Europa's downstream apex without detecting any discernible signatures of its presence. We also note that mere sputtering of Europa's surface ice releases H_2O molecules as well (e.g., Cassidy *et al.*, 2013). In data from a mass spectrometer, these particles would "compete" with the water molecules associated with an active plume eruption. However, while much lower than the energy of the incident magnetospheric ions, particles emanating from the plume and from surface sputtering would likely still have distinctly different energies.

5.4.2 Setup #2: Plasma interaction with an induced dipole, a plume, and an asymmetric global atmosphere

In this setup the orientation of the magnetic background field is $\vec{B_0} = (0, -210, -450)$ nT. Due to the non-zero B_y component of the background field, the Alfvén wing characteristics are no longer located in the $z = 0$ plane. The northern wing is inclined toward Jupiter, whereas the southern wing is tilted away from Jupiter by about $25°$. Additionally, the cross-section of the Alfvén wing is reduced by the presence of an induced dipole (Neubauer, 1999), see Figure 5 of Arnold *et al.*, 2020a.

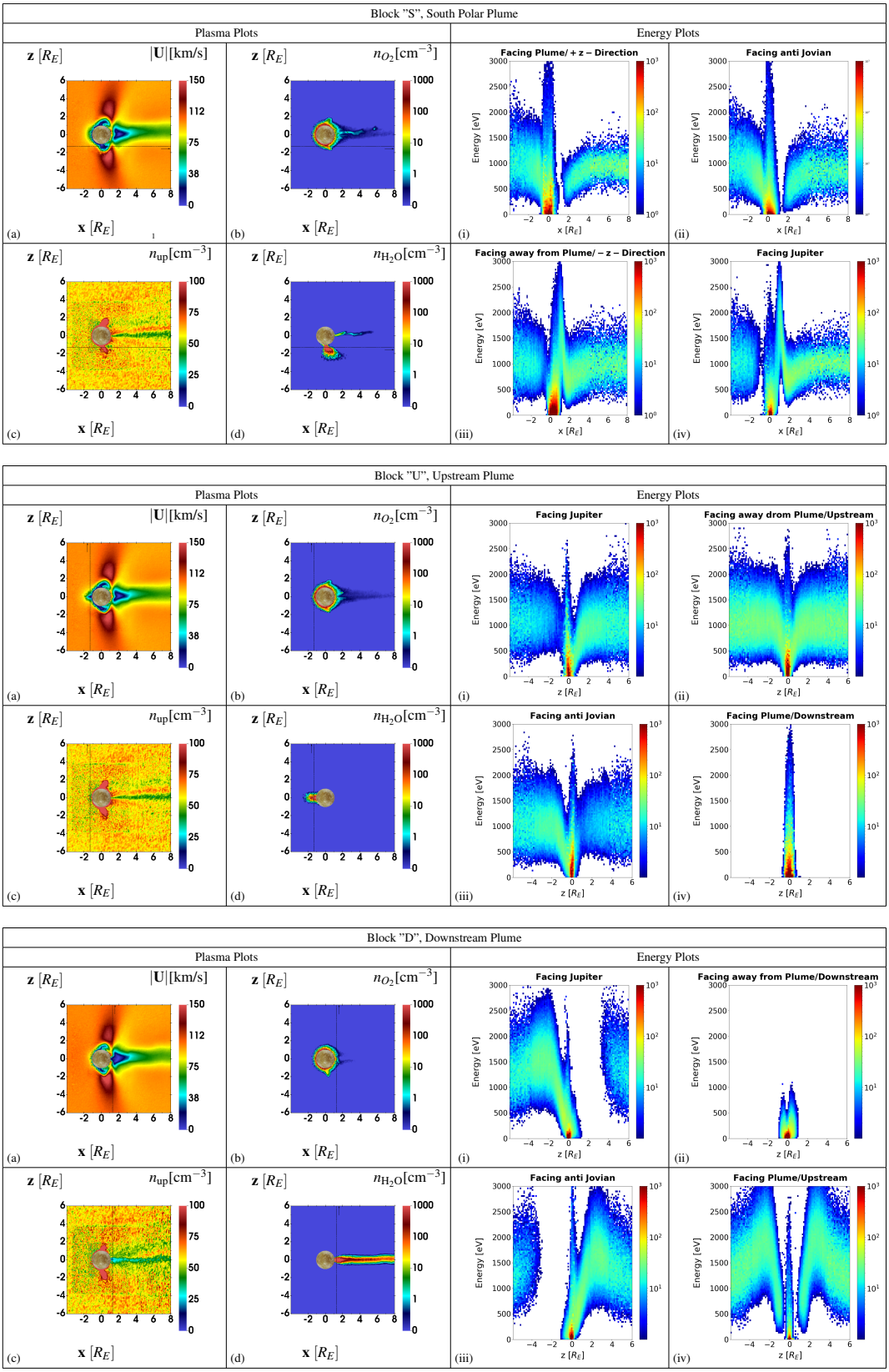

Figure 5.3: Bulk properties of the plasma flow and synthetic ion energy spectrograms for setup #2. The layout of the figure is identical to that of Figure 5.2. In block "S", the spacecraft moves along the $(y = 0, z = -1.3R_E)$ line, whereas in block "U" the hypothetical trajectory is located at $(x = -1.3R_E, y = 0)$. In block "D", the spacecraft trajectory is given by $(x = +1.3R_E, y = 0)$.

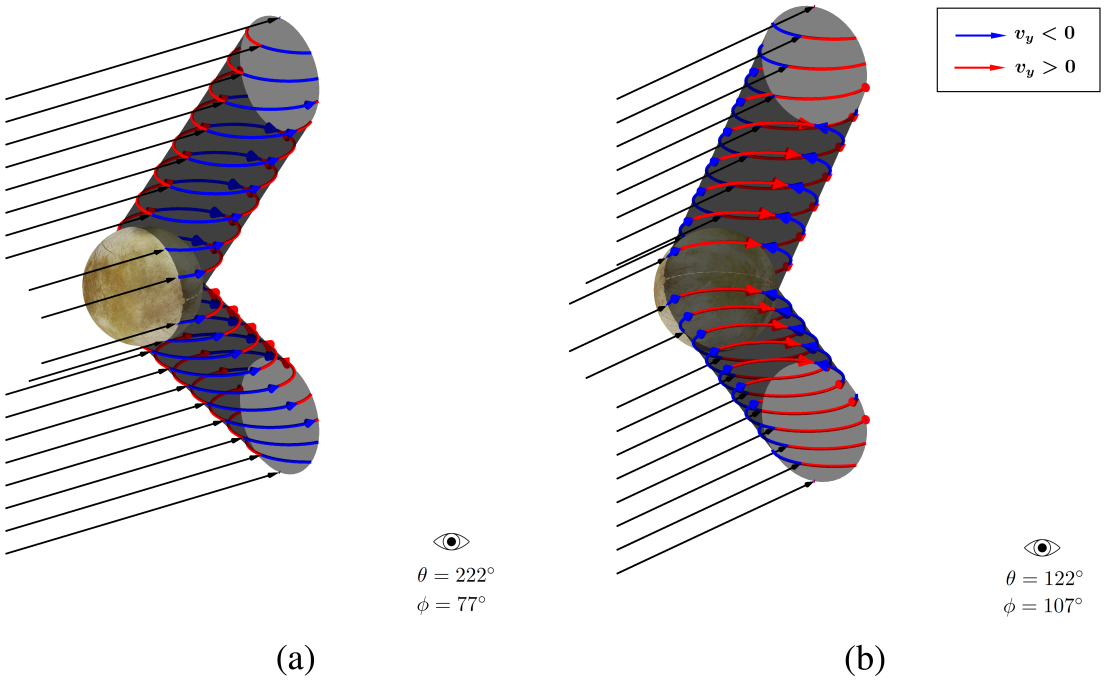

Figure 5.4: Deflection of the incident magnetospheric plasma around Europa's tilted Alfvén wings. The deflection of the upstream flow (which is aligned with the $(+x)$ axis) generates alternating regions with a velocity component toward Jupiter ($v_y > 0$, red) or away from Jupiter ($v_y < 0$, blue). (a) Side view from upstream, (b) view from downstream.

South-polar plume

The pick-up tails of plume and exospheric ions are rotated out of the (x, z)-plane. Therefore, within the (x, z) plane both tails are visible only in Europa's immediate vicinity (see Figure 5.3, block "S", panels (b) and (d)). The perturbations in the bulk velocity (Figure 5.3, block "S", panel (a)) and the upstream plasma density (Figure 5.3, block "S", panel (c)) are also much weaker than in a rotated plane $(x, \tilde{z})$ containing the wing characteristics. The model output for the $(x, \tilde{z})$ plane containing the wing characteristics has been discussed in Arnold *et al.*, 2020a (see Figure 5 in that work). Here the results for the (x, z) plane are mainly shown to provide context for the interpretation of the ion energy spectrograms which are calculated along flyby trajectories in that plane.

In the $x < 0$ segments of the ion energy spectra, the upstream ion population is again visible, centered around 835 eV. The population of cold plume ions causes a localized

"spike" in all four spectrograms, centered around $x = 0$ (Figure 5.3, block "S", panels (i)–(iv)). However, the spacecraft trajectory remains confined to the (x, z) plane and crosses the plume's pick-up tail only close to Europa (between $x \approx 0 - 1R_E$). A Europa-averted detector shows slightly stronger plume signatures (especially around $x = 1R_E$) than a detector facing Europa, since the drift of the plume ions in the draped magnetic field has a northward component. However, the effect is more subtle than in setup $\#1$, as the spacecraft no longer intersects the "core" of the southern Alfvén wing (see section 3.1.1). In the upstream region ($x \leq 0$), count rates for a detector facing away from Jupiter are higher than for a detector facing Jupiter, whereas downstream of the actual plume crossing ($x \geq 2R_E$) the detector facing Jupiter measures slightly higher count rates. This disparity is due to the plasma deflection around the Alfvén wings: at the upstream side of the quasi-cylindrical southern Alfvén wing (which is inclined out of the (x, z) plane away from Jupiter), the flow observable by the spacecraft is diverted toward Jupiter, thereby hitting the Jupiter-averted detector. However, at the downstream side of the Alfvén wing, the flow hitting the spacecraft is deflected away from Jupiter and therefore mainly enters the Jupiter-facing detector. This upstream-downstream asymmetry did not occur in setup $\#1$, where $\vec{B}_0$ points in $(-z)$-direction and the flow deflection disappears near the $y = 0$ plane (since the rotation of the fields in the main Alfvén wings due to the Hall effect is rather weak, see Arnold *et al.*, 2020a; Kivelson *et al.*, 2004; Simon *et al.*, 2011). In the immediate vicinity of Europa's south pole, the deflection of the magnetospheric ions around the "core" of the plume, combined with the (almost) unidirectional motion of the plume particles, again causes highly localized gaps in the spectrograms observable by several detectors (see Figure 5.3, block "S", panels (i), (ii), and (iv)).

Upstream Plume

Within the (x, z) plane, the plume is barely visible in macroscopic parameters of the incident magnetospheric plasma for the south-polar case, but when located upstream, it causes

a distinct drop in the plasma bulk velocity around $x = -1\ R_E$ (see Figure 5.3, block "U", panel (a)). As suggested by Arnold *et al.*, 2020a, the plasma bulk speed is the only macroscopic quantity that contains discernible plume signatures in this case.

The most suitable approach to identify an upstream plume in particle data is again with a detector pointed toward Europa, since no upstream plasma flow moves in that direction. The spectrogram of Figure 5.3, block "U", panel (iv) is therefore not "contaminated" by the contribution of the magnetospheric plasma. The spectra for the other three detector orientations (toward upstream, toward Jupiter and away from Jupiter) are qualitatively similar to the preceding case where Europa was located in the center of Jupiter's plasma sheet and no induced dipole was present (see section 3.1.2). In particular, the spectrogram acquired by a detector looking toward upstream (Figure 5.3, block "U", panel (ii)) is nearly identical to the preceding case. Since the x component of an individual ion's velocity alone determines whether it is "seen" by this model detector, the shape of the spectrogram is not affected by the deflection around the Alfvén wing in the ($\pm y$) direction.

However, the spectrograms recorded by the Jupiter-facing and Jupiter-averted detectors now exhibit a north-south asymmetry caused by the inclination of the Alfvén wings and the location of the trajectory upstream of Europa: in the southern hemisphere the Alfvén wing is inclined in $(-y)$ direction. Therefore the spacecraft encounters the region where the plasma is deflected toward Jupiter around the southern Alfvén wing. In the northern hemisphere the Alfvén wing is inclined toward Jupiter and the spacecraft therefore encounters a region where the flow is deflected away from the planet (see also Figure 5.4 and Figure 21.2 in Kivelson *et al.*, 2004). Hence, a detector facing Jupiter (Figure 5.3, block "U", panel (i)) measures increased count rates in Europa's northern hemisphere (where more ions move toward the detector) and reduced count rates in Europa's southern hemisphere. For the detector looking away from Jupiter (Figure 5.3, block "U", panel (iii)) the geometry is reversed. However, these deflection patterns do not contain any clearly discernible signature of the Alfvén winglet associated with the plume and can readily be explained

through deflection around the "main" Alfvén wing, generated by the interaction with the global ionosphere (Paterson *et al.*, 1999). For this reason, a "spike" of cold plume plasma near $x = 0$ is indicative of a plume crossing in Europa's upstream hemisphere, but the accompanying deflection features are not specific to the presence of a plume.

Downstream plume

The thermal plasma parameters are similar to the case with a plume located at Europa's upstream apex (see Figure 3, block "D", panels (a)–(d)). The most remarkable feature is that –despite the inclination of the upstream magnetic field– the pick-up tail formed by the plume ions is still oriented along the x axis. On the other hand, the tail formed by ions from the global ionosphere is again rotated out of the (x, z) plane. There is only weak plume-plasma interaction visible in the plasma bulk velocity, since the plume is "shielded" by the solid body of Europa. Pick-up of newly generated plume ions is weakest in this configuration, since the incident plasma is largely deflected around Europa.

In the previous setup (section 3.1.3), without an induced dipole, the downstream plume did not generate a discernible spike in the ion energy spectra, either because the particle production rates were too low or the acceleration due to pick-up was too weak. However, when the dipole is included, the plume generates a distinct spike during the crossing, independent of the detector orientation. For a detector facing the plume we now see three distinct peaks in the ion energy spectrogram (Figure 3, block "D", panel (iv)), two of them at the outer edges of Europa's geometric plasma shadow and the third one in its center, coinciding with the position of the plume. Hence, in contrast to the preceding scenario, the plume is now able to superimpose a third, central peak on the initially M-like structure associated with ion pick-up from Europa's global ionosphere (see section 3.1.3). This time, the ion energies are much higher than in the scenario without an induced dipole. The detector facing downstream also detects a highly localized population of cold particles within the bounds of Europa's geometric plasma shadow (see Figure 5.3, block "D", panel (ii)).

Due to the inclination of the Alfvén wings, Europa's wake in the (x, z) plane is not completely shielded from the upstream plasma anymore. Therefore, this signature corresponds mainly to the thermal motion of slow plasma antiparallel to the bulk flow (see Figure 5.3, block "D", panel (iv)).

Similar to the flyby through the upstream plume, the Jupiter-facing and Jupiter-averted detectors display intense signatures of the flow deflection around the tilted "main" Alfvén wing and the associated north-south asymmetry. The deflected ions start to resume motion in $(+x)$ direction downstream of the Alfvén wing tubes. Therefore, the flow is deflected toward Jupiter in Europa's northern hemisphere, whereas the magnetospheric ions move away from Jupiter in Europa's southern hemisphere. For this reason, the Jupiter-averted detector registers increased particle counts in Europa's northern hemisphere, whereas its spectrogram displays a prominent gap in the southern hemisphere. The opposite can be seen in the data from the Jupiter-facing detector. Since the perturbations associated with Europa's main Alfvén wing are way more intense at the moon's wakeside than along an upstream flyby trajectory (see Arnold *et al.*, 2020a, Figure 5, panels (a)–(c)), the dips and enhancement signatures in these spectra are much more prominent than in case of an upstream plume.

Overall, in the scenario where Europa is located outside of Jupiter's plasma sheet, the deflection signatures around the main Alfvén wings make a significant contribution to the particle flow into the detector. These signatures dominate the particle spectra and can severely complicate the identification of plume signatures in spacecraft data.

5.4.3 Plasma interaction during the Galileo E26 flyby

Magnetic field and energetic proton data from the E26 flyby are indicative of a plume crossing in Europa's southern trailing hemisphere (Arnold *et al.*, 2019; Huybrighs *et al.*, 2020). For simplicity, the flyby trajectory in our model setup is a straight line through the point of closest approach of E26 at $x = -0.83R_E$, $z = -0.89R_E$, i.e., south of Europa's equator. The spacecraft moved in $(+y)$ direction (i.e., toward Jupiter) and intersected the cylinder $\sqrt{y^2 + z^2} = R_E$, thereby penetrating "deeper" into Europa's main Alfvén wing than during the generic cases in sections 3.1 and 3.2. The orientation of the magnetic background field is $\vec{B}_0 = (-22, 205, -379)$ nT, leading to Alfvén wing characteristics which are again inclined against the $z = 0$ plane. To identify the contribution of plume ions to the modeled ion energy spectra, we present results for two runs: one run with a plume and a "baseline scenario" without a plume. Results for both scenarios are shown in Figure 5.5. The parameters of the incident magnetospheric flow and Europa's global exosphere are the same in both runs. The model results for the electromagnetic fields for both setups can be found in Arnold *et al.*, 2019.

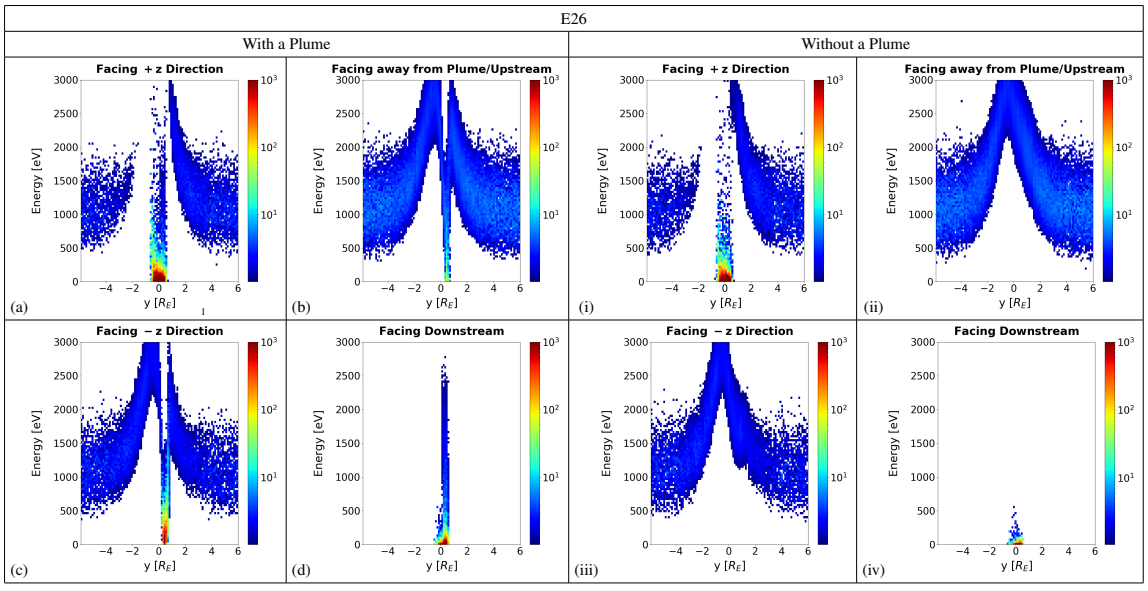

Figure 5.5: Synthetic ion energy spectrograms, as observable for different viewing directions of a particle detector during the Galileo E26 flyby of Europa. Left block ((a)–(d)): with the plume included, right block ((i)–(iv)): "baseline run" without the plume.

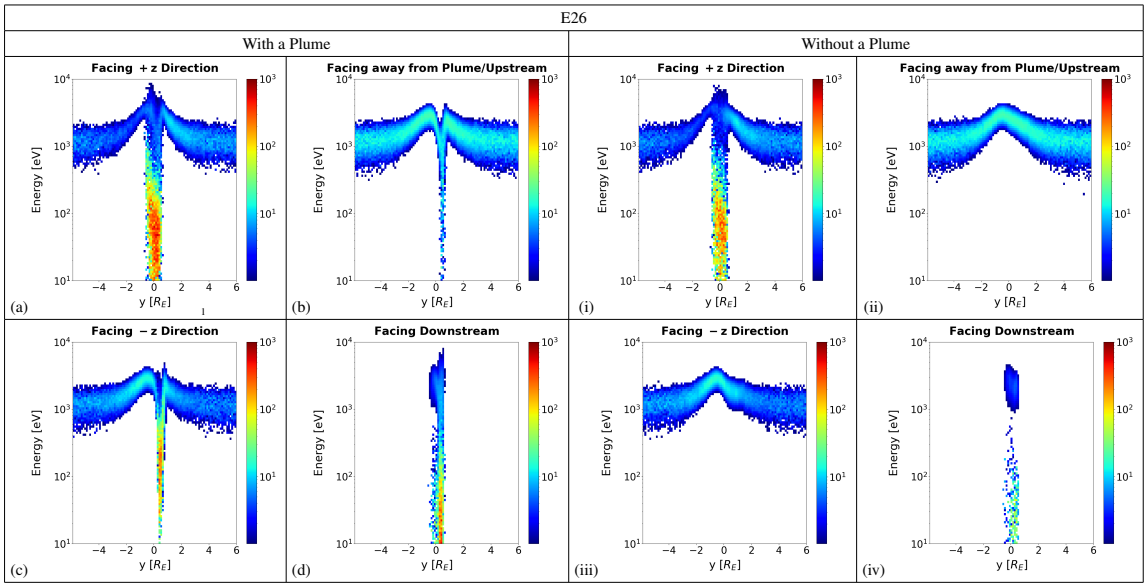

Figure 5.6: Synthetic ion energy spectrograms for the E26 flyby. The model output shown is the same as in Figure 5.5. However, here the spectrograms are plotted on a logarithmic energy scale.

The spectrogram recorded by a detector looking toward Europa in $(+x)$ direction (toward downstream, see Figure 5.5(d)) contains a clearly discernible signature of the plume, since this detector does not record any magnetospheric upstream particles (similar to Figures Figure 5.2 and Figure 5.3, blocks "U", panels (iv)). However, for this detector orientation, the difference between a run with (Figure 5.5(d)) and without a plume (Figure 5.5(iv)) is rather quantitative than qualitative. Without a plume, the spacecraft still observes a localized enhancement in the spectrogram when it "scratches" the outer regions of Europa's atmosphere around closest approach. The intensity of this peak is amplified by more than an order of magnitude (at energies below 500 eV) when a plume is included. However, to infer the presence of a plume one would need a very accurate model of Europa's global atmosphere at the time of E26, since the plume does not generate any qualitatively new signatures in the "downstream" spectrogram.

In the spectrogram from a detector looking away from the plume in $(-x)$ direction (i.e., toward upstream, see Figure 5.5(b)), the upstream ion population is visible outside of the interaction region. Around closest approach, upstream ions are accelerated and deflected

at the flanks of Europa's southern Alfvén wing. Count rates are therefore shifted toward higher energies (up until $\approx$ 3000 eV). When a plume is included, a characteristic dip is carved into the "bell-like" acceleration feature in the spectrogram, since newly generated plume ions have not yet obtained a significant velocity at the altitude of the flyby. Surprisingly, the detector looking toward upstream (away from Europa) obtains a more clearly visible plume signature than the detector looking toward downstream (toward Europa). The reason for this is that around closest approach of E26, the spacecraft was immersed in the population of cold plume ions while still remaining "far enough upstream" to detect the deflection of the incident magnetospheric ions by the Alfvén wing(let). Due to its small scale height (compared to that of the plume), ions from Europa's global exosphere do not appear in either of the two spectrograms (Figures Figure 5.5(b) and (ii)) for this viewing direction. The cold plume ion population is therefore clearly discernible over the "background" of warm, deflected magnetospheric flow. These ions have just been picked up, thereby moving back toward Europa. A detector looking southward (in $(-z)$ direction, see Figure 5.5(c)) observes almost the same features, since the detector is oriented away from the plume as well and is also able to capture a decent portion of the upstream particles.

If the detector faces into the $(+z)$ direction (northward, see Figure 5.5(a)), its field of view is partially "obscured" by Europa's solid body (see Figure 5.1(b), violet cylinder). In the run without a plume (Figure 5.5(i)), the model reveals a highly asymmetric deflection feature: two uneven outer flanks with peak energies above 2000 eV, caused by the deflection of the upstream flow around Europa's inclined southern Alfvén wing, and a dip in between, generated by Europa's cold exospheric ions. When a plume is included, the deflection pattern barely changes. Thus, for a detector looking in $(+z)$ direction, the differences between both runs are rather quantitative than qualitative and not sufficient to obtain clear evidence for the presence of the plume.

In conclusion, a detector facing toward upstream or southward would have had the highest chances to identify the E26 plume in thermal plasma data. Only in these spectrograms

the presence of the plume causes qualitative differences to a scenario that considers only Europa's global atmosphere, but no plume. This confirms our earlier finding that a detector looking toward Europa does not necessarily have the highest chances of unambiguously identifying a plume source on the moon's surface.

In practical applications, ion energy spectrograms are often plotted with a logarithmic energy axis. To illustrate the impact of such a rebinning on the shape of the spectrograms, Figure 5.6 displays the modeled spectrograms for E26, but with a logarithmic energy axis. As can be seen, logarithmic energy binning provides better resolution of the low-energy plume ion population. However, this approach also drastically attenuates the deflection features visible in the incident magnetospheric ion population. In our model scenarios, the deflection of the upstream particles often made the strongest contribution to the plasma interaction signatures associated with a plume.

5.5 Summary and Concluding Remarks

Using the output of a hybrid model (Arnold *et al.*, 2019; Arnold *et al.*, 2020a), we have generated synthetic energy spectrograms of the thermal ion population observable in the vicinity of plumes at various locations on Europa's surface. In this way, we have assessed the influence of the local electromagnetic field perturbations and the viewing geometry on the detectability of potential plume signatures in Europa's thermal plasma environment by a spacecraft.

Our results show that even in the immediate vicinity of Europa, flow deflection by the moon's Alfvén wings has a drastic influence on the observability of pick-up ions from a local plume source. For instance, the pick-up tail formed by a plume at Europa's south pole is slightly "lifted" northward by the draped magnetic field in the moon's southern Alfvén wing. In this process, the plume ions' drift velocity gains a component *toward* Europa, i.e., a detector looking *away* from the moon is most suitable to observe this newly generated ion population. In addition, the Alfvén winglet generated by a plume locally

amplifies the deflection of the incident magnetospheric plasma around the obstacle, thereby generating an indirect signature of the plume in the ion energy spectrograms. However, in order to isolate the additional deflection of the upstream ions caused by the Alfvén winglet, a reference spectrogram would be required for an interaction scenario that does *not* consider the plume source.

Depending on the viewing direction of a thermal particle detector, the ion population associated with a plume may also be partially or completely obscured by the incident magnetospheric ions. While this is evident when the detector is oriented toward upstream, the strong deflection of the incident magnetospheric flow around Europa's Alfvén wings may also obstruct the plume ions in the recording of a detector that looks, e.g., toward or away from Jupiter.

Overall, our results suggest that thermal ion energy spectrograms provide a valuable diagnostic tool to support the identification of local plume sources at Europa through in-situ observations. However, only for very few specific flyby geometries and plume locations, the signatures in these spectrograms are "sufficiently unique" to be directly associated with the presence of a plume of water vapor. Also, the spectrograms presented in this study have been generated under the assumption that the viewing direction of the particle detector remains fixed during a close flyby. In reality, however, the detector orientation will continuously change throughout the flyby due to the inherent rotation of the spacecraft and the detector itself. Thus, the actual energy spectrograms observed during an Europa flyby will consist of a sequence of "vertical slices" through the time series obtained for fixed viewing directions in this study. In some cases, the signatures associated with a plume crossing are particularly narrow, such as the highly localized enhancement in ion counts generated by a source at Europa's wakeside apex. In such a case, an unfavorable momentary viewing geometry will cause the plasma detector to completely miss any potential signatures of the plume passage. The detectability of such localized plume signatures ultimately depends on the rotation period of the spacecraft, compared to the time it needs to travel through the

perturbations caused by the plume. Also, changes in the upstream conditions throughout the duration of a flyby could add dynamic features to the spectrograms which may further shroud the signatures associated with a plume.

Our study reveals that plumes can often be identified in the spectrograms in an indirect way, i.e., through the pronounced "gaps" that they carve into the distribution of the incident magnetospheric ions (which have energies on the order of 1 keV). Taking into account the non-zero velocity of the spacecraft would mainly shift the energy range of the cold plume ions in the spectrograms by a few eV. However, the energy of the plume ions would still be much lower than that of the magnetospheric ions. Thus, in a real-world scenario, the general shape of the spectrograms would remain very similar to the results shown here. Overall, the identification of plumes through the perturbations they leave in particle and field data will always require to take into account information on multiple components of Europa's plasma interaction (e.g., thermal ions, energetic ions, magnetic field).

CHAPTER 6

SUMMARY OF THE FINDINGS OF THIS DISSERTATION

6.1 Magnetic Signatures of a Plume at Europa during the Galileo E26 Flyby (Arnold *et al.*, 2019)

Prior to the beginning of this dissertation, only Blöcker *et al.*, 2016 tried to demonstrate the detectability of plume signatures in magnetic field data by comparing their model output with Galileo flyby data from the E26 flyby. To model the complex plasma interaction at Europa, they used a single fluid magnetohydrodynamic (MHD) approach. Even though the plasma interaction at Europa is suitable for an MHD approach, their model is not able to describe the flow shear between separate ion species, e.g. the flow shear between the upstream plasma and plume ions. The MHD approach therefore does not incorporate the ionospheric Hall effect, which might caused the discrepancies between their model and Galileo data. Shortly after Blöcker *et al.*, 2016, the study of Jia *et al.*, 2018 presented hints of a plume crossing during the E12 flyby. They used a multifluid MHD model with an inclined neutral profile for the plume molecules.

The results of Blöcker *et al.*, 2016 were very promising, our goal therefore was to re-analyze the E26 flyby. Thus, we developed a three-dimensional hybrid (kinetic ions, fluid electrons) model of Europa's magnetospheric interaction, included the plume profile from Jia *et al.*, 2018 and tested multiple plume orientations and profiles for the global atmosphere. We worked towards answering "Are plumes visible in Galileo magnetic field data of close ($\leq$ 400km) Europa flybys?", along with "How do plumes contribute to the plasma interaction at Europa?".

By analyzing the magnetic field components measured during E26, we showed that our model is able to describe the signatures that are potentially associated with the magnetic

field bending and pileup in front of a plume. An implication of this result is that an approach that incorporates the ionospheric Hall effect is needed to describe the perturbations measured on the small length scales of a close spacecraft flyby (on the order of ≈400 km). Furthermore, by comparing runs with and without a plume, our model shows that a plume source is required to explain the fine structures in the magnetic field perturbations observed by Galileo during the E26 flyby of Europa. Although the magnetic signatures along the E26 trajectory were highly sensitive to the plume orientation, various orientations led to a similarly good agreement with observations.

6.2 Plasma interaction signatures of plumes at Europa (Arnold *et al.*, 2020a)

Our work aimed to study the plasma interaction for different plume locations across Europa's surface, and to determine the degree to which different plume configurations can be obscured by the interaction of Jupiter's magnetospheric plasma with Europa's induced dipole field and its global atmosphere. Hence, we simulated Europa's plasma environment for three plume locations: a plume at Europa's south pole and a plume at the apex of the upstream and downstream hemisphere of the moon, respectively. We combined the plume sources with symmetric and asymmetric density profiles (taken from Arnold *et al.*, 2019) of Europa's global atmosphere. Additionally, we varied the strength and orientation of Jupiter's magnetic background field at Europa, simulating two scenarios: a scenario without an induced dipole, which corresponds to the case when Europa's distance to the Jovian current sheet is at its minimum, and a scenario with an induced dipole, when Europa is located above or underneath the center of Jovian's current sheet.

Our simulations revealed that in the scenario with an induced dipole, the induction signatures dominate the plasma interaction. The magnetic perturbations of a plume will be close to the detection threshold. Therefore, we recommend a flyby when Europa is close to the center of Jupiter's plasma sheet and the strength of the induced dipole is at its minimum.

In the scenario without an induced dipole, the plume's visibility is determined by the

ratio of the plume's density to the density of the global atmosphere around the plume location. In simulations with an asymmetric atmosphere (denser at Europa's ram side by a factor of 10), the signatures of a plume at the ram side apex are almost indiscernible from the signatures generated by the global atmosphere alone. Still, plumes locally modify the draping signatures in B_x and generate distinct pile-up features in B_z, but remain almost "invisible" in B_y. In addition, the plasma quantity most diagnostic for the crossing of a plume is the bulk velocity $|\vec{U}|$, which is reduced within a radius of several R_E around the plume source. Overall, we came to the conclusion that precise knowledge of the plasma's upstream parameters and the density profile of Europa's global atmosphere is required to identify plumes in plasma data. Additionally, the detectability of plume signatures depends strongly on the spacecraft's trajectory.

6.3 Applying Ion Energy Spectrograms to Search for Plumes at Europa (Arnold *et al.*, 2020b)

Huybrighs *et al.*, 2016 found that in addition to the magnetic field signature of a plume, it should be possible to detect plumes in energy spectrograms of neutral and charged particles acquired near Europa. Indeed, Tokar *et al.*, 2009 demonstrated that plumes are visible in thermal ion energy spectrograms obtained by the Cassini spacecraft at Enceladus. Yet, until this study no attempt had been made to identify the imprint that potential plumes leave in particle energy spectra acquired by plasma detectors aboard a spacecraft. Recently the demand for an alternative to an in-situ plume detection through magnetic field observation arose, when NASA announced to replace the magnetometer on board the Europa Clipper spacecraft (with "a less complex instrument", Loff, 2019). We decided to build upon the study of Arnold *et al.*, 2020a by analyzing our hybrid model output. We determined the kinetic energy distribution of particles and calculated the ion energy distribution along hypothetical trajectories that intersect plumes at different surface locations. Hence, the goal of our work was to provide a framework for the identification of plume signatures in

particle data for upcoming in-situ flyby missions.

Our study revealed that in the immediate vicinity of Europa, the visibility of a plume is strongly affected by the ion deflection around Europa's Alfvén wings generated by the moon's global atmosphere. Due to field line draping, a particle detector looking away from Europa may have the best chance of capturing signatures of a plume source. For example, in the case of a south polar plume, the pick-up tail formed by the plumes ions is lifted toward the moon by the draped magnetic field in Europa's southern Alfvén wing. The plume ions therefore obtain a velocity component pointing northward (to Europa), right into a detector facing into the opposite direction. Our results suggest that ion energy spectrograms provide a useful tool for the identification of plumes at Europa. Nevertheless, the ion population associated with a plume may be partially or completely obscured by the incident magnetospheric ions. Only a few combinations of flyby geometries and plume locations were suitable for an in-situ plume detection through ion energy spectrograms. And, lastly, (as a result of the rotation of the spacecraft) an unfavorable momentary viewing geometry could cause the plasma detector to completely miss any potential signatures of the plume passage.

REFERENCES

[1] H. Arnold *et al.*, "Magnetic signatures of a plume at Europa during the Galileo E26 flyby," *Geophysical Research Letters*, vol. 46, no. 3, pp. 1149–1157, 2019. eprint: https://agupubs.onlinelibrary.wiley.com/doi/pdf/10.1029/2018GL081544.

[2] H. Arnold *et al.*, "Plasma interaction signatures of plumes at Europa," *Journal of Geophysical Research: Space Physics*, vol. 125, no. 1, e2019JA027346, 2020, e2019JA027346 10.1029/2019JA027346. eprint: https://agupubs.onlinelibrary.wiley.com/doi/pdf/10.1029/2019JA027346.

[3] H. Arnold *et al.*, "Applying ion energy spectrograms to search for plumes at Europa," *Journal of Geophysical Research: Space Physics*, vol. n/a, no. n/a, e2020JA028376, 2020, e2020JA028376 2020JA028376. eprint: https://agupubs.onlinelibrary.wiley.com/doi/pdf/10.1029/2020JA028376.

[4] F. Bagenal *et al.*, "Plasma conditions at Europa's orbit," *Icarus*, vol. 261, pp. 1–13, 2015.

[5] P. M. Banks and G Kockarts, "Aeronomy, part a," *Academic, San Diego, Calif*, p. 184, 1973.

[6] A. Blöcker *et al.*, "Europa's plasma interaction with an inhomogeneous atmosphere: Development of Alfvén Winglets within the Alfvén Wings," *Journal of Geophysical Research (Space Physics)*, vol. 121, no. 10, pp. 9794–9828, 2016.

[7] B. R. Breer *et al.*, "Energetic ion dynamics in the perturbed electromagnetic fields near Europa," *Journal of Geophysical Research: Space Physics*, vol. 0, no. 0, 2019. eprint: https://agupubs.onlinelibrary.wiley.com/doi/pdf/10.1029/2019JA027147.

[8] M. H. Burger and R. E. Johnson, "Europa's neutral cloud: morphology and comparisons to Io," *Icarus*, vol. 171, pp. 557–560, 2004.

[9] T. A. Cassidy *et al.*, "Magnetospheric ion sputtering and water ice grain size at Europa," *pss*, vol. 77, pp. 64–73, 2013.

[10] A. J. Coates *et al.*, "Cassini in Titan's tail: CAPS observations of plasma escape," *Journal of Geophysical Research (Space Physics)*, vol. 117, no. A5, A05324, 2012.

[11] J. F. Cooper *et al.*, "Energetic ion and electron irradiation of the icy Galilean satellites," *Icarus*, vol. 149, no. 1, pp. 133 –159, 2001.

[12] V. P. Dahlke, “Erstellung von Energiespektrogrammen aus Simulationsergebnissen und Vergleich mit Cassini-Messungen für den Saturnmond Enceladus,” Bachelor’s thesis, 2011.

[13] R. T. Desai *et al.*, “Hybrid simulations of positively and negatively charged pickup ions and cyclotron wave generation at Europa,” *Journal of Geophysical Research: Space Physics*, vol. 122, 2017, 2017JA024479.

[14] T. Doggett *et al.*, “Geologic stratigraphy and evolution of Europa’s surface,” in *Europa, Edited by Robert T. Pappalardo, William B. McKinnon, Krishan K. Khurana ; with the assistance of René Dotson with 85 collaborating authors. University of Arizona Press, Tucson, 2009. The University of Arizona space science series ISBN: 9780816528448, p.137*, R. T. Pappalardo *et al.*, Eds. 2009, p. 137.

[15] M. Feyerabend *et al.*, “Filamented ion tail structures at Titan: A hybrid simulation study,” *PSS*, vol. 117, pp. 362–376, 2015.

[16] M. Feyerabend *et al.*, “Hybrid simulation of Titan’s interaction with the supersonic solar wind during Cassini’s T96 flyby,” *grl*, vol. 43, 2016.

[17] L. A. Frank *et al.*, “The plasma instrumentation for the Galileo mission,” *Space Science Reviews*, vol. 60, pp. 1572–9672, 1992.

[18] G. Giono *et al.*, “An analysis of the statistics and systematics of limb anomaly detections in HST/STIS transit images of Europa,” *The Astronomical Journal*, vol. 159, no. 4, p. 155, 2020.

[19] M. Grey *et al.*, “Europa PIMS prototype faraday cup development,” in *2018 IEEE Aerospace Conference*, 2018, pp. 1–15.

[20] D. T. Hall *et al.*, “Detection of an oxygen atmosphere on Jupiter’s moon Europa,” *NAT*, vol. 373, pp. 677–679, 1995.

[21] K. P. Hand and C. F. Chyba, “Empirical constraints on the salinity of the europan ocean and implications for a thin ice shell,” *Icarus*, vol. 189, no. 2, pp. 424 –438, 2007.

[22] C. J. Hansen *et al.*, “The composition and structure of the Enceladus plume,” vol. 38, no. 11, p. L11202, 2011.

[23] H. Hussmann *et al.*, “Thermal equilibrium states of Europa’s ice shell: Implications for internal ocean thickness and surface heat flow,” *Icarus*, vol. 156, no. 1, pp. 143 –151, 2002.

[24] H. L. F. Huybrighs *et al.*, "On the in-situ detectability of Europa's water vapour plumes from a flyby mission," *Icarus*, vol. XXX, in press, 2016.

[25] H. L. F. Huybrighs *et al.*, "On the in-situ detectability of Europa's water vapour plumes from a flyby mission," *Icarus*, vol. 289, pp. 270–280, 2017. arXiv: 1704.00912.

[26] H. L. F. Huybrighs *et al.*, "An active plume eruption on Europa during Galileo flyby E26 as indicated by energetic proton depletions," *Geophysical Research Letters*, vol. 47, no. 10, e2020GL087806, 2020, e2020GL087806 10.1029/2020GL087806. eprint: https://agupubs.onlinelibrary.wiley.com/doi/pdf/10.1029/2020GL087806.

[27] W.-H. Ip *et al.*, "Ion sputtering and surface erosion at Europa," *Geophysical Research Letters*, vol. 25, no. 6, pp. 829–832, 1998.

[28] X. Jia *et al.*, "Evidence of a plume on Europa from Galileo magnetic and plasma wave signatures," *Nature Astronomy*, vol. 2, pp. 459–464, 2018.

[29] R. Johnson *et al.*, "Radiation effects on the surface of the Galilean satellites," in *Jupiter: The Planet, Satellites and Magnetosphere*, Cambridge Univ., 2004, pp. 485–512.

[30] K. K. Khurana *et al.*, "Induced magnetic fields as evidence for subsurface oceans in Europa and Callisto," *Nature*, vol. 395, no. 6704, pp. 777–780, 1998.

[31] S. W. Kieffer *et al.*, "A Clathrate reservoir hypothesis for Enceladus' south polar plume," *Science*, vol. 314, no. 5806, pp. 1764–1766, 2006. eprint: http://science.sciencemag.org/content/314/5806/1764.full.pdf.

[32] Y.-K. Kim *et al.*, *Electron-impact cross sections for ionization and excitation database*, NIST Standard Reference Database 107 (ver. 3.0), 2004.

[33] M. G. Kivelson *et al.*, "Europa and Callisto: Induced or intrinsic fields in a periodically varying plasma environment," *Journal of Geophysical Research (Space Physics)*, vol. 104, no. A3, pp. 4609–4626, 1999.

[34] M. G. Kivelson *et al.*, "Magnetospheric interactions with satellites," in *Jupiter. The planet, satellites and magnetosphere*, F. Bagenal, T.E. Dowling and W.B. McKinnon, Ed., Cambridge Univ. Press, 2004, pp. 513–536.

[35] M. G. Kivelson *et al.*, "Europa's Interaction with the Jovian Magnetosphere," in *Europa, Edited by Robert T. Pappalardo, William B. McKinnon, Krishan K. Khurana ; with the assistance of René Dotson with 85 collaborating authors. University of Arizona Press, Tucson, 2009. The University of Arizona space science series ISBN: 9780816528448, p.545*, 2009, p. 545.

[36] M. G. Kivelson *et al.*, "Galileo magnetometer measurements: A stronger case for a subsurface ocean at Europa," *Science*, vol. 289, pp. 1340–1343, 2000.

[37] C. Koenders *et al.*, "Dynamical features and spatial structures of the plasma interaction region of 67P/Churyumov-Gerasimenko and the solar wind," vol. 105, pp. 101–116, 2015.

[38] H. Kriegel *et al.*, "The plasma interaction of Enceladus: 3D hybrid simulations and comparison with Cassini MAG data," *Planetary and Space Science*, vol. 57, no. 14, pp. 2113 –2122, 2009.

[39] H. Kriegel *et al.*, "Influence of negatively charged plume grains on the structure of Enceladus' Alfvén wings: Hybrid simulations versus Cassini magnetometer data," *Journal of Geophysical Research: Space Physics*, vol. 116, no. 10, 2011, cited By 41.

[40] H. Kriegel *et al.*, "Ion densities and magnetic signatures of dust pick-up at Enceladus," *Journal of Geophysical Research (Space Physics)*, vol. 119, no. 4, pp. 2740–2774, 2014.

[41] W. Kurth *et al.*, "The plasma wave environment of Europa," *Planetary and Space Science*, vol. 49, no. 3, pp. 345 –363, 2001, Magnetospheres of the Outer Planets (Part I).

[42] L. Liuzzo *et al.*, "The impact of Callisto's atmosphere on its plasma interaction with the Jovian magnetosphere," *Journal of Geophysical Research (Space Physics)*, vol. 120, pp. 9401–9427, 2015.

[43] L. Liuzzo *et al.*, "Disentangling plasma interaction and induction signatures at Callisto: The Galileo C10 flyby," *Journal of Geophysical Research: Space Physics*, vol. 121, no. 9, pp. 8677–8694, 2016.

[44] L. Liuzzo *et al.*, "Magnetic signatures of plasma interaction and induction at Callisto: The Galileo C21, C22, C23, and C30 flybys," *Journal of Geophysical Research: Space Physics*, vol. 122, no. 7, pp. 7364–7386, 2017. eprint: https://agupubs.onlinelibrary.wiley.com/doi/pdf/10.1002/2017JA024303.

[45] L. Liuzzo *et al.*, "Observability of Callisto's inductive signature during the JUpiter ICy Moons Explorer mission," *Journal of Geophysical Research: Space Physics*, vol. 123, no. 11, pp. 9045–9054, 2018.

[46] S. Loff. (2019). "NASA seeks new options for science instrument on Europa Clipper," (visited on 10/01/2020).

[47] M. A. McGrath *et al.*, "Observations of Europa's tenuous atmosphere," in *Europa, Edited by Robert T. Pappalardo, William B. McKinnon, Krishan K. Khurana ; with the assistance of René Dotson with 85 collaborating authors. University of Arizona Press, Tucson, 2009. The University of Arizona space science series ISBN: 9780816528448, p.485*, R. T. Pappalardo *et al.*, Eds., 2009, p. 485.

[48] J. Müller *et al.*, "A.I.K.E.F.: Adaptive hybrid model for space plasma simulations," *Computer Physics Communications*, vol. 182, no. 4, 946–966, doi: 10.1016/j.cpc.2010.12.033, 2011.

[49] J. Müller *et al.*, "Origin of Mercury's double magnetopause: 3D hybrid simulation study with A.I.K.E.F.," *Icarus*, vol. 218, no. 1, pp. 666–687, 2012.

[50] F. M. Neubauer, "Nonlinear standing Alfven wave current system at Io - Theory," *jgr*, vol. 85, pp. 1171–1178, 1980.

[51] F. M. Neubauer, "The sub-Alfvénic interaction of the Galilean satellites with the Jovian magnetosphere," *jgr*, vol. 103, pp. 19 843–19 866, 1998.

[52] F. M. Neubauer, "Alfvén wings and electromagnetic induction in the interiors: Europa and Callisto," *Journal of Geophysical Research (Space Physics)*, vol. 104, no. A12, pp. 28 671–28 684, 1999.

[53] L. Paganini *et al.*, "A measurement of water vapour amid a largely quiescent environment on Europa," *Nature Astronomy*, 2019.

[54] W. R. Paterson and G. Collinson, "On the possibility of a plume traversal during Galileo's E12 encounter with Europa," in *AGU Fall Meeting Abstracts*, vol. 2019, 2019, SM44A–08.

[55] W. R. Paterson *et al.*, "Galileo plasma observations at Europa: Ion energy spectra and moments," *Journal of Geophysical Research: Space Physics*, vol. 104, no. A10, pp. 22 779–22 791, 1999. eprint: https://agupubs.onlinelibrary.wiley.com/doi/pdf/10.1029/1999JA900191.

[56] C. Plainaki *et al.*, "Exospheric O_2 densities at Europa during different orbital phases," *Planet. Space Sci.*, vol. 88, pp. 42–52, 2013.

[57] C. Plainaki *et al.*, "Towards a global unified model of Europa's tenuous atmosphere," *Space Science Reviews*, vol. 214, no. 1, p. 40, 2018.

[58] C. C. Porco *et al.*, "Cassini observes the active south pole of Enceladus," *Science*, vol. 311, no. 5766, pp. 1393–1401, 2006.

[59] M. K. Pospieszalska and R. E. Johnson, "Magnetospheric ion bombardment profiles of satellites - Europa and Dione," *Icarus*, vol. 78, pp. 1–13, 1989.

[60] L. Roth *et al.*, "Transient water vapor at Europa's south pole," *Science*, vol. 343, no. 6167, pp. 171–174, 2014.

[61] L. Roth *et al.*, "Orbital apocenter is not a sufficient condition for HST/STIS detection of Europa's water vapor aurora," *Proceedings of the National Academy of Science*, vol. 111, E5123–E5132, 2014.

[62] L. Roth *et al.*, "Europa's far ultraviolet oxygen aurora from a comprehensive set of HST observations," *Journal of Geophysical Research (Space Physics)*, n/a, 2016.

[63] M. Rubin *et al.*, "Self-consistent multifluid MHD simulations of Europa's exospheric interaction with Jupiter's magnetosphere," *Journal of Geophysical Research (Space Physics)*, vol. 120, pp. 3503–3524, 2015.

[64] J. Saur *et al.*, "Interaction of the Jovian magnetosphere with Europa: Constraints on the neutral atmosphere," *Journal of Geophysical Research (Space Physics)*, vol. 103, pp. 19 947–19 962, 1998.

[65] J. Saur *et al.*, "Three-dimensional plasma simulation of Io's interaction with the Io plasma torus: Asymmetric plasma flow," *JGR*, vol. 104, no. A11, pp. 25 105–25 126, 1999.

[66] J. Saur *et al.*, "Hemisphere coupling in Enceladus' asymmetric plasma interaction," *jgr*, vol. 112, no. A11, A11209, 2007.

[67] P. M. Schenk, "Thickness constraints on the icy shells of the Galilean satellites from a comparison of crater shapes," *Nature*, vol. 417, pp. 419–421, 2002.

[68] N. Schilling *et al.*, "Time-varying interaction of Europa with the jovian magnetosphere: Constraints on the conductivity of Europa's subsurface ocean," *Icarus*, vol. 192, no. 1, pp. 41–55, 2007.

[69] N. Schilling *et al.*, "Influence of the internally induced magnetic field on the plasma interaction of Europa," *Journal of Geophysical Research (Space Physics)*, vol. 113, A03203, A03203, 2008.

[70] J. Schmidt *et al.*, "Slow dust in Enceladus' plume from condensation and wall collisions in tiger stripe fractures," *Nature*, vol. 451, pp. 685–8, 2008.

[71] R. W. Schunk and A. F. Nagy, *Ionospheres: Physics, Plasma Physics, and Chemistry*. Cambridge University Press, 2000.

[72] M. Seufert *et al.*, "Multi-frequency electromagnetic sounding of the Galilean moons," *Icarus*, vol. 214, no. 2, pp. 477–494, 2011.

[73] S. Simon *et al.*, "Influence of negatively charged plume grains and hemisphere coupling currents on the structure of Enceladus' Alfvén wings: Analytical modelling of Cassini magnetometer observations," *Journal of Geophysical Research (Space Physics)*, vol. 116, no. A4, A04221, 2011.

[74] S. Simon *et al.*, "Analysis of Cassini magnetic field observations over the poles of Rhea," *Journal of Geophysical Research (Space Physics)*, vol. 117, no. A7, A07211, 2012.

[75] S. Simon *et al.*, "Variability of Titan's induced magnetotail: Cassini magnetometer observations," *Journal of Geophysical Research (Space Physics)*, vol. 119, no. 3, pp. 2024–2037, 2014.

[76] S. Simon, "An analytical model of sub-alfvénic moon-plasma interactions with application to the hemisphere coupling effect," *Journal of Geophysical Research: Space Physics*, vol. 120, no. 9, pp. 7209–7227, 2015. eprint: https://agupubs.onlinelibrary.wiley.com/doi/pdf/10.1002/2015JA021529.

[77] E. J. Smith *et al.*, "The planetary magnetic field and magnetosphere of Jupiter: Pioneer 10.," *jgr*, vol. 79, pp. 3501–3513, 1974.

[78] D. J. Southwood *et al.*, "Io and its plasma environment," *Journal of Geophysical Research: Space Physics*, vol. 85, no. A11, pp. 5959–5968, 1980. eprint: https://agupubs.onlinelibrary.wiley.com/doi/pdf/10.1029/JA085iA11p05959.

[79] B. S. Southworth *et al.*, "Modeling Europa's dust plumes," vol. 42, pp. 10,541–10,548, 2015.

[80] W. B. Sparks *et al.*, "Probing for evidence of Plumes on Europa with HST/STIS," *The Astrophysical Journal*, vol. 829, no. 2, p. 121, 2016.

[81] W. B. Sparks *et al.*, "Active cryovolcanism on Europa?" *The Astrophysical Journal Letters*, vol. 839, no. 2, p. L18, 2017.

[82] F. Tian *et al.*, "Monte Carlo simulations of the water vapor plumes on Enceladus," *Icarus*, vol. 188, no. 1, 154–161, doi: 10.1016/j.icarus.2006.11.010, 2007.

[83] R. L. Tokar *et al.*, "Cassini detection of Enceladus' cold water-group plume ionosphere," *Geophysical Research Letters*, vol. 36, no. 13, 2009. eprint: https://agupubs.onlinelibrary.wiley.com/doi/pdf/10.1029/2009GL038923.

[84] M. Volwerk *et al.*, "Wave activity in Europa's wake: Implications for ion pickup," *Journal of Geophysical Research (Space Physics)*, vol. 106, pp. 26 033–26 048, 2001.

[85] M. Volwerk *et al.*, "Europa's alfvén wing: Shrinkage and displacement influenced by an induced magnetic field," *Annales Geophysicae*, vol. 25, no. 4, pp. 905–914, 2007.

[86] A. Vorburger and P. Wurz, "Europa's ice-related atmosphere: The sputter contribution," *Icarus*, vol. 311, pp. 135 –145, 2018.

[87] C. Zimmer *et al.*, "Subsurface Oceans on Europa and Callisto: Constraints from Galileo Magnetometer Observations," *Icarus*, vol. 147, no. 2, pp. 329–347, 2000.

VITA

Hannes Arnold was born on May 10, 1988 in Bozen (Italy), where he grew up trilingually. Hannes showed an interest in science from a young age and was especially interested in our solar system and the space beyond. He went to high school in Bozen, with focus on computer science and began to study at the University of Cologne afterwards. Hannes obtained his master's degree in 2017, where he specialized in astrophysics with a minor in computational physics. Shortly after, he enrolled into the PhD program of Georgia Tech with focus on plasma physics. During his three years in the program he published three papers on Europa's plasma interaction and has recently submitted a fourth one. His work has been recognized with the GT Best Publication Award (2019) and the GT Research Excellence Award (2020).